

Table 2. Key model variables.

Variable	Formula	Units
Entrainment	$E = 2(L + W)\alpha v$	$\text{m}^2 \text{s}^{-1}$
Plume Water Volume Flux	$Q = LWv$	$\text{m}^3 \text{s}^{-1}$
Momentum Flux	$M = LWv^2$	$\text{m}^4 \text{s}^{-2}$
Temperature Flux	$F_T = QT_p$	$^\circ\text{C m}^3 \text{s}^{-1}$
Dissolved Solids Flux	$F_s = QSp_w$	g s^{-1}
Dissolved O ₂ and N ₂ Fluxes	$F_{D_i} = QC_i$	mol s^{-1}
Gaseous O ₂ and N ₂ Fluxes	$F_{G_i} = LW\lambda^2(v + v_b)y_i$	mol s^{-1}

Table 3. Non-linear differential flux equations.

Water Volume Flux	$\frac{dQ}{dz} = E$
Momentum Flux	$\frac{dM}{dz} = \frac{\rho_a - \rho_p}{\rho_p} gLW\lambda^2 + \frac{\rho_a - \rho_w}{\rho_p} gLW(1 - \lambda^2)$
Temperature Flux	$\frac{dF_T}{dz} = ET_a$
Salinity Flux	$\frac{dF_s}{dz} = E\rho_a S_a$
Dissolved Gas Flux	$\frac{dF_{D_i}}{dz} = EC_i + \frac{4\pi r^2 N}{v + v_b} K_L(H_i P_i - C_i)$
Gas Flux	$\frac{dF_{G_i}}{dz} = \frac{4\pi r^2 N}{v + v_b} K_L(H_i P_i - C_i)$

Reservoir model

CE-QUAL-W2 (W2) is a two-dimensional, laterally averaged, hydrodynamic and water quality model (USACE, 1995). W2 includes horizontal, but not vertical, momentum, and accounts for momentum transfer from influent streams and the associated shear stress imparted to the surrounding water. W2 was applied to SHR for the year 1998 when the aeration system was operated. A temperature calibration was performed adjusting only the wind-sheltering coefficient. Based on the model calibration, no significant warming is expected to occur in the hypolimnion if the diffuser is not in operation. W2 was then set up to run during the aeration period. During diffuser operation there was no inflow into the reservoir and the only outflow was seepage loss and water supplied to the water treatment plant. For simplicity, all dissolved oxygen (DO) sinks were turned off, with DO treated as a conservative tracer.

Coupled plume and reservoir model

The location of the 360-m long diffuser changes in elevation with its deepest point being closest to the dam wall. Therefore, as shown in Figure 3, it is represented in W2 as 5 discrete segments in consecutive columns. For the purpose of coupling, the plume model is used to compute the flow rate of ambient water entrained as the plume rises, and the flow rate, temperature, and oxygen concentration of the water that is detrainment upon reaching the depth of maximum plume rise. In other words, entrainment removes water of known temperature and oxygen concentration from a range of depths, while detrainment returns the sum of all the entrained water at the specified discharge location after adding the predicted amount of oxygen. As shown in Figure 3, this plume action is simulated within W2 by withdrawing water from the "entrainment"

cells (marked with X in Figure 3) and discharging it at the "detrainment" cell (marked with O in Figure 3). Because of the changing temperature gradient during the course of the simulation, the plume rise height also changes. It was therefore necessary in some cases to specify a new detrainment cell during the course of the simulation, as indicated in Figure 3.

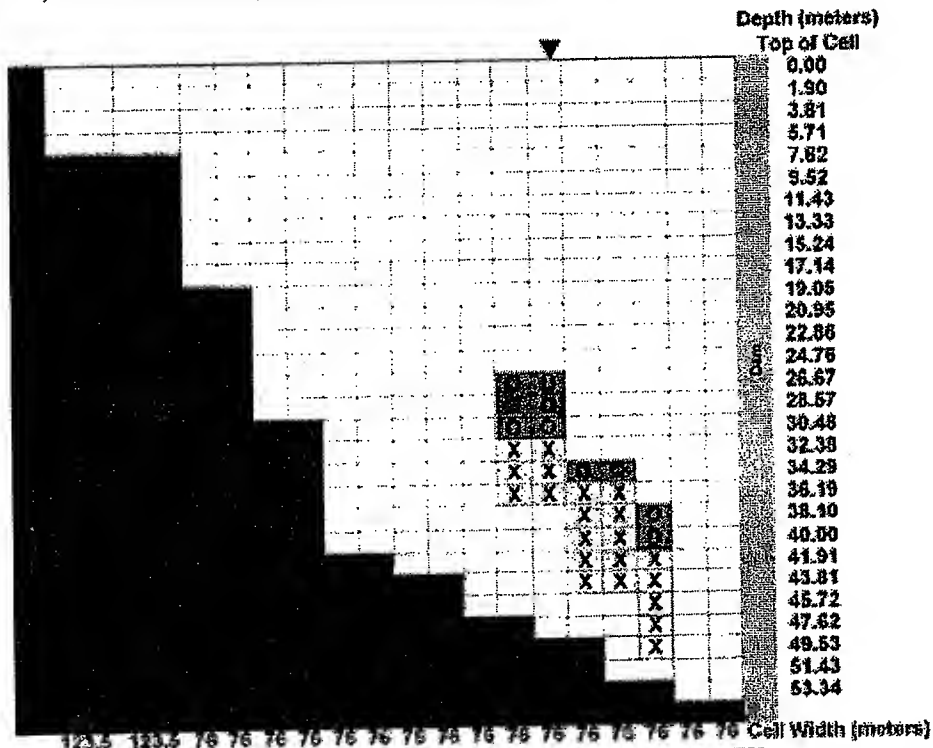


Figure 3. Reservoir grid section for CE-QUAL-W2.

Although the reservoir is laterally averaged, the entrainment operation is adequately represented using a simple withdrawal. However, the entire plume discharge is mixed into the detrainment cell. Because the theoretical plume width at the point of detrainment approaches infinity, this instantaneous mixing appears reasonable to a first approximation. However, the selection of detrainment cell size might be an important consideration when the coupling procedure is refined.

The "manual" coupling procedure was handled as follows. First, the initial reservoir conditions on Sep. 28 were used in the plume model to obtain the flow rate of entrained and detrained water. This procedure was performed for each of the 5 diffuser segments shown in Figure 3. Then, starting on Sep. 28 at 12h00, and using the 5 sets of predicted data, the coupled plume/W2 model was run for 6 hours. The predicted ambient temperature and DO profiles obtained at the end of this 6-hour period were then used as input to the plume model to generate a new set of predicted plume entrainment and detrainment data for each of the 5 plume segments. The entire procedure was repeated until Oct. 9 at 12h00.

RESULTS AND DISCUSSION

The results of the preliminary coupling procedure are shown in Figures 4 and 5. Excluding the water below the diffuser, Figure 4 shows that the coupled model predicts mixing and warming induced by plume operation quite accurately. The thermocline is eroded during the entire period of operation, even though the plume only partially penetrates the thermocline during the first day of simulation at the 2 highest diffuser segments shown in Figure 3. Thereafter, the plume stops between 1 and 3 meters below the thermocline. The results suggest that the flow of detrained water causes sufficient mixing near the thermocline to result in almost exactly the right amount of warming in the hypolimnion. Factors causing

mixing include vertical dispersion of horizontal momentum, momentum transfer from the detraining plume water, and horizontally generated shear. A more thorough investigation into the dominant mixing mechanisms is required.

Although all oxygen sinks are turned off in the W2 model, Figure 5 shows that the coupled model predicts the evolution of hypolimnetic DO fairly well. Once the effects of sediment and other oxygen demands are correctly incorporated in W2, the predicted oxygen concentrations will not increase as rapidly. However, as currently represented, the plume model under-predicts the rate of oxygen addition because oxygen transfer ceases when the plume detrains. Bubbles are still present in the hypolimnion and will continue to rise through the water column. In effect, this produces a weaker secondary plume that results in some additional mixing and oxygen transfer in the hypolimnion, as well as at higher locations in the reservoir. The effects of the secondary plume will be investigated, and if significant relative to the primary plume, will be incorporated in the coupled model.

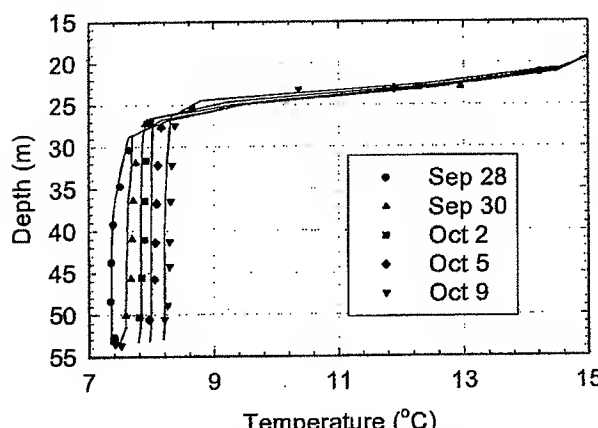


Figure 4. Observed versus predicted hypolimnetic temperature.

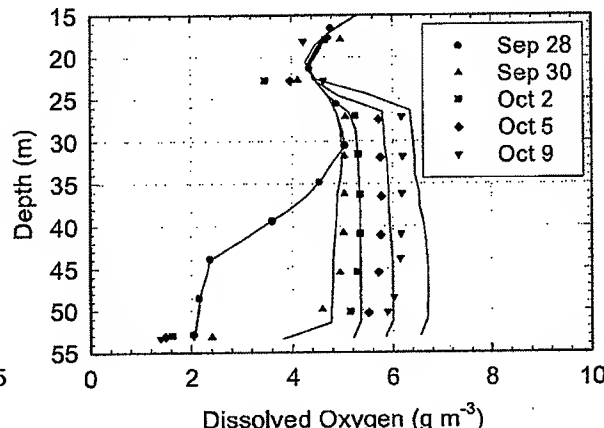


Figure 5. Observed versus predicted hypolimnetic DO.

FUTURE WORK

While the preliminary results are very encouraging, the iterative "manual" coupling procedure is time consuming. The plume model will therefore be incorporated as a subroutine in W2 so that the computation can be done automatically. Further testing of the coupled model will be carried out on new data collected at SHR in Virginia as well as at Lake Baldegg in Switzerland. Ultimately, the coupled model could also be used to improve the calibration of the plume model.

REFERENCES

- Cole T.M. and Buchak E.M. (1995). CE-QUAL-W2: A two-dimensional, laterally averaged, Hydrodynamic and Water Quality Model, Version 2.0. Instruction Report EL-95-. US Army Engineering Waterways Experiment Station, Vicksburg, MS.
- Fannelop T.K., Hirschberg S. and Kuffer J. (1991). Surface Current and Recirculating Cells Generated by Bubble Curtains and Jets. *Journal of Fluid Mechanics*, 229, 629-657.
- Little J.C. and McGinnis D.F. (2000). Hypolimnetic Oxygenation: Predicting Performance using a Discrete-Bubble Model. *Proceedings of 1st World Water Congress, International Water Association (IWA)*, Paris, France, July 3-7.
- Wüest A., Brooks N.H. and Imboden D.M. (1992). Bubble plume modeling for lake restoration. *Wat. Resour. Res.*, 28, 3235-3250.

Exhibit D

Linear bubble plume model for hypolimnetic oxygenation: Full-scale validation and sensitivity analysis

V. L. Singleton,¹ P. Gantzer,¹ and J. C. Little¹

Received 23 December 2005; revised 12 June 2006; accepted 21 November 2006; published 8 February 2007.

[1] An existing linear bubble plume model was improved, and data collected from a full-scale diffuser installed in Spring Hollow Reservoir, Virginia, were used to validate the model. The depth of maximum plume rise was simulated well for two of the three diffuser tests. Temperature predictions deviated from measured profiles near the maximum plume rise height, but predicted dissolved oxygen profiles compared very well with observations. A sensitivity analysis was performed. The gas flow rate had the greatest effect on predicted plume rise height and induced water flow rate, both of which were directly proportional to gas flow rate. Oxygen transfer within the hypolimnion was independent of all parameters except initial bubble radius and was inversely proportional for radii greater than approximately 1 mm. The results of this work suggest that plume dynamics and oxygen transfer can successfully be predicted for linear bubble plumes using the discrete-bubble approach.

Citation: Singleton, V. L., P. Gantzer, and J. C. Little (2007), Linear bubble plume model for hypolimnetic oxygenation: Full-scale validation and sensitivity analysis, *Water Resour. Res.*, 43, W02405, doi:10.1029/2005WR004836.

1. Introduction

[2] Bubble plumes are used in a variety of industrial and environmental applications including mixing in chemical reactors, stripping of dissolved gases, containment of spills, prevention of ice formation, protection of harbors from damaging waves [Fanneløp *et al.*, 1991], and destratification of lakes and reservoirs [Schladow, 1992]. In addition to airlift aerators [Burris *et al.*, 2002] and Speece cones [McGinnis and Little, 1998], bubble plumes are commonly used for hypolimnetic aeration and oxygenation, which preserves stratification of water bodies while adding oxygen to the deepest layer. Hypolimnetic anoxia negatively affects the drinking water treatment process, cold-water fisheries, and water quality downstream of hydropower reservoirs. In the United States, releases from hydropower reservoirs typically must comply with state water quality criteria for minimum dissolved oxygen (DO) concentrations [Peterson *et al.*, 2003]. Oxygen depletion may lead to increases in hydrogen sulfide, ammonia, and phosphorus and the release of reduced iron and manganese from the sediments. Hydrogen sulfide, iron, and manganese in drinking water usually require additional treatment [Cooke and Carlson, 1989]. Finally, hypoxia can affect sex differentiation and development in fish, resulting in male-dominated populations with reduced reproductive success [Shang *et al.*, 2006].

[3] A bubble plume model to predict oxygen transfer from linear diffuser systems was presented by McGinnis *et al.* [2001], based on the model for a circular diffuser developed earlier by Wüest *et al.* [1992]. While several

models for point-source or circular bubble plumes have been proposed [Asaeda and Imberger, 1993; Brevik and Kluge, 1999; Ditmars and Cederwall, 1974; Fanneløp and Sjøen, 1980; Johansen, 2000; Kobus, 1968; McDougall, 1978; Milgram, 1983; Rayyan and Speece, 1977; Sahoo and Luketina, 2003; Schladow, 1992; Wüest *et al.*, 1992; Zheng *et al.*, 2002], less work has been conducted on linear (also referred to as line, two-dimensional, or planar) bubble plumes. Kobus [1968] developed one of the first analytical models for linear bubble plumes, which uses an empirical correlation to calculate buoyancy flux. Ditmars and Cederwall [1974] presented a model similar to that of Kobus [1968] but included bubble slip velocity. Brevik [1977] proposed a phenomenological theory for two-dimensional bubble plumes comparable with that of Ditmars and Cederwall [1974], except that kinetic energy was used to predict entrainment. Wilkinson [1979] proposed that full-scale linear plumes could be characterized by a Weber number. Laureshen and Rowe [1987] presented a model for two-dimensional bubble plumes in which plume spreading, entrainment, and momentum amplification were assumed to be functions of the plume Weber number and empirical constants. Fanneløp *et al.* [1991] developed a model for linear plumes in shallow water and studied the resulting surface currents and recirculation cells. Last, Brevik and Kluge [1999] expanded an existing model for linear bubble plumes to account for vertical turbulence. Although much insight into plume dynamics was gained, none of these models for linear or two-dimensional bubble plumes accounted for ambient stratification or gas transfer. The first linear bubble plume model to include gas transfer was presented by McGinnis *et al.* [2001], who converted the circular bubble plume model of Wüest *et al.* [1992] to linear geometry. The incorporation of gas transfer is critical because the rapid dissolution rate of oxygen, and nitrogen

¹Department of Civil and Environmental Engineering, Virginia Polytechnic Institute and State University, Blacksburg, Virginia, USA.

when compressed air is used, strongly influences the buoyancy of the plume [Wiëst *et al.*, 1992]. Gas transfer is especially important in deep water bodies and for weak plumes because the increased contact time allows greater gas exchange. Last, the prediction of oxygen addition from hypolimnetic oxygenation systems is facilitated. Despite the usefulness of the linear bubble plume model, it has not yet been validated at full scale and over a range of operating conditions.

[4] Using extensive, high-spatial-resolution conductivity and temperature as a function of depth (CTD) transect data collected in Spring Hollow Reservoir (SHR), Virginia, during diffuser operation in 2003 and 2004, the performance of the linear bubble plume model is evaluated. The motivation for this work includes verification of model performance prior to use for design and investigation of critical model parameters through sensitivity analysis. Also, the accuracy of model predictions for depth of maximum plume rise (DMPR) and induced water flow rate should be assessed prior to coupling with lake/reservoir hydrodynamic and water quality models, such as CE-QUAL-W2 [McGinnis *et al.*, 2001]. In this paper an improved linear bubble plume model is presented, observations and model predictions are compared, and results of a sensitivity analysis are discussed.

2. Bubble Plumes in Stratified Water Bodies

[5] During hypolimnetic oxygenation with bubble plumes, compressed gas is continually supplied to diffusers, usually located immediately above the sediments, and is allowed to bubble freely. A gas-water plume mixture that is less dense than the ambient water is created, which causes the mixture to ascend through the hypolimnion. As the mixture rises, ambient water is entrained into the plume, and the plume width increases. The entrained fluid produces a double-plume structure, consisting of an inner core that contains the bubble-water mixture surrounded by an outer annulus that contains plume water relatively free of bubbles [McDougall, 1978]. As the outer annulus entrains stratified hypolimnetic water, the plume width increases and the density decreases. When the negative buoyancy of the entrained fluid exceeds the positive buoyancy imparted by the bubbles, the plume detains water at a rate nearly equal to that previously entrained [Lemckert and Imberger, 1993]. At this depth, the velocity of the relatively dense water within the plume decreases to zero, and the plume stops rising. The detraining plume water then forms an annular downward flow immediately outside the outer annulus of the upward flowing plume water. The detraining plume water entrains ambient water until a depth of neutral buoyancy is reached, where a horizontal intrusion is created into the hypolimnion [Asaeda and Imberger, 1993]. The undissolved bubbles remaining in the bubble-water mixture separate from the inner core flow and continue to rise to the surface, repeating the entire process.

3. Linear Bubble Plume Model

[6] The linear bubble plume model utilizes the discrete-bubble approach, which has also been applied to the airlift aerator and Speece cone and was recently reviewed in detail by Singleton and Little [2006]. The linear bubble plume

model is composed of horizontally integrated equations based on the conservation of mass, momentum, and heat. Eight flux equations are solved simultaneously to predict water flow rate, plume temperature, oxygen and nitrogen transfer and concentration, salinity, and plume rise height, given diffuser geometry and depth, applied gas flow rate, and initial bubble size (Tables 1 and 2). The model accounts for density stratification due to vertical temperature and salinity gradients. Entrainment is assumed to be proportional to the local (with respect to depth) plume water velocity and perimeter. Bubble size varies as the bubbles rise due to expansion and dissolution, and bubble slip velocity and gas transfer coefficients are functions of bubble radius [Wiëst *et al.*, 1992]. Also, Henry's constants for oxygen and nitrogen are functions of temperature [Wiëst *et al.*, 1992]. The bubble plume model equations were originally developed by Wiëst *et al.* [1992] for circular geometry but were modified by McGinnis *et al.* [2001] for the linear geometry of the system installed in SHR. The equations that include the spreading coefficient (λ) were recently refined [Singleton and Little, 2005] to more accurately reflect the geometry of the plume at the ends of the linear diffuser (Tables 1 and 2), which is approximated in plan view as a long, thin rectangle. Additional refinements to the model of McGinnis *et al.* [2001], which are detailed in the following paragraphs, include use of a correlation to calculate initial bubble size [McGinnis and Little, 2002], correction of the entrainment coefficient (α) and λ for top-hat profiles, and use of a Froude number (Fr) to calculate initial water velocity [Fischer *et al.*, 1979; Wiëst *et al.*, 1992]. Also, water quality profiles from the plume near-field, as opposed to the reservoir far-field, were used as boundary conditions [McGinnis *et al.*, 2004].

[7] The entrainment coefficient and λ were set at 0.11 and 0.93, respectively. These values were derived by Fanneløp *et al.* [1991] by fitting Gaussian profiles to laboratory data and were modified for the top-hat profile assumption of the model using [Fanneløp and Sjøen, 1980]

$$\alpha_T = \sqrt{2} \alpha_G \quad (1)$$

$$\lambda_T = \sqrt{\frac{\lambda_G^2 + 1}{2}}, \quad (2)$$

where the subscripts T and G refer to top-hat and Gaussian profiles, respectively. For simplicity, top-hat or uniform profiles are assumed for water velocity, temperature, salinity, dissolved and gaseous constituents, and bubble velocity [Wiëst *et al.*, 1992]. Other model assumptions are as follows: (1) The linear plume width W for temperature and dissolved constituents is equal to the width of the plume velocity profile, whereas the bubbles are confined to an inner core of width λW ($\lambda < 1$); (2) ambient currents are negligible; (3) the diffuser produces bubbles at a constant rate and uniform size that are evenly distributed over the cross section of initial width λW_0 ; (4) bubble coalescence is neglected; (5) initial water properties of the plume are those of ambient water at the diffuser depth; and (6) exchange of gases other than oxygen and nitrogen is not considered.

[8] The model predictions are strongly dependent on the initial plume conditions and the plume boundary conditions

Table 1. Key Variables of the Linear Bubble Plume Model^a

Variable	Formula	Units
Entrainment factor	$E = 2(L + W)\alpha v$	m^2/s
Plume water volume flux	$Q = LWv$	m^3/s
Momentum flux	$M = LWv^2$	m^4/s^2
Temperature flux	$F_T = QT_p$	$^\circ\text{C m}^3/\text{s}$
Dissolved solids flux	$F_s = QS\rho_w$	kg/s
Dissolved O ₂ and N ₂ fluxes	$F_{D_i} = QC_i$	mol/s
Gaseous O ₂ and N ₂ fluxes	$F_{G_i} = \lambda W[L - W(1 - \lambda)](v + v_b)v_i$	mol/s

^aRevised from McGinnis et al. [2001].

of temperature, dissolved oxygen, and salinity. Initial conditions for the bubble plume model were determined as detailed by Wüest et al. [1992], except for the following deviations. Initial bubble size is calculated using the correlation developed by McGinnis and Little [2002] for the type of linear diffuser installed in SHR:

$$d_{3,2} = 1.12 + 0.938q. \quad (3)$$

The correlation was determined using measured Sauter-mean bubble diameter ($d_{3,2}$) values of 1.1–2.2 mm collected over actual unit gas flow rates q of 0.08–0.88 m^2/h at the diffuser.

[9] For the circular bubble plume model, Wüest et al. [1992] proposed that the induced vertical water velocity v at the diffuser depth is equivalent to the initial plume water velocity. To estimate the initial velocity, Wüest et al. [1992] defined a densimetric Fr and utilized a relationship between the local Richardson number (Ri) and Fr derived by Fischer et al. [1979] for single-phase, round buoyant jets discharging vertically. The circular bubble plume model was recently validated by McGinnis et al. [2004], so a similar procedure was used to determine the initial plume velocity for the linear bubble plume. Corresponding equations for Fr were derived for planar or linear plumes using relationships presented by Fischer et al. [1979] to obtain

$$Fr = Ri^{-\frac{1}{4}} \quad (4)$$

$$Fr = \frac{v}{[\lambda Wg(\rho_a - \rho_p)/\rho_p]^{\frac{1}{2}}}, \quad (5)$$

where g is gravitational acceleration, ρ_a is the ambient water density, and ρ_p is the bubble plume density. The local Ri for planar jets has a constant value of 0.735 at distances from

the source where the flow is more like a plume [Fischer et al., 1979]. Consequently, Fr for a planar or linear plume is equal to 1.26, except close to the source. Wüest et al. [1992] assumed that the bubble slip velocity near the source was relatively low, so the initial Froude number (Fr_o) should be equal to the value for a single-phase plume. Unlike the circular plume model, the Fr profiles predicted by the linear bubble plume model continually increase with depth for the diffuser installed in SHR (not shown). For $Fr_o \leq 2.0$, the plume velocity initially increases with decreasing depth immediately above the linear diffuser (Figure 1a). This effect was also predicted by Fanneløp and Webber [2003] for buoyant plumes rising from areal sources, where a point of maximum velocity occurred above the source. Additionally, the plume neck (point of minimum radius or width) is always below the point of maximum velocity in the plume [Fanneløp and Webber, 2003]. A neck is not predicted for the linear bubble plume when $Fr_o = 2.0$ (Figure 1b). However, necking or contraction will only occur when the momentum immediately above the source is relatively low and/or the entrainment coefficient is relatively low [Fanneløp and Webber, 2003]. Also, Wüest et al. [1992] reasoned that a plume from an open source (diffuser above sediments) may not contract because initially entrained water is not obstructed. Therefore Fr_o for an open source will likely be higher than that for a closed source (diffuser resting on sediments). Because the linear diffuser in SHR is an open source (Figure 2), Fr_o for the linear bubble plume was assumed to be 2.0, and a sensitivity analysis was conducted to determine the effect of varying Fr_o .

[10] The differential flux equations of the linear bubble plume model (Table 2) were solved numerically using the fourth-order Runge-Kutta method. Further information on the general solution procedure, equations of state, and model assumptions is provided by Wüest et al. [1992] and McGinnis et al. [2004]. The model calculations are only valid over the plume rise height, up to the DMPR. When the plume stops rising, a secondary plume may form above as bubbles that are not completely dissolved continue to rise [Asaeda and Imberger, 1993; McDougall, 1978; Schladow, 1992]. This phenomenon can occur when a bubble plume is released into strong density stratification.

4. Application to Spring Hollow Reservoir, Virginia

4.1. Field Data Collection

[11] To fully evaluate the linear bubble plume model, experimental data for boundary conditions, rise height, and in-plume constituent profiles are required. Testing was

Table 2. Nonlinear Differential Flux Equations of the Linear Bubble Plume Model^a

Flux	Equation
Water volume	$dQ/dz = E$
Momentum	$dM/dz = [(\rho_a - \rho_p)/\rho_p]gLW + [(\rho_w - \rho_p)/\rho_p]g\lambda W[L - W(1 - \lambda)]$
Temperature	$dF_T/dz = ET_a$
Salinity	$dF_J/dz = EP_aS_a$
Dissolved gas	$dF_{D_i}/dz = EC_a + [4\pi r^2 N(v + v_b)]K_L(H_iP_i - C_i)$
Gas	$dF_{G_i}/dz = -[4\pi r^2 N(v + v_b)]K_L(H_iP_i - C_i)$

^aRevised from McGinnis et al. [2001].

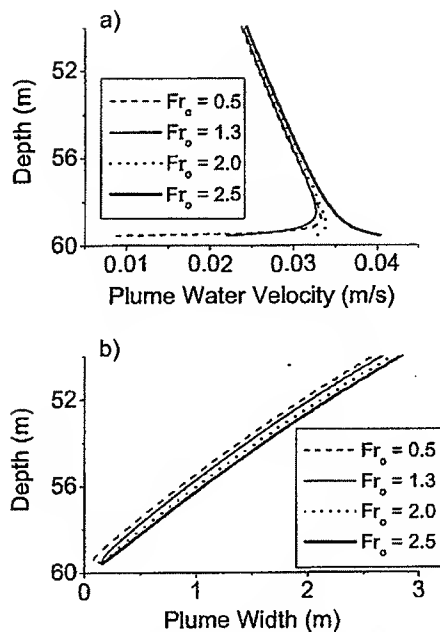


Figure 1. Effect of initial Froude number (Fr_o) on predictions of plume water velocity and plume width using linear bubble plume model.

conducted using a full-scale linear diffuser (Figure 2) installed in Spring Hollow Reservoir, Virginia (Figure 3). Constructed in 1995, SHR is a small monomictic, mesotrophic side-stream reservoir that is generally stratified from May to December. The reservoir is managed by the Western Virginia Water Authority and serves as one of the principle drinking water sources for Roanoke County. The water body has a maximum depth of 65 m and a maximum surface elevation of 431 m. The approximate surface area and volume are 0.54 km^2 and $12.4 \times 10^6 \text{ m}^3$, respectively. To prevent anoxia in the hypolimnion and the associated deterioration of raw water quality, a linear diffuser equipped with fine-bubble porous hoses was installed in 1997 (Figure 3). The 305-m-long diffuser can be supplied with compressed air or pure oxygen at various gas flow rates and is located in the deepest portion of the reservoir (368–372 m elevation). On the basis of an average surface elevation of 430 m, the depth of the diffuser during testing ranged from 58 to 62 m along its length. Table 3 provides the diffuser operating parameters in 2003 and 2004.

[12] Diffuser tests were performed in 2003 using compressed air (21% O₂) supplied at a high gas flow rate (45 Nm³/h average) during 29 June to 14 July and pure oxygen (97% O₂) supplied at a low flow rate (11 Nm³/h average) during 14–26 August. A third test was conducted in 2004 using pure oxygen, but at a higher gas flow rate (40 Nm³/h maximum) during 22 October to 5 November. In 2003, the diffuser quickly mixed the rather small hypolimnetic volume during both tests, and the water quality conditions on the dates of data collection (2 July and 17 August for compressed air and pure oxygen, respectively) were by that time relatively homogeneous as a result of plume-induced mixing. One of the primary objectives of the 2004

experiments was to maximize the plume signature in the hypolimnion and to increase confidence in the linear plume model validation under a different set of boundary conditions. In 2004, the data were therefore collected on 24 October, soon after start of diffuser operation. Additionally, the 2004 test was performed later in the stratified season to maximize the ambient DO and temperature gradients in the hypolimnion.

[13] To establish appropriate boundary conditions for the plume model, characterization of the plume near-field environment is necessary [McGinnis et al., 2004]. Therefore the data collected included numerous high-spatial-resolution CTD (Sea-Bird model SBE 19plus; 4-Hz sampling rate) transects measured almost daily before, during, and after diffuser operation. The CTD profiler was also equipped with a DO probe (1.4-s response time measured at 20°C). Profiles were obtained laterally across the diffuser at 0.5-m increments for 0–10 m, 2-m increments for 10–20 m, and 5-m increments for 20–40 m from the centerline of the diffuser in both directions (Figures 3 and 4). (The diffuser centerline location is shifted to the left for 2004 (Figures 4e and 4f) because the diffuser was repositioned earlier in the year. Also, the operational length of the diffuser was decreased for that year (Table 3).)

[14] The geometry of SHR affects the extent and rate of circulation within the hypolimnion induced by the bubble plume. Because of the relatively small size of SHR, operation of the linear diffuser created uniform conditions below the thermocline within days after startup. While SHR bathymetry influences plume-induced mixing in the hypolimnion, the effect on short-term plume operation is negligible because the time that individual bubbles spend in the hypolimnion is of the order of minutes. The bubbles and resulting plume experience a pseudo steady state with respect to ambient conditions. Effects on data collection due to the ends of the linear diffuser were assumed to be negligible because the lateral profile location was over 150 m from a diffuser end (Figure 3), and the diffuser is designed to release a uniform gas flow along its length.

4.2. Observations and Model Validation

[15] Plume rise height, spreading, and constituent profiles predicted by the linear bubble plume model were compared with experimental observations. Critical model input parameters for the three test conditions (2 July 2003, 17 August 2003, and 23 October 2004) are shown in Table 3. The boundary conditions were obtained from averaged near-field lateral profiles [McGinnis et al., 2004] (± 2 m and ± 1 m from plume centerline for 2003 and 2004, respectively) and differed significantly between 2003 and 2004 (Figure 5). (The presence of two thermoclines in 2003 is due to the pumped reservoir inflow that discharges at 396-m elevation, which corresponded to approximately 34-m depth during diffuser testing. The lower thermocline delineates the effective hypolimnion for the oxygenation system.)

[16] Measured contours of temperature and DO are shown in Figure 4, along with corresponding model predictions for plume width and the DMPR. The actual plume boundaries are not well defined in the contour plots, so comparison with predicted plume widths is difficult. The lack of distinct plume boundaries was due to the almost well mixed conditions in the hypolimnion as a result of diffuser

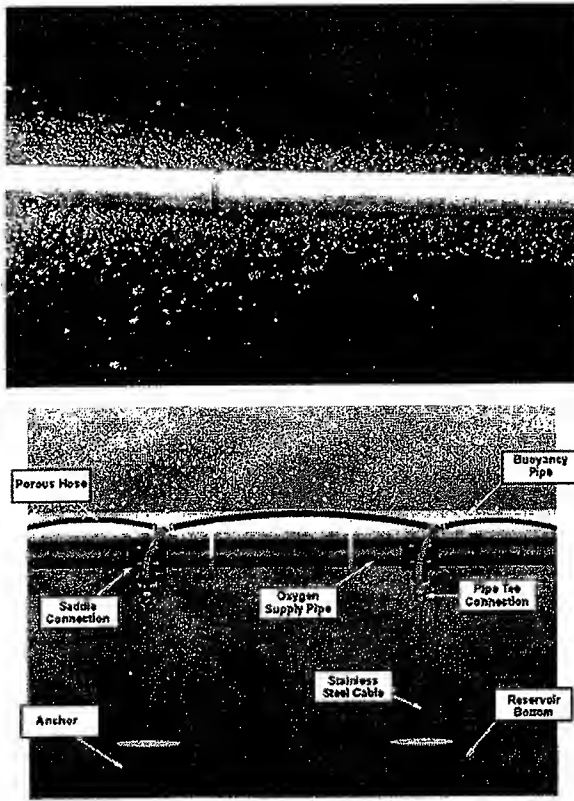


Figure 2. Photograph and schematic of linear bubble plume diffuser in Spring Hollow Reservoir, Virginia. Courtesy of Mark Mobley, Mobley Engineering, Inc.

operation, particularly for 2003 (Figures 4a–4d). Also, use of compressed air did not produce a strong DO plume signature for the July test compared with the August and October tests with pure oxygen. The actual plume rise height is easier to distinguish, especially in the DO contours for August and October. The predicted depths of maximum plume rise are 38.2, 46.1, and 48.8 m for July, August, and October, respectively. For July and October, the DMPR is simulated well by the model (Figures 4a, 4b, 4e, and 4f). However, the model appears to underestimate the plume rise height for August, when the gas flow rate was comparatively low (Table 3). The under-predicted DMPR may have been due to an overestimated value for α . In a detailed study of round plumes, Milgram [1983] found that α is directly proportional to the plume gas holdup or fraction. However, the linear bubble-plume model assumes that α is constant (Table 3).

[17] The structure of the plumes is similar to those observed by Asaeda and Imberger [1993] for round bubble plumes in weak stratification (Figure 4). Depending on the gas flow rate and stratification strength, three types of horizontal intrusions from the plume were reported. The pattern of the DO contours for October (Figure 4f) closely resembles type 1, which corresponds to a high gas flow rate or weak stratification [Asaeda and Imberger, 1993]. This is similar to a single plume impinging on a free surface, which

is analogous to the thermocline in SHR. Although the plume for July is not easily discerned from the temperature or DO contours, the structure is most likely similar to a type 1 plume. The July plume appears to detrain primarily at the lower thermocline with one strong intrusion, as evidenced by accumulation of higher oxygenated water near the top of the plume (Figure 4b). The plume for August is best classified as type 3, which is for low gas flow rates or strong density stratification [Asaeda and Imberger, 1993]. Type 3 plumes do not have steady intrusions, but instead are characterized by alternating, collapsing eddies that cause the plume to meander.

[18] Referring to the October test (Figure 4f), the higher DO concentrations at lower depths adjacent to both sides of the plume were likely the result of detrained water that sinks past the equilibrium depth due to momentum. The temperature isotherms were also depressed immediately beside the plume (Figure 4e). This phenomenon was also observed by McGinnis et al. [2004]. The DO concentration immediately above the predicted DMPR and near the vertical plume centerline for October 2004 is higher than the ambient concentration (Figure 4f). This could have been caused by the formation of a secondary plume above the DMPR resulting from incompletely dissolved bubbles. The model estimates that the bubble size at the top of the first plume was about 5×10^{-5} m for October 2004, which is relatively large compared with July 2003 and August 2003 (Figure 6f). These undissolved bubbles could have created a secondary plume, which entrained oxygenated water from the detrainment of the first plume and carried it higher into the water column.

[19] Vertical profiles of constituents and properties within the plumes were also predicted for the three diffuser tests (Figure 6). For the July test with compressed air, the higher gas flux creates a greater buoyancy flux and a higher initial plume water velocity (Figure 6d). Also, the concentration driving force for oxygen transfer is lower compared with pure oxygen, which decreases the rate of bubble dissolution with depth (Figure 6f). These effects result in a higher DMPR for July compared with August (Figures 4 and 6). The model predictions for 2004 differ from those of 2003 because of the differing boundary conditions (Figure 5). The plume rise height for the October test with pure oxygen is less than that for August, even though the gas flux was more than tripled (Table 3). The ambient temperature, and hence density, stratification was stronger in 2004, which provided greater negative buoyancy to decrease plume momentum. The stronger ambient density stratification also caused the plume velocity to decrease more rapidly with depth in 2004 despite a higher initial velocity from the diffuser (Figure 6d). The lower plume rise height in October resulted in lower plume water flow rates than July (Figure 6e), even with comparable gas fluxes applied (Table 3).

[20] Average temperature, DO, and density profiles within the plumes were also measured (Figures 6a–6c). The temperature, and consequently density, predictions for July and October deviate from the measured profiles where the plumes reach the top of the hypolimnion (Figures 6a and 6c), or where the rate of plume spreading is greatest (Figure 4). The model underpredicts the final plume temperature by approximately 0.3° and 0.2°C for July and October, respectively. One reason for the discrepancy

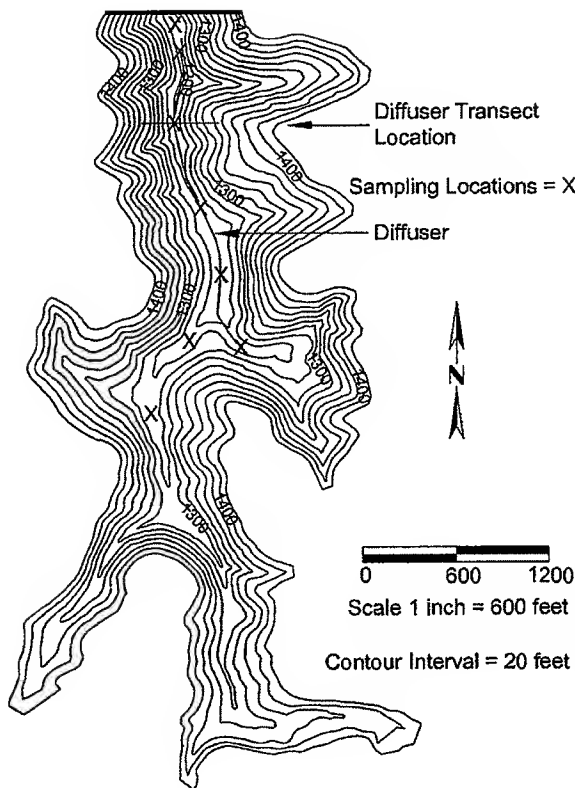


Figure 3. Bathymetric map of Spring Hollow Reservoir, Virginia, showing locations of linear bubble plume diffuser and conductivity-temperature-depth (CTD) lateral transects.

may be that the model assumes α is constant. In addition to the dependence on plume gas holdup, Milgram [1983] also found that α for a circular plume is directly proportional to the local plume radius. As the plume approaches its maximum rise height, the width increases rapidly

(Figure 4). If linear plume dynamics are similar to circular plumes, then α for linear plumes may also increase as the plume width increases. Additionally, the boundary profiles selected may not accurately reflect the actual ambient conditions immediately adjacent to the plume along its entire rise height. Measured vertical CTD profiles at the estimated plume width were averaged and used for boundary conditions. However, the plume width varies greatly with depth (Figure 4), so use of vertical profiles at a single lateral distance from the diffuser is not appropriate. Also, the average plume width was visually estimated from the temperature and DO contour plots (Figure 4), but the actual plume boundaries are not well defined.

[21] The model predicts the plume DO profiles well for all three diffuser tests (Figure 6b). For July and August the model characterizes the initial increase in DO immediately above the diffuser quite accurately. The initial rapid increase in DO for August and October is due to the higher oxygen saturation concentration at depth with the use of pure oxygen. The high hydrostatic pressure causes the oxygen transfer rate to be almost independent of the ambient DO concentration at the depth of diffuser. By contrast, the initial DO increase for the July test with compressed air is more modest (Figure 6b). The shape of the predicted DO profile for October differs somewhat from the experimental data, even though the final values at the DMPR differ by only 0.3 g/m³. The hypolimnion and hence the plume near-field were more heterogeneous in 2004 than 2003, which may have contributed to the overprediction at lower depths if the selected boundary profiles did not accurately represent water entrained into the plume.

[22] Another source of inaccuracy could be the correlation equation used to calculate initial bubble size (equation (3)). This relationship was developed using data collected over actual air flow rates per unit length of diffuser of 0.08–0.88 m²/h [McGinnis and Little, 2002]. The actual gas flow rates per unit length of diffuser for the July, August, and October tests were 0.019, 0.0063, and 0.024 m²/h, respectively. Therefore the initial bubble diameters used in the model were extrapolated beyond the valid correlation range.

Table 3. Conditions for Linear Bubble Plume Model Validation and Sensitivity Analysis for Spring Hollow Reservoir, Virginia^a

Parameter	2 July 2003	17 Aug 2003	23 Oct 2004	Sensitivity Range
Oxygen in gas supply, %	21	97	97	n/a
Entrainment coefficient []	0.11	0.11	0.11	0.05–0.2
Spreading coefficient []	0.93	0.93	0.93	0.5–1.0
Initial Froude number []	2.0	2.0	2.0	1.0–3.0
Operational diffuser length, m	300	300	250	60–625
Initial plume width, m	0.16	0.16	0.16	n/a
Initial plume area, m ²	50	50	42	10–100
Gas flow rate, ^b Nm ³ /h	38	13	40	1–400
Initial gas flux, ^c m/h	0.76	0.26	0.96	0.02–9.5
Initial bubble radius, m	5.7×10^{-4}	5.6×10^{-4}	5.7×10^{-4}	$10^{-4}–10^{-1}$
Diffuser depth, ^d m	60	60	59	n/a
Reservoir maximum depth, m	64	65	64	n/a
Reservoir surface area, 10 ⁶ m ²	0.53	0.53	0.53	n/a
Reservoir total volume, 10 ⁶ m ³	12	12	12	n/a

^aReservoir conditions on testing days are also included.

^bNm³ denotes 1 m³ of gas at 1 bar and 0°C.

^cSensitivity analysis range refers to varying gas flow rate while maintaining constant initial plume area.

^dDepth at location of lateral CTD transect.

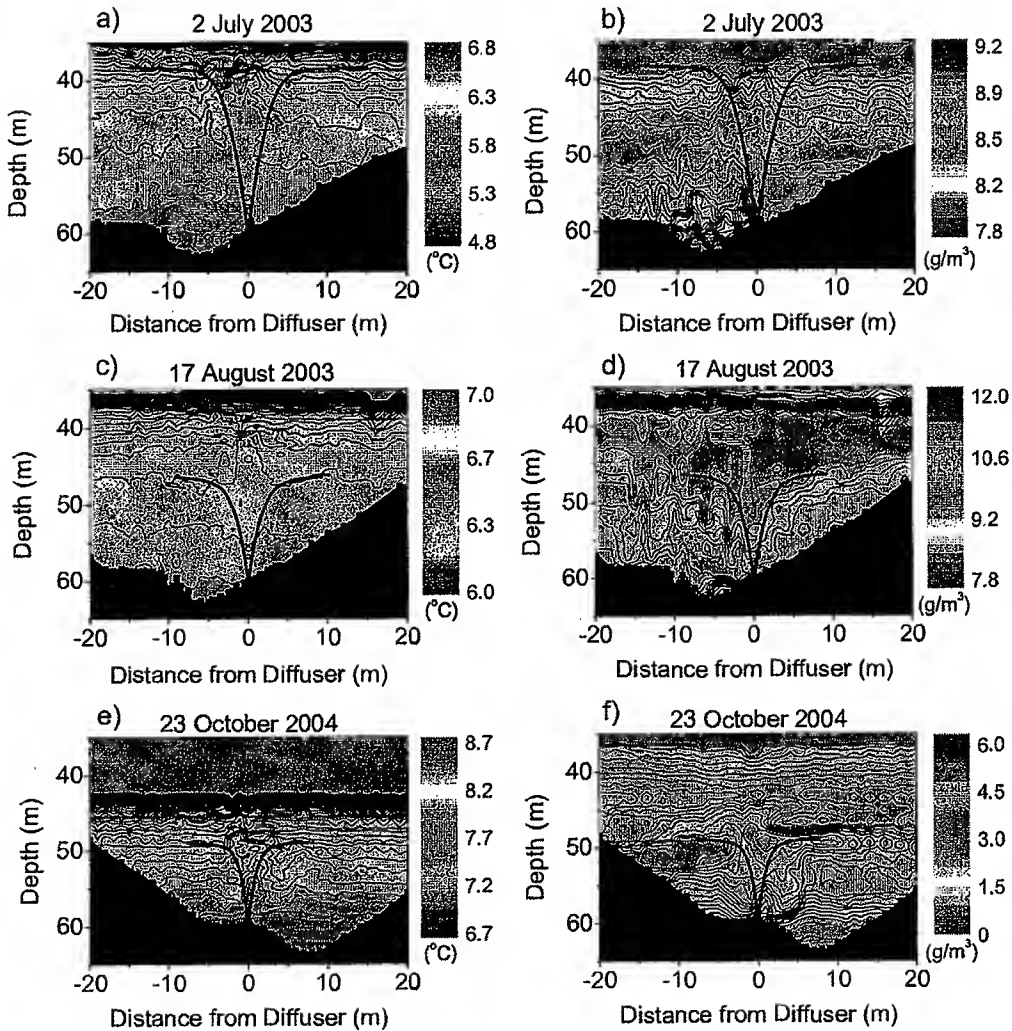


Figure 4. Measured (left) plume temperature ($^{\circ}\text{C}$) and (right) dissolved oxygen (DO) (g/m^3) contours with linear bubble plume model predictions for diffuser operation with air (2 July 2003) and pure oxygen (17 August 2003 and 23 October 2004) in Spring Hollow Reservoir, Virginia. Contours were interpolated from CTD profiles collected at locations indicated by small black squares along the bottom of each plot.

4.3. Sensitivity Analysis

[23] A sensitivity analysis was performed with the linear bubble plume model to determine the effects on plume rise height, oxygen transfer efficiency, and induced water flow rate, because these parameters are important for design and operation of hypolimnetic aeration/oxygenation systems. Parameter perturbation was used, in which input variables are independently adjusted to determine their individual effects on model predictions. The model variables investigated are either difficult to measure or can be controlled through system design or operation (Table 3). Currently, α and λ for the linear plume model are empirical constants [Fanneløp *et al.*, 1991], and the initial plume water velocity is calculated using a densimetric Fr [Wiest *et al.*, 1992]. The initial plume area, gas flow rate, and, to a lesser extent, initial bubble size can be controlled through diffuser design and operation. The sensitivity of model predictions to

ambient dissolved nitrogen was also examined for the standard case using compressed air (2 July 2003). The model assumes that the background dissolved nitrogen concentration is equivalent to the saturated value at atmospheric partial pressure and the average hypolimnetic water temperature.

[24] The DMPR is most influenced by gas flow rate and initial bubble radius (Figures 7e and 7f). The gas flow rate is directly related to the density of the plume bubble-water mixture and subsequently the positive buoyancy and upward momentum of the plume (Table 2). For gas flow rates greater than approximately $100 \text{ Nm}^3/\text{h}$, the plume rise height is controlled more by the depth of the thermocline in SHR (Figure 5a). As the plume rise height approaches the thermocline, further increases in the buoyancy and momentum fluxes can not overcome the strong ambient density stratification. The 2003 predictions are more a function of

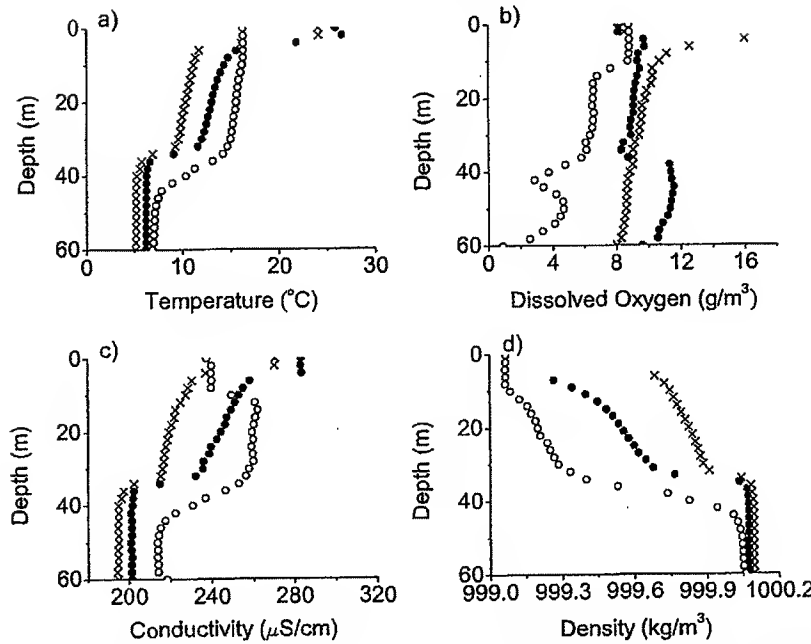


Figure 5. Input boundary conditions for linear bubble plume model validation and sensitivity analysis. Data collected from Spring Hollow Reservoir, Virginia, during diffuser operation with compressed air (2 July 2003, crosses) and pure oxygen (17 August 2003, solid circles, and 23 October 2004, open circles).

gas flow rate than those for October 2004 because of differing boundary conditions (Figure 5).

[25] The plume rise height is moderately sensitive to initial bubble radius (Figure 7f). For initial radii less than about 1 mm, the DMPRs are nearly independent of bubble size. As initial bubble sizes increase, the plumes ascend higher and reach a maximum height for a radius of about 6 mm for each diffuser test. The shapes of the curves can be attributed to the dependence of bubble rise velocity and gas transfer coefficients on bubble radius [Wüest *et al.*, 1992]. The DMPR predictions for August are more sensitive to initial bubble radius than those for July and October (Figure 7f). The plume on 17 August 2003 did not have sufficient buoyancy and momentum to rise to the thermocline because a relatively low gas flow rate was applied (Figure 4c and Table 3). By contrast, the plume dynamics for July and October were influenced to a greater degree by the thermocline, which in effect damped the sensitivity of plume rise height to the initial bubble radius.

[26] The predicted DMPR for the linear bubble plume is virtually independent of Fr_o and λ over the ranges analyzed (Figures 7b and 7c). The plume rise height is moderately sensitive to α . Entrainment into the plume is a function of plume size, water velocity, and α (Table 1), and entrainment of ambient water decelerates the plume. Plume rise is influenced to a somewhat greater degree by the initial plume area. As the plume area is increased, the buoyancy flux decreases because the gas flow rate is constant. Plume rise height was unaffected by variations in the ambient dissolved nitrogen concentration from 50 to 200% saturation in the hypolimnion for the 2 July 2003 diffuser test. Similar to the analysis for DMPR, induced water flow rate at the top of the plume was found to be insensitive to Fr_o and λ and

somewhat more sensitive to α and the initial plume area (results not shown). Plume water flow rate is most influenced by gas flow rate and initial bubble radius. Higher gas flow rates produce greater buoyancy and momentum fluxes, which results in greater plume rise heights and increased entrainment.

[27] Oxygen transfer efficiency (total mass of oxygen transferred relative to initial mass of oxygen in bubbles) within the hypolimnion was independent of all parameters except initial bubble radius, decreasing from nearly 100% to around 20% for air and pure oxygen as the initial radii increased from approximately 1 mm to 1 cm (Figure 8). Oxygen transfer can continue above the DMPR if the bubbles are not dissolved. However, secondary plumes are not accounted for in the model. Even though undissolved bubbles at the top of the plume may continue to transfer oxygen during ascent, the oxygen may not be added at the desired depth (*i.e.*, below the thermocline). A local minimum with respect to induced water flow rate at the top of the plume is predicted for a bubble radius of about 1 mm for the conditions in SHR (not shown). This suggests that while maximum oxygen transfer efficiency can be achieved with a 1-mm initial bubble radius, vertical water circulation, and hence oxygen distribution in the hypolimnion, will not be optimized. As the bubble radius is increased from 1 mm, induced water flow rate increases as well for radii up to 5 mm, but oxygen transfer efficiency decreases rapidly within this range (Figure 8).

5. Comparison of Linear and Circular Bubble Plume Models

[28] The primary difference between the linear and circular bubble plume models is the plume geometry. For a

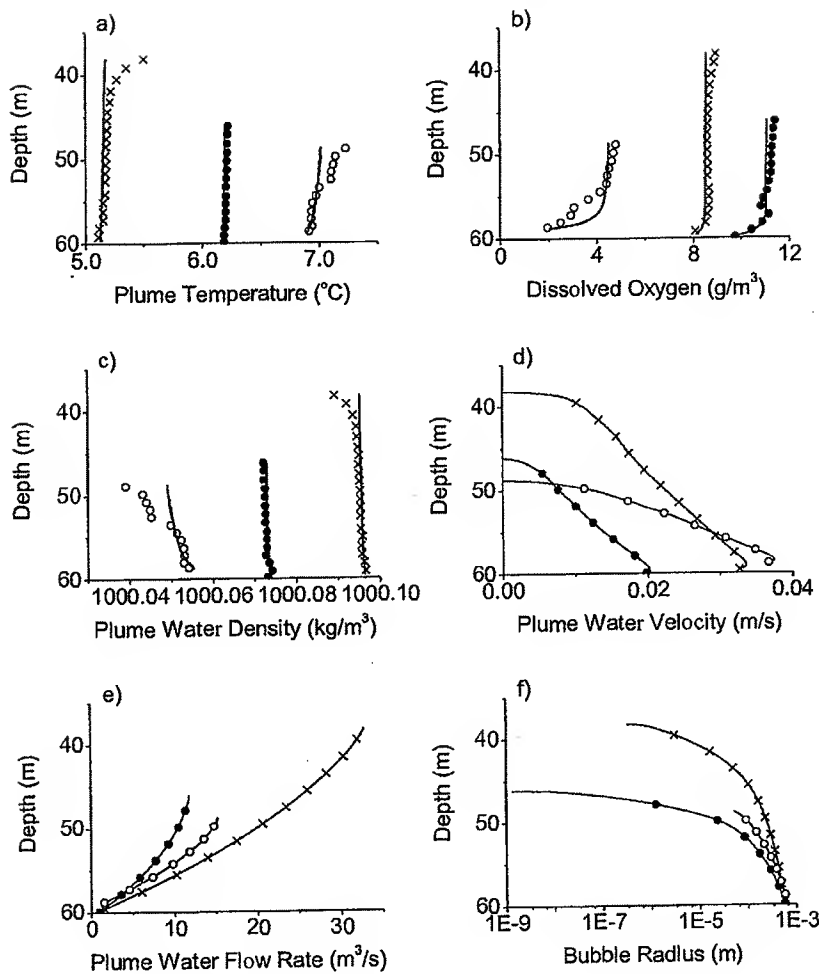


Figure 6. In-plume profiles predicted by linear bubble plume model, represented as (a–c) solid lines and (d–f) solid lines and symbols. Input data collected from Spring Hollow Reservoir, Virginia, during diffuser operation with compressed air (2 July 2003, crosses) and pure oxygen (17 August 2003, solid circles, and 23 October 2004, open circles). Measured average in-plume temperature, DO, and plume water density represented as symbols (Figures 6a–6c).

given plume cross-sectional area, the perimeter of a linear plume is much greater than for a circular or round plume. The initial estimated plume area and perimeter of the linear diffuser in SHR for July 2003 was about 50 m^2 and 600 m, respectively (Table 3). This corresponds to an equivalent radius and perimeter of approximately 4 m and 25 m, respectively, for a circular plume. In this case, the perimeter of the linear plume is 24 times greater than for the circular plume. For both the linear and circular plume models, entrainment of ambient water is directly proportional to local plume perimeter, local plume water velocity, and α (Table 1). The larger perimeter of the linear plume greatly increases ambient entrainment, which contributes to the negative buoyancy of the plume and causes the plume to decelerate more rapidly. This results in a lower plume rise height compared with the circular plume.

[29] The sensitivity of the linear bubble plume model to various parameters was comparable to results for the circu-

lar bubble plume model analysis. Gas flow rate had the greatest effect on DMPR predictions by both models, and the linear plume model was less sensitive to initial bubble radius than the circular plume model was [Wuest *et al.*, 1992]. The latter may be due to differences between temperature boundary conditions, which caused plume dynamics in SHR to be more influenced by thermocline depth. Initial bubble size greatly affected oxygen transfer efficiency for both diffuser geometries, decreasing rapidly as the radii increased beyond 1 mm and 3 mm for the linear and circular plumes, respectively. Both the linear and circular plume model predictions for DMPR were relatively insensitive to Fr_o and initial plume area (Figure 7 and Wuest *et al.* [1992]). However, circular model predictions for DMPR were more sensitive to α . Overall, the linear model was less sensitive to input parameters than the circular model, but this insensitivity is probably due to the relatively

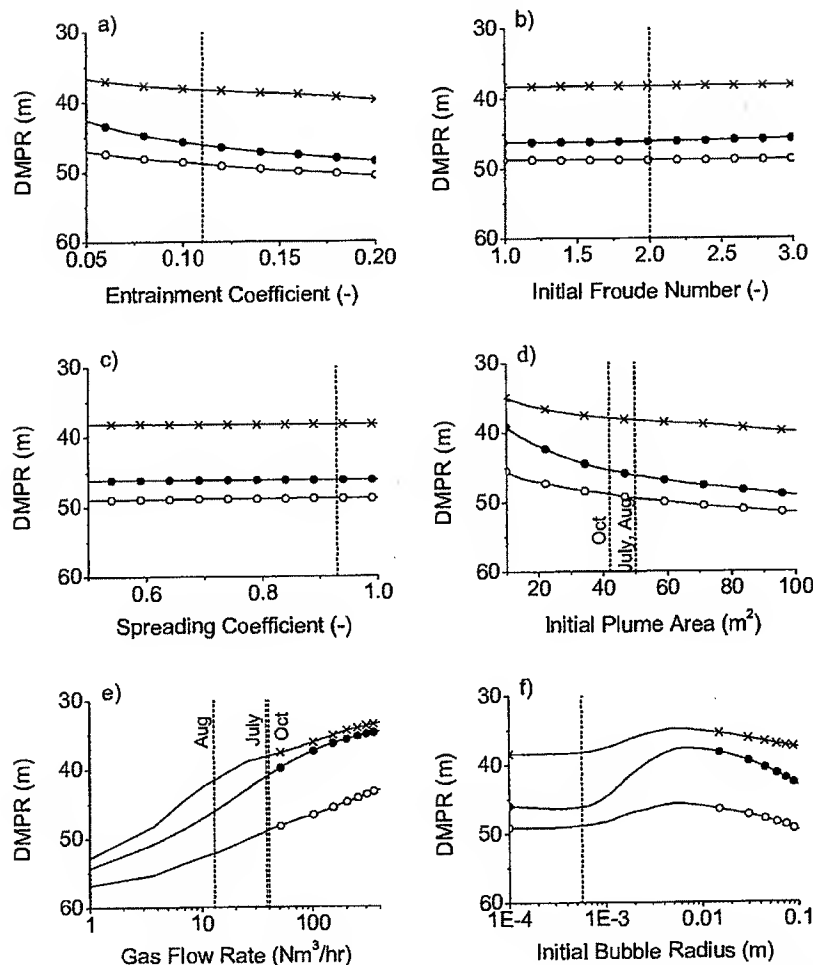


Figure 7. Effect of linear bubble plume model parameters on depth of maximum plume rise (DMPR). Standard values for each parameter are indicated by the vertical dashed lines. Input data collected from Spring Hollow Reservoir, Virginia, during diffuser operation with compressed air (2 July 2003, crosses) and pure oxygen (17 August 2003, solid circles, and 23 October 2004, open circles).

homogeneous boundary conditions in the hypolimnion of SHR caused by diffuser mixing.

6. Summary and Conclusions

[30] In the current work, the linear bubble plume model of McGinnis *et al.* [2001] was improved, and the updated model was evaluated using data collected from a full-scale hypolimnetic oxygenation system installed in Spring Hollow Reservoir, Virginia. Three diffuser experiments were conducted using compressed air and pure oxygen over a range of flow rates. Predicted plume rise height, spreading, and constituent profiles were compared with experimental observations. For July 2003 and October 2004, the DMPR was simulated well by the model. However, the model underestimated the plume rise height for August 2003, when the gas flow rate was comparatively low. The model underpredicted the final plume temperature by approximately 0.3° and 0.2°C for July 2003 and October 2004, respectively. The model predicted the plume DO

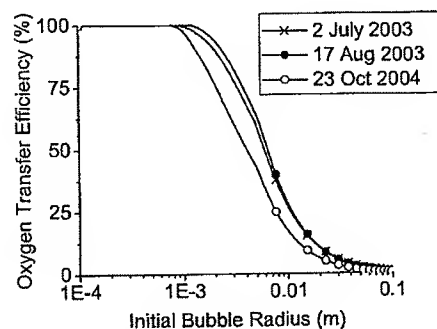


Figure 8. Effect of initial bubble radius on oxygen transfer efficiency predicted by linear bubble plume model. Input data collected from Spring Hollow Reservoir, Virginia, during diffuser operation with compressed air (2 July 2003) and pure oxygen (17 August 2003 and 23 October 2004).

profiles very well for all three diffuser tests, including simulating the initial rapid transfer of oxygen immediately above the diffuser.

[31] A sensitivity analysis was performed to determine the effect of various model input parameters. The DMPR and induced water flow rate were most influenced by gas flow rate and initial bubble radius, moderately sensitive to α and the initial plume area, and insensitive to Fr_o , λ , and ambient dissolved nitrogen. Oxygen transfer within the hypolimnion was independent of all parameters except initial bubble radius, decreasing from nearly 100% to around 20% for air and pure oxygen as the initial radii increased from approximately 1 mm to 1 cm.

[32] The linear bubble plume model for hypolimnetic oxygenation has been successfully validated. The model can be used to design lake and reservoir oxygenation systems and to optimize existing systems to maximize oxygen addition. Application of the linear plume model requires knowledge of the gas flow rate, initial bubble radius, initial plume area, and near-field constituent profiles (boundary conditions). Additionally, several empirical parameters must be estimated including α and λ . Even though all of the model inputs may not be known with certainty for a given aeration or oxygenation system, the model can be used for preliminary design and coarse optimization. Also, plume rise height, water flow rate, and oxygen transfer efficiency were found to be primarily dependent on gas flow rate and initial bubble radius.

[33] Operation of bubble plumes for hypolimnetic oxygenation usually alters the ambient temperature and DO conditions of a water body. Plume dynamics and oxygen transfer are strongly related to the near-field water column properties, establishing a feedback loop that continually changes plume dynamics. This complex plume-lake interaction should be accounted for in the design and operation of bubble plume diffusers. *McGinnis et al. [2001]* performed a preliminary coupling of the linear bubble plume model with an existing reservoir model, CE-QUAL-W2 [*Cole and Wells, 2003*], and obtained encouraging results. Efforts are currently under way to further develop the coupled model to predict plume performance and the near- and far-field reservoir responses. In the absence of near-field boundary profiles, far-field or simulated constituent profiles can be used to provide a reasonable estimate of plume performance.

Notation

b	plume radius (circular bubble plume), m.
d	bubble diameter, mm.
C	dissolved concentration, mol/m ³ .
E	entrainment factor, m ² /s.
F_D	dissolved species flux, mol/s.
F_G	gaseous species flux, mol/s.
F_S	salinity flux, kg/s.
F_T	temperature flux, °C m ³ /s.
Fr	Froude number [].
g	gravitational acceleration, m/s ² .
H	Henry's constant, mol/m ³ /bar.
K_L	mass transfer coefficient, m/s.
L	plume length, m.
M	water momentum, m ⁴ /s ² .

N	number flux of bubbles, 1/s.
P	pressure, bar.
Q	plume flow rate, m ³ /s.
q	actual gas flow rate per unit diffuser length, m ² /h.
Ri	Richardson number [].
R	bubble radius, m.
S	salinity, g/kg.
T	temperature, °C.
v	velocity, m/s.
W	plume width, m.
y	gaseous concentration, mol/m ³ .
Z	depth, m.

Greek letters

α	entrainment coefficient [].
λ	spreading coefficient [].
ρ	density, kg/m ³ .

Subscripts

3,2	Sauter-mean.
G	Gaussian profile.
O	oxygen.
N	nitrogen.
T	top-hat profile.
a	ambient water.
b	bubble.
i	gas species, oxygen or nitrogen.
o	initial.
p	plume water and gas mixture.
w	plume water.

[34] Acknowledgments. The authors thank Daniel McGinnis for his valuable technical assistance. Financial support was generously provided by the U.S. National Science Foundation (grant BES 0202034) and the Western Virginia Water Authority.

References

- Asaeda, T., and J. Imberger (1993), Structure of bubble plumes in linearly stratified environments, *J. Fluid Mech.*, **249**, 35–57.
- Brevik, I. (1977), Two-dimensional air-bubble plume, *J. Waterw. Port Coastal Ocean Div. Am. Soc. Civ. Eng.*, **103**, 101–115.
- Brevik, I., and R. Kluge (1999), On the role of turbulence in the phenomenological theory of plane and axisymmetric air-bubble plumes, *Int. J. Multiphase Flow*, **25**, 87–108.
- Burris, V. L., D. F. McGinnis, and J. C. Little (2002), Predicting oxygen transfer and water flow rate in airlift aerators, *Water Res.*, **36**, 4605–4615.
- Cole, T. M., and S. A. Wells (2003), CE-QUAL-W2: A two-dimensional, laterally averaged, hydrodynamic and water quality model, Version 3.2, U.S. Army Eng. and Res. Dev. Cen., Vicksburg, Miss.
- Cooke, G. D., and R. E. Carlson (1989), *Reservoir Management for Water Quality and THM Precursor Control*, 387 pp., Am. Water Works Assoc. Res. Found., Denver, Colo.
- Ditmars, J. D., and K. Cederwall (1974), Analysis of air-bubble plumes, paper presented at the 14th Coastal Engineering Conference, Am. Soc. of Civ. Eng., Copenhagen, 24–28 June.
- Fannlop, T. K., and K. Sjøen (1980), Hydrodynamics of underwater blow-outs, *Norw. Marit. Res.*, **4**, 17–33.
- Fannlop, T. K., and D. M. Webber (2003), On buoyant plumes rising from area sources in a calm environment, *J. Fluid Mech.*, **497**, 319–344.
- Fannlop, T. K., S. Hirschberg, and J. Kueffer (1991), Surface current and recirculating cells generated by bubble curtains and jets, *J. Fluid Mech.*, **229**, 629–657.
- Fischer, H. B., E. J. List, R. C. Y. Koh, J. Imberger, and N. H. Brooks (1979), *Mixing in Inland and Coastal Waters*, 483 pp., Elsevier, New York.
- Johansen, O. (2000), DeepBlow—A Lagrangian plume model for deep water blowouts, *Spill Sci. Technol. Bull.*, **6**, 103–111.
- Kobus, H. E. (1968), Analysis of the flow induced by air-bubble systems, paper presented at the 11th Coastal Engineering Conference, Am. Soc. of Civ. Eng., London.

- Laureshen, C. J., and R. D. Rowe (1987), Modeling of plane bubble plumes, paper presented at the 24th National Heat Transfer Conference and Exhibition, Am. Soc. of Mech. Eng., Pittsburgh, Pa., 9–12 Aug.
- Lemckert, C. J., and J. Imberger (1993), Energetic bubble plumes in arbitrary stratification, *J. Hydraul. Eng.*, **119**, 680–703.
- McDougall, T. J. (1978), Bubble plumes in stratified environments, *J. Fluid Mech.*, **85**, 655–672.
- McGinnis, D. F., and J. C. Little (1998), Bubble dynamics and oxygen transfer in a Speece cone, *Water Sci. Technol.*, **37**, 285–292.
- McGinnis, D. F., and J. C. Little (2002), Predicting diffused-bubble oxygen transfer rate using the discrete-bubble model, *Water Res.*, **36**, 4627–4635.
- McGinnis, D. F., J. C. Little, and A. Wuest (2001), Hypolimnetic oxygenation: Coupling bubble-plume and reservoir models, paper presented at Asian Waterqual 2001: First IWA Asia-Pacific Regional Conference, Int. Water Assoc., Fukuoka, Japan, 12–15 Sept.
- McGinnis, D. F., A. Lorke, A. Wüest, A. Stöckli, and J. C. Little (2004), Interaction between a bubble plume and the near field in a stratified lake, *Water Resour. Res.*, **40**, W10206, doi:10.1029/2004WR003038.
- Milgram, J. H. (1983), Mean flow in round bubble plumes, *J. Fluid Mech.*, **133**, 345–376.
- Peterson, M. J., G. F. Cada, M. J. Sale, and G. K. Eddlemon (2003), Regulatory approaches for addressing dissolved oxygen concerns at hydropower facilities, 38 pp., U.S. Dep. of Energy Off. of Energy Efficiency and Renewable Energy, Idaho Falls, Idaho.
- Rayyan, F., and R. E. Speece (1977), Hydrodynamics of bubble plumes and oxygen absorption in stratified impoundments, *Prog. Water Technol.*, **9**, 129–142.
- Sahoo, G. B., and D. Luketina (2003), Modeling of bubble plume design and oxygen transfer for reservoir restoration, *Water Res.*, **37**, 393–401.
- Schladow, S. G. (1992), Bubble plume dynamics in a stratified medium and the implications for water quality amelioration in lakes, *Water Resour. Res.*, **28**, 313–321.
- Shang, E. H. H., R. M. K. Yu, and R. S. S. Wu (2006), Hypoxia affects sex differentiation and development, leading to a male-dominated population in zebrafish (*Danio rerio*), *Environ. Sci. Technol.*, **40**, 3118–3122.
- Singleton, V. L., and J. C. Little (2005), Linear bubble plume model for hypolimnetic oxygenation: Full-scale evaluation and sensitivity analysis, paper presented at 9th Workshop on Physical Processes in Natural Waters, Lancaster Univ., Lancaster, UK, 4–6 Sept.
- Singleton, V. L., and J. C. Little (2006), Designing hypolimnetic aeration and oxygenation systems: A review, *Environ. Sci. Technol.*, **40**(24), 7512–7520, doi:10.1021/es060069s.
- Wilkinson, D. L. (1979), Two-dimensional bubble plumes, *J. Hydraul. Div. Am. Soc. Civ. Eng.*, **105**, 139–154.
- Wüest, A., N. H. Brooks, and D. M. Imboden (1992), Bubble plume modeling for lake restoration, *Water Resour. Res.*, **28**, 3235–3250.
- Zheng, L., P. D. Yapa, and F. Chen (2002), A model for simulating deep-water oil and gas blowouts: I. Theory and model formulation, *J. Hydraul. Res.*, **41**, 339–351.

P. Gantzer, J. C. Little, and V. L. Singleton, Department of Civil and Environmental Engineering, Virginia Polytechnic Institute and State University, 418 Durham Hall, Blacksburg, VA 24061-0246, USA.
(jcl@vt.edu)

Exhibit E

CARBON DIOXIDE IN WATER AND SEAWATER: THE SOLUBILITY OF A NON-IDEAL GAS

R.F. WEISS

Scripps Institution of Oceanography, University of California at San Diego, La Jolla,
Calif. 92037 (U.S.A.)

(Received May 29, 1974; revised and accepted August 22, 1974)

ABSTRACT

Weiss, R.F., 1974. Carbon dioxide in water and seawater: the solubility of a non-ideal gas.
Mar. Chem., 2: 203-215.

New measurements of the solubility of carbon dioxide in water and seawater confirm the accuracy of the measurements of Murray and Riley, as opposed to those of Li and Tsui. Corrections for non-ideal behavior in the gas phase and for dissociation in distilled water are required to calculate solubility coefficients from these sets of data. Equations for the solubilities of real gases are presented and discussed. Solubility coefficients for carbon dioxide in water and seawater are calculated for the data of Murray and Riley, and are fitted to equations in temperature and salinity of the form used previously to fit the solubilities of other gases.

INTRODUCTION

Until very recently, direct determinations of the solubility of CO₂ in seawater have been limited to a few measurements of Krogh (1904). Most authors have preferred to use approximations based on the solubility of CO₂ in aqueous sodium chloride solutions. Buch et al. (1932) prepared tables of seawater CO₂ solubilities from the Bohr (1899) data for sodium chloride solutions, using the assumption that the effect of sea salt on the solubility is equal to the effect of an equal weight of sodium chloride. Lyman (1957) refined this assumption by considering the salting-out of the various constituents of sea salt, suggesting that the Buch et al. values may be about 0.5% too high.

The lack of direct measurements of CO₂ solubility in seawater has recently been alleviated by two independent sets of data: those of Li and Tsui (1971), determined by infrared analysis, and those of Murray and Riley (1971), determined gravimetrically. Unfortunately, the agreement between these sets of measurements is poor. Whereas the data of Li and Tsui support the values assumed by Buch et al., the solubility data of Murray and Riley are as much as 3.8% lower than those of Li and Tsui at higher temperatures and salinities. The agreement is better at lower temperatures and in distilled water, so that

the differences cannot be expressed either as a constant offset or as a constant factor.

In hopes of resolving these discrepancies, it was decided to make several independent measurements of CO₂ solubility. If it could be shown that a few accurate measurements covering a wide range of temperature and salinity were consistently in close agreement with one of the two sets of data, this would provide strong support for the accuracy of that set at all measured temperatures and salinities.

The second objective of this work was the fitting of the best CO₂ solubility data to an equation in temperature and salinity of the form used previously to fit the solubilities of N₂, O₂, and Ar (Weiss, 1970), He and Ne (Weiss, 1971a), H₂ (Crozier and Yamamoto, 1974), and Kr (Weiss and Kyser, in preparation). CO₂ is many times more soluble than any of the gases treated previously, and in the gas phase its departures from the ideal gas approximation are large compared to the accuracy with which its solubility can be measured. Therefore, before the use of such equations is justified, it is necessary to use Henry's law for real gases and to test its validity over a range of partial pressures of CO₂. Also, it is necessary to test the validity of the logarithmic Setchénov salting-out relation (Weiss, 1970, 1971b) for CO₂ in seawater.

Both Li and Tsui (1971), and Murray and Riley (1971), noted that their measurements would be affected by the dissociation of dissolved hydrated CO₂ to form bicarbonate, and accordingly they acidified their seawater samples to a sufficiently low pH so that this effect could be neglected. However, both studies failed to take this effect into account for their distilled-water measurements, which were made without acidification. Although this effect cancels in direct comparisons between the two sets of measurements, the proper use of Henry's law and of the Setchénov relation requires that the data be corrected for dissociation.

All distilled water CO₂ solubility data discussed in the following sections have been corrected for dissociation using the following approximation:

$$[\text{CO}_2] = [\Sigma \text{CO}_2] - \sqrt{K_1' [\Sigma \text{CO}_2]} \quad (1)$$

where [CO₂] is the sum of the concentrations of dissolved CO₂ and undisassociated hydrated CO₂, [ΣCO₂] is the sum of the concentrations of all dissolved CO₂ species as measured in the solubility experiment, and K_{1'} is the first apparent dissociation constant at the temperature of the measurement.*¹ Solubilities measured in distilled water for p_{CO₂} ≈ 1 atm are thus reduced by ~ 0.18% at 0°C, to ~ 0.46% at 40°C.

HENRY'S LAW AND REAL GASES

King (1969, ch.4) presents an excellent and thorough discussion of Henry's law and its application to real gases over a wide range of pressures. By ex-

*¹ Values of K_{1'} were calculated according to Harned and Davis (1943, eq.15):
 $\log_{10} K_1' = -3404.71/T + 14.8435 - 0.032786 T$.

pressing the activity of the solute in the gas phase by its fugacity, and by making the appropriate thermodynamic correction for the expansion of the solution by the dissolved gas, the "modified Henry's law equation" is obtained:

$$f_i = Q_i x_i \exp(P\bar{v}_i/RT) \quad (2)$$

where f_i is the fugacity of gas i , x_i is the mole fraction of i in solution, \bar{v}_i is the partial molal volume of i in solution, R is the gas constant, T is the absolute temperature, P is the total pressure at the liquid-gas interface, and Q_i , the modified Henry's law constant for i , is a function only of the temperature and the nature of the solvent.

Conveniently, King uses the CO₂-water system as an example to illustrate the application of eq. 2. Using literature data, with special emphasis on the work of Wiebe and Gaddy (1939; 1940), King (1969, pp.219-220) demonstrates that eq. 2 holds over the entire CO₂-pressure range from zero to several hundred atmospheres, at a number of different temperatures.*² The use of the modified form of Henry's law to calculate CO₂ solubilities over wide ranges of total pressures and CO₂ partial pressures, based on accurate solubility measurements made at pressures near 1 atm, is therefore well justified.*³ This is particularly germane to studies dealing with the solubility of natural levels of atmospheric CO₂.

In treating the solution of atmospheric gases in natural waters, it is convenient to express the solubility in terms of the Bunsen coefficient β , thereby avoiding the problem of evaluating the mole fraction of the gas in mixed solvents such as seawater. The Bunsen coefficient is defined here as the volume of gas (STP) absorbed per unit volume of the *solution*, at the temperature of the measurement, when the total pressure and the fugacity are both 1 atm.*⁴ This is preferable to the usual definition of β for ideal gases, in which the *partial* pressure is set at 1 atm and the *total* pressure is not specified, because the total pressure is required to define the system (see eq. 2). Thus, C_i , the volume (STP) of gas i dissolved in a unit volume of *solution* at the temperature of the measurement, is given by the relation:

$$C_i = \beta_i f_i \exp[(1 - P)\bar{v}_i/RT] \quad (3)$$

where:

$$\beta_i = Q_i^{-1} V_i^\dagger \rho N \exp(-\bar{v}_i/RT) \quad (4)$$

and V_i^\dagger is the volume of one mole of the real gas i at STP, ρ is the density of the *solution*, N is the number of moles in a unit weight of *solvent*, and P is in atmospheres. Since the solubility of most gases ($\bar{v} \approx 30 \text{ cm}^3/\text{mole}$) is decreased

*² Note that helium solubility measurements by these workers are in excellent agreement with recent microgasometric data (Weiss, 1971a).

*³ A more detailed discussion of CO₂ solubility as a function of pressure is given in the Appendix.

*⁴ Pressures are given here in atmospheres because of the widespread use of this unit to define standard states. Atmospheres may be converted to bars (10⁵ newtons/m²), the more fundamental unit commonly used in high-pressure work, by multiplying by 0.986923.

by only $\sim 0.15\%$ per atmosphere increase in total pressure, the small deviations from 1 atm total pressure which are encountered in many natural conditions may be neglected, thereby reducing the exponential term in eq.3 to unity.

In the special case of CO₂, solubilities are generally used in calculations of chemical equilibria and are therefore best given in molar (moles/l. of solution) or gravimetric (moles/kg of solution) units:

$$[\text{CO}_2] = K_0 f_{\text{CO}_2} \exp[(1 - P)\bar{v}_{\text{CO}_2}/RT] \quad (5)$$

where the constant K_0 equals β/V^\dagger in molar units (moles/l. atm) or $\beta/\rho V^\dagger$ in gravimetric units (moles/kg · atm). Again, the exponential term may be taken as unity at total pressures near 1 atm.

In the following discussions, gas volumes and fugacity-pressure corrections are based on the virial equation of state. The appropriate expansions are carried only as far as the second virial coefficient $B(T)$, since the terms containing the third virial coefficient were always found to be negligible ($\sim 10^{-5}$). Values of $B(T)$ in cm³/mole, for CO₂ (Sengers et al., 1971) in the range 265–320°K, are well represented by a power series:

$$B(T) = -1636.75 + 12.0408 T - 3.27957 \cdot 10^{-2} T^2 + 3.16528 \cdot 10^{-5} T^3 \quad (6)$$

Thus, for the pure gas (neglecting the small contribution of water vapor), the solubility measurements discussed in the following sections have been corrected using the approximations (Guggenheim, 1967, pp.91 and 97):

$$V(P, T) = V^*(P, T) + B(T) \quad (7)$$

and:

$$\ln(f/P) = B(T) P/RT \quad (8)$$

where V is the volume of one mole of the real gas, and V^* is the volume of one mole of ideal gas.

In most natural applications which do not require accuracies greater than $\sim 0.7\%$, the fugacity in eq.4 may be taken as equal to the partial pressure. However, if greater accuracy is desired, the fugacity must be calculated. For a nearly pure gas phase, eq.8 will suffice, but for multi-component gas phases, such as CO₂ in air, it is necessary to calculate fugacity in the mixture.

Useful equations for the calculation of fugacities in binary mixtures are given by Guggenheim (1967, pp.175–177):

$$f_1 = x_1 P \exp[(B_{11} + 2x_2^2 \delta_{12}) P/RT] \quad (9)$$

where the subscripts 1 and 2 refer to the two components of the mixture, x is the mole fraction, and B_{11} is the second virial coefficient of the pure gas 1.

The quantity δ_{12} is defined by:

$$\delta_{12} = \frac{1}{2} (B_{11} + B_{22}) + \delta_{12} \quad (10)$$

where B_{12} is the cross virial coefficient for interactions between gas 1 and gas 2 molecules, and B_{11} and B_{22} refer to the pure gases 1 and 2, respectively. In addition to the binary mixtures, equations 8 and 9 may also be applied to mixtures of CO_2 in air when $x_{\text{CO}_2} \ll 1$.

Few direct measurements of cross-virial coefficients exist, so that the quantity δ_{12} must be evaluated from theoretical considerations. The quantity $\delta_{\text{CO}_2-\text{air}}$ has been evaluated from the Lennard-Jones (6-12) potential model following the method of Hirschfelder, Curtiss and Bird (1954, pp.166-170). The results in cm^3/mole for the temperature range 273 to 313°K are well represented by the linear relation:

$$\delta_{\text{CO}_2-\text{air}} = 57.7 - 0.118 T \quad (11)$$

The magnitude of this correction, as opposed to assuming $\delta = 0$ (Lewis and Randall rule), is about 0.2% in the overall solubility calculation, or about one third of the total deviation from ideal gas behavior.

Calculations of CO_2 fugacity using the virial equation of state are valid to within 0.1% for total pressures up to ~ 10 atm. Higher pressures require the use of more sophisticated equations of state, such as the Benedict, Webb and Rubin (1940; 1942) equation, which may be used to at least 500 atm (see Appendix).

DATA FITTING

The corrected data of Murray and Riley (1971) were fitted to the same equation in temperature and salinity which has been used to fit the solubilities of many other gases (see Introduction). This equation is derived from the integrated van't Hoff equation and the logarithmic Setchénov salinity dependence, and has the form (Weiss, 1970):

$$\ln K_0 = A_1 + A_2(100/T) + A_3 \ln(T/100) + S\% [B_1 + B_2(T/100) + B_3(T/100)^2] \quad (12)$$

where K_0 may be expressed either in moles/l · atm, referring to a liter of solution at the temperature of the measurement and an atmosphere fugacity in the gas phase, or in moles/kg · atm, referring to a kilogram of solution. The A 's and B 's are constants, T is the absolute temperature, and $S\%$ is the salinity in parts per thousand. The method of fitting the data, and the conditions for justification of the Setchénov equation and the number of terms used in the expansion, are discussed elsewhere (Weiss, 1970).

The corrected Murray and Riley CO_2 data showed good agreement with the equations at all stages of the fitting procedure. The data show a root-mean-square deviation from the final fitted equation of $1.4 \cdot 10^{-4}$ moles/l · atm in K_0 , or about 0.3%. Agreement with the Setchénov relation is shown in Fig. 1 by the random nature of the deviations as a function of salinity for each measured isotherm. The fitted values of the constants in eq. 12 are listed in Table I for K_0 in molar and in gravimetric units. Values of K_0 at various temperatures

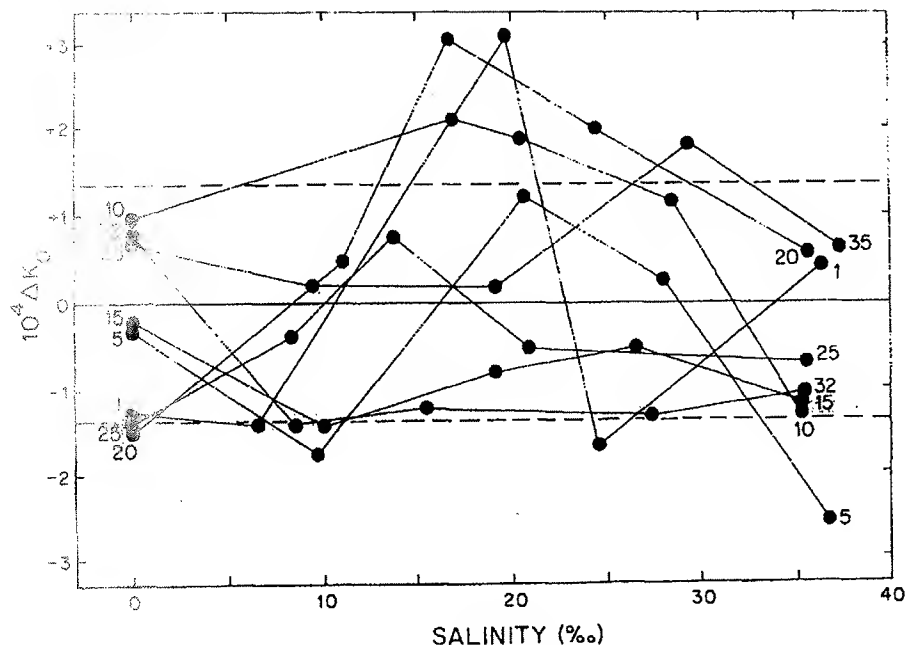


Fig. 1. Deviations of the Murray and Riley (1971) CO_2 solubility data (corrected for dissociation and non-ideality) in moles/l · atm from the fitted curve (eq. 12), plotted against salinity. Measurements made at constant temperature are connected by lines, and are labeled to the nearest $^{\circ}\text{C}$. The dashed lines show ± 1 standard deviation.

and salinities calculated from these constants are listed in Tables II and III.

Salting-out constants (the B 's in eq. 12) were also determined for the solubility of CO_2 in aqueous NaCl solutions using the data of Bohr (1899), corrected for dissociation. With NaCl concentration expressed as weight percent in solu-

TABLE I

Constants for the calculation of the solubility of CO_2 in molar and gravimetric units according to eq. 12

Units of K_0		
	moles/l · atm	moles/kg · atm
A_1	-58.0931	-60.2409
A_2	90.5069	93.4517
A_3	22.2940	23.3585
B_1	0.027766	0.023617
B_2	-0.025888	-0.023656
B_3	0.0050578	0.0047036

TABLE II

The solubility coefficient K_o (10^{-2} moles/l · atm)

T (°C)	Salinity (%)								
	0	10	20	30	34	35	36	38	40
-1	—	—	7.273	6.903	6.760	6.724	6.689	6.620	6.551
0	7.758	7.364	6.990	6.635	6.498	6.465	6.431	6.364	6.298
1	7.458	7.081	6.723	6.382	6.251	6.219	6.187	6.123	6.060
2	7.174	6.813	6.469	6.143	6.017	5.986	5.955	5.894	5.833
3	6.905	6.558	6.229	5.916	5.795	5.766	5.736	5.677	5.619
4	6.650	6.317	6.001	5.701	5.585	5.557	5.528	5.472	5.416
5	6.408	6.088	5.785	5.497	5.386	5.358	5.331	5.277	5.223
6	6.178	5.871	5.580	5.303	5.196	5.170	5.144	5.092	5.040
8	5.751	5.469	5.200	4.945	4.846	4.822	4.797	4.749	4.702
10	5.366	5.105	4.857	4.621	4.529	4.507	4.485	4.440	4.396
12	5.017	4.776	4.546	4.327	4.243	4.222	4.201	4.160	4.119
14	4.700	4.477	4.264	4.062	3.983	3.964	3.945	3.906	3.869
16	4.412	4.205	4.008	3.820	3.747	3.729	3.712	3.676	3.641
18	4.149	3.958	3.775	3.600	3.533	3.516	3.499	3.466	3.434
20	3.910	3.732	3.562	3.400	3.337	3.322	3.306	3.275	3.245
22	3.691	3.526	3.368	3.217	3.158	3.144	3.130	3.101	3.073
24	3.491	3.337	3.190	3.050	2.995	2.982	2.968	2.942	2.915
26	3.307	3.164	3.027	2.897	2.846	2.833	2.821	2.796	2.771
28	3.138	3.005	2.878	2.756	2.709	2.697	2.685	2.662	2.639
30	2.983	2.859	2.741	2.627	2.583	2.572	2.561	2.540	2.518
32	2.840	2.725	2.615	2.509	2.468	2.457	2.447	2.427	2.407
34	2.708	2.601	2.498	2.400	2.361	2.352	2.342	2.323	2.305
36	2.587	2.487	2.391	2.299	2.263	2.254	2.246	2.228	2.211
38	2.474	2.382	2.292	2.207	2.173	2.165	2.157	2.140	2.124
40	2.370	2.284	2.201	2.121	2.090	2.082	2.074	2.059	2.044

tion, and K_o in moles/l · atm, the constants are: $B_1 = -0.68330$, $B_2 = 0.40911$, $B_3 = -0.064989$. Averaged over the temperature range 0–40°C, K_o is 0.8% higher in a 3.6% NaCl solution than K_o in seawater of 36‰ salinity, calculated from the salting-out constants in Table I. This difference probably lies within the error of the Lyman (1957) prediction that K_o in the NaCl solution would be 0.5% higher.

EXPERIMENTAL METHOD

Measurements of CO₂ solubility were carried out by the microgasometric technique used previously to measure He and Ne solubilities (Weiss, 1971a). High-purity CO₂ (certified ≥ 99.99%) was supplied by Matheson Gas Products and gas chromatographic analysis showed < 0.01% air contamination. Because of the high solubility of CO₂ compared to He and Ne, the amount of degassed

water added to the equilibration chamber was reduced to about one third of the total gas volume. Under these conditions, equilibration was extremely rapid (first-order rate constant $\tau \approx 30$ sec) so that the 6–10 minutes allowed for equilibration were more than adequate. Permeation of CO₂ through the indicator drop was rapid, and required that the chamber above the drop be filled with pure CO₂ prior to each equilibration. With this procedure, no drift in the indicator drop could be detected over a period of 1 h.

In order to obtain the most direct comparisons with the work of Murray and Riley and of Li and Tsui, chemical procedures similar to their's were followed. Distilled water measurements were performed without acidification and the corrections for dissociation were made. Surface seawater, collected at La Jolla and evaporated to increase its salinity by ~2‰, was passed through a 0.45μ filter, poisoned with 1 mg/liter HgCl₂, and its salinity determined to ± 0.004‰ by an inductive salinometer. Sulfuric acid (~2N) was then added to bring the pH to 2.2 and the salinity was adjusted by gravimetric determination of the amount of H₂O added in the acid solution. Following Murray and

TABLE III

The solubility coefficient K_s (10⁻² moles/kg·atm)

T (°C)	Salinity (‰)								
	0	10	20	30	34	35	36	38	40
-1	—	—	7.158	6.739	6.579	6.539	6.500	6.422	6.345
0	7.758	7.305	6.880	6.479	6.325	6.287	6.249	6.175	6.101
1	7.458	7.024	6.616	6.232	6.085	6.048	6.012	5.941	5.870
2	7.174	6.758	6.367	5.999	5.857	5.822	5.788	5.719	5.651
3	6.904	6.506	6.131	5.777	5.642	5.608	5.575	5.509	5.444
4	6.649	6.267	5.907	5.568	5.438	5.405	5.374	5.310	5.248
5	6.407	6.040	5.695	5.369	5.244	5.213	5.182	5.122	5.062
6	6.177	5.825	5.493	5.180	5.060	5.031	5.001	4.943	4.885
8	5.752	5.427	5.120	4.831	4.720	4.693	4.666	4.612	4.558
10	5.367	5.067	4.784	4.516	4.413	4.388	4.363	4.313	4.263
12	5.019	4.741	4.479	4.231	4.136	4.112	4.089	4.042	3.997
14	4.703	4.446	4.202	3.972	3.884	3.862	3.840	3.797	3.755
16	4.416	4.177	3.951	3.738	3.655	3.635	3.615	3.575	3.536
18	4.155	3.933	3.723	3.524	3.448	3.429	3.410	3.373	3.336
20	3.916	3.710	3.515	3.330	3.258	3.241	3.223	3.189	3.154
22	3.699	3.507	3.325	3.152	3.086	3.069	3.053	3.021	2.989
24	3.499	3.321	3.151	2.990	2.928	2.912	2.897	2.867	2.837
26	3.317	3.150	2.992	2.841	2.783	2.769	2.755	2.727	2.699
28	3.149	2.994	2.846	2.705	2.651	2.638	2.624	2.598	2.572
30	2.995	2.850	2.712	2.580	2.530	2.517	2.505	2.480	2.455
32	2.854	2.718	2.589	2.466	2.418	2.406	2.395	2.372	2.349
34	2.723	2.596	2.476	2.360	2.316	2.305	2.294	2.272	2.250
36	2.603	2.484	2.371	2.263	2.221	2.211	2.201	2.180	2.160
38	2.492	2.381	2.275	2.174	2.134	2.125	2.115	2.096	2.077
40	2.389	2.285	2.186	2.091	2.054	2.045	2.036	2.018	2.000

Riley (1971), the effect of the added H_2SO_4 molecules on the salinity was neglected as being insignificant with respect to altering the solubility of CO_2 . The water was degassed using the same vacuum extraction method as in the previous work (Weiss, 1971a).

The results were calculated in the same manner as previous microgasometric measurements, except that the corrections for non-ideal behavior discussed in the foregoing section were applied. The correction for the expansion of the aqueous phase during equilibration was made using a partial molal volume of 32.3 cm^3 per mole of CO_2 (see Appendix). The overall accuracy of these CO_2 solubility measurements is estimated as $\pm 0.2\%$.

RESULTS AND CONCLUSIONS

The microgasometric experimental values for K_o in moles/l·atm at several temperatures and salinities, corrected for dissociation and non-ideality, are given in Table IV. Deviations of the microgasometric results from the fitted Murray and Riley data, plotted in Fig.2, show excellent agreement without systematic deviations. At each of the three different temperature and salinity conditions, the range of microgasometric points brackets the fitted curve. The average deviation of all the measured points is $1.5 \cdot 10^{-5}$ moles/l·atm, and the root-mean-square deviation is $1.2 \cdot 10^{-4}$ moles/l·atm. Curves for the deviations of the data of Li and Tsui, taken from their equations (1) and (2a) after correction for dissociation and non-ideality, are also plotted in Fig.2. Although their fresh-water measurements are in reasonably good agreement, the seawater data of Li and Tsui show large deviations from the fitted Murray and Riley

TABLE IV

Experimental CO_2 solubilities: microgasometric determinations of K_o in moles/l·atm

Salinity (%)	t ($^{\circ}\text{C}$)	$K_o \cdot 10^2$
0.0	20.61	3.848
0.0	20.63	3.843
0.0	20.60	3.867
0.0	20.59	3.834
0.0	20.61	3.840
35.330	6.59	5.071
35.330	6.60	5.063
35.330	6.60	5.068
35.330	6.59	5.041
35.330	20.62	3.245
35.330	20.63	3.272
35.330	20.63	3.245
35.330	20.63	3.255
35.330	20.63	3.254
35.330	20.63	3.252

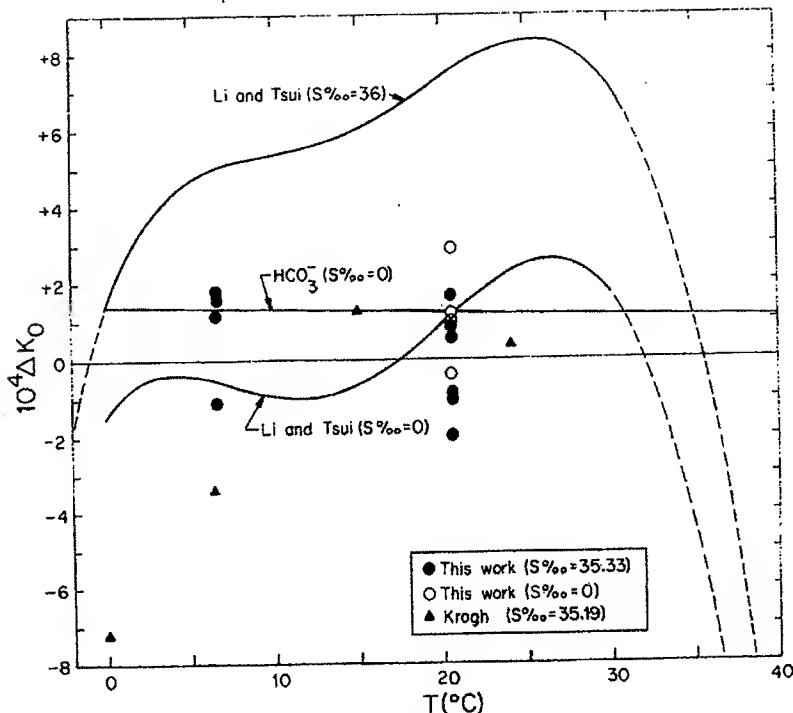


Fig. 2. Deviations of various CO_2 distilled water and seawater solubility data in moles/l. atm from the fit to the corrected data (see text) of Murray and Riley (1971), plotted against temperature. The curves for Li and Tsui (1971) are taken from their equations (1) and (2a), and, like the data of Krogh (1904), have been corrected for non-ideality and dissociation: the dashed portions of these curves represent the extrapolation of their equations beyond the range of their measurements. The magnitude of the error caused by dissociation for measurements made in distilled water at $\text{pCO}_2 = 1 \text{ atm}$ is shown by the line labeled " HCO_3^- ".

data. Fig. 2 also shows the corrected data of Krogh (1904), which agree well with Murray and Riley at the higher temperatures.

The microgasometric results provide independent confirmation of the accuracy of the CO_2 solubility measurements of Murray and Riley (1971) and show the measurements of Li and Tsui (1971) to be in error by as much as $\sim 4\%$ at the higher temperatures and salinities. The data of Murray and Riley, corrected for the effects of non-ideal gas behavior and for dissociation in the distilled water measurements, are well represented by the Setchénov and integrated van't Hoff equations used previously to fit the solubilities of several other comparatively ideal gases. Thus, CO_2 solubilities calculated from eq. 12, using the constants in Table I, are believed to provide the most accurate values in the literature, with an overall accuracy estimated at $\pm 1 \cdot 10^{-4}$ moles/l. atm or about 0.2%. The solubility of CO_2 obeys the modified form of Henry's law

(eq.2) and it is therefore necessary to take account of the total pressure, as well as to calculate the fugacity of CO₂ in the gas phase, if full use is to be made of the accuracy of these solubility data.

ACKNOWLEDGEMENTS

I thank T.K. Kyser for his assistance with the laboratory measurements, and H. Craig and S.L. Miller for valuable discussions on the thermodynamics of real gases. This research was supported by a U.S. National Science Foundation grant to the Isotope Laboratory, Scripps Institution of Oceanography.

APPENDIX

Carbon dioxide solubility at high pressures

At pressures greater than ~10 atm, CO₂ fugacities calculated from the virial equation of state, even when carried to the third virial coefficient, show large deviations from the literature values (Deming and Deming, 1939). Far better results are obtained with the Benedict, Webb and Rubin equation of state for pure substances (Benedict et al., 1940) and for mixtures (Benedict et al., 1942), which fit the observed *p*-*V*-*T* data up to densities of twice the critical density. In the following discussion, Benedict, Webb and Rubin equation constants for pure CO₂ are taken from the Bishnoi and Robinson (1971)*⁵ volume-dependent fit to the compressibility data of Reamer et al. (1944). Because the Benedict, Webb and Rubin equation is an explicit function of *V* and *T*, the solution for specific values of *P* is obtained by the method of successive approximations.

Fig.3 shows the distilled water CO₂ solubility data of Wiebe and Gaddy (1940) for the temperature range 12–40°C and the pressure range 25–500 atm, plotted as ln(*f*/*x*) against the total pressure *P*. Fugacities were calculated assuming a pure CO₂ phase at a pressure of *P* minus the vapor pressure of water. Negligible error was introduced by this approximation because of the small fraction of water vapor in the CO₂-rich phase. The straight lines plotted at each of the six experimental temperatures were fitted to the Wiebe and Gaddy data by the method of least-squares.

According to eq.2, if \bar{v} is independent of *P*, then ln(*f*/*x*) plotted as a function of *P* at constant *T* should give a straight line with intercept ln *Q* and slope (\bar{v}/RT) . This relationship is strongly supported by the experimental data as shown in Fig.3. The root-mean-square deviation of the Wiebe and Gaddy measurements about the six straight lines is ~0.8%, and there is no systematic indication of departure from linearity. The slopes of these lines correspond to remarkably constant values of \bar{v} , with a mean of 32.3 cm³/mole and a standard deviation of 0.5 cm³/mole. Thus, the data show no significant variation in \bar{v} , either as a function of *T* over the range 12–40°C, or as a function of *P* up to 500 atm.

Results of the fit to the corrected Murray and Riley distilled water data (eq.12), measured at 1 atm, are also plotted in Fig.3. The overall agreement with the Wiebe and Gaddy data is good, although there may be a systematic difference at 12°C (the Wiebe and Gaddy data also show the greatest scatter at this temperature). On the average, the solubilities at 1 atm obtained from the linear fits to the Wiebe and Gaddy data are 0.4% lower in β (or higher in *Q*), and show a 2% root-mean-square difference.

*⁵ The constants, converted from English to metric units (atm, l, mole, °K): $A_0 = 1.9521940$, $B_0 = 0.033065171$, $C_0 = 170449.55$, $a = 0.25264437$, $b = 6.6041298 \cdot 10^{-3}$, $c = 19592.012$, $\alpha = 4.7117009 \cdot 10^{-5}$, $\gamma = 4.3414415 \cdot 10^{-3}$, $R = 0.08205601$.

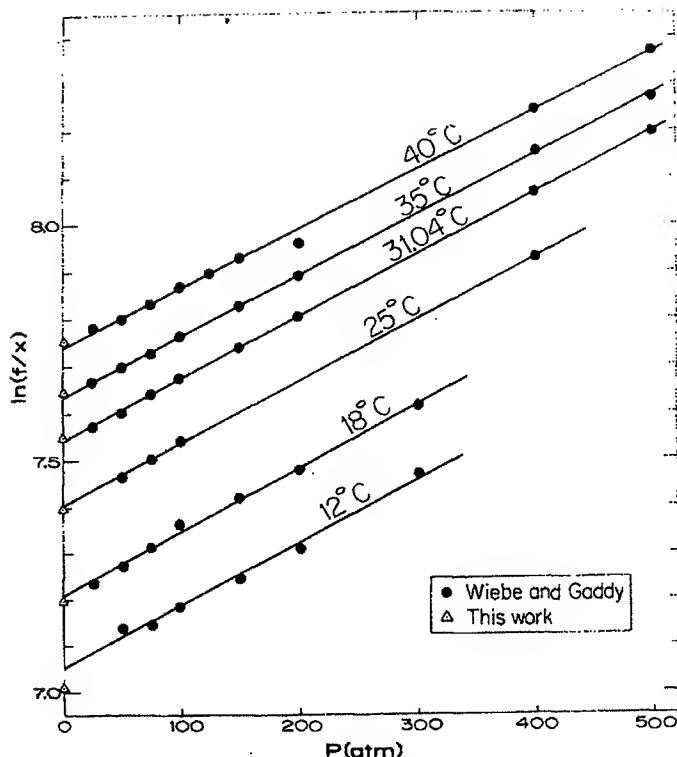


Fig. 3. High-pressure distilled water CO_2 solubility data of Wiebe and Gaddy (1940) plotted as the logarithm of the fugacity to mole fraction ratio, against the total pressure. Solubilities at 1 atm calculated from eq. 12 are plotted for the temperatures of the Wiebe and Gaddy measurements.

In summary, the high-pressure solubility data show that the modified form of Henry's law (eqs. 2, 3, or 5) is valid for CO_2 in water over the entire pressure range of 0–500 atm, which corresponds to a dissolved CO_2 concentration range of 0–1.7 molar. Assuming that \bar{v} for CO_2 is the same in seawater as in distilled water, as was shown by Enns et al. (1965) for O_2 , the solubility of CO_2 in seawater at high pressures may also be calculated from these equations.

REFERENCES

- Benedict, M., Webb, G.B. and Rubin, L.C., 1940. An empirical equation for the thermodynamic properties of light hydrocarbons and their mixtures. I. Methane, ethane, propane and *n*-butane. *J. Chem. Phys.*, 8: 334–345
- Benedict, M., Webb, G.B. and Rubin, L.C., 1942. An empirical equation for the thermodynamic properties of light hydrocarbons and their mixtures. II. Mixtures of methane, ethane, propane and *n*-butane. *J. Chem. Phys.*, 10: 747–758
- Bishnoi, P.R. and Robinson, D.B., 1971. An evaluation of methods for determining the parameters in the BWR equation of state using volumetric and heat capacity data. *Can. J. Chem. Eng.*, 49: 642–650

- Bohr, C., 1899. Definition und Methode zur Bestimmung der Invasions- und Evasions-coeffizienten bei der Auflösung von Gasen in Flüssigkeiten. Werthe der genannten Constanten sowie der Absorptionscoeffizienten der Kohlensäure bei Auflösung in Wasser und in Chlornatriumlösungen. Ann. Phys. Chem., 68: 500—525
- Buch, K., Harvey, H.W., Wattenberg, H. and Gripenberg, S., 1932. Über das Kohlensäure-system in Meerwasser. Rapp. Cons. Explor. Mer, 79: 1—70
- Crozier, T.E. and Yamamoto, S., 1974. The solubility of hydrogen in water, seawater and NaCl solutions. J. Chem. Eng. Data, 19: 242—244
- Deming, W.E. and Deming, L.S., 1939. Some physical properties of compressed gases. VI. The fugacity of carbon dioxide. Phys. Rev., 56: 108—112
- Enns, T., Scholander, P.F. and Bradstreet, E.D., 1965. The effect of hydrostatic pressure on gases dissolved in water. J. Phys. Chem., 69: 389—391
- Guggenheim, E.A., 1967. Thermodynamics. North-Holland, Amsterdam, 5th ed., 390 pp.
- Harned, H.S. and Davis, R., 1943. The ionization constant of carbonic acid in water and the solubility of carbon dioxide in aqueous salt solution from 0-50°. J. Am. Chem. Soc., 65: 2030—2037
- Hirschfelder, J.O., Curtiss, C.F. and Bird, R.B., 1954. Molecular Theory of Gases and Liquids. Wiley, New York, N.Y., 1219 pp.
- King, M.B., 1969. Phase Equilibrium in Mixtures. Pergamon, Oxford, 584 pp.
- Krogh, A., 1904. On the tension of carbonic acid in natural waters and especially in the sea. Medd. om Grönland, 26: 331—405
- Li, Y.H. and Tsui, T.F., 1971. The solubility of CO₂ in water and seawater. J. Geophys. Res., 76: 4203—4207
- Lyman, J., 1957. Buffer Mechanism of Sea Water. Thesis, Univ. of California at Los Angeles, 196 pp.
- Murray, C.N. and Riley, J.P., 1971. The solubility of gases in distilled water and seawater — IV. Carbon dioxide. Deep-Sea Res., 18: 533—541
- Reamer, H.H., Olds, R.H., Sage, B.H. and Lacey, W.N., 1944. Phase equilibria in hydro-carbon systems. Methane-carbon dioxide system in the gaseous region. Ind. Eng. Chem., 36: 88—90
- Sengers, J.M.H. Levelt, Klein, M. and Gallagher, J.S., 1971. Pressure—Volume—Temperature Relationships of Gases — Virial Coefficients. U.S. N.B.S. Rept., U.S. Air Force Tech. Publ., AEDC-TR-71-39: 47 pp.
- Weiss, R.F., 1970. The solubility of nitrogen, oxygen and argon in water and seawater. Deep-Sea Res., 17: 721—735
- Weiss, R.F., 1971a. Solubility of helium and neon in water and seawater. J. Chem. Eng. Data, 16: 235—241
- Weiss, R.F., 1971b. The effect of salinity on the solubility of argon in seawater. Deep-Sea Res., 18: 225—230
- Wiebe, R. and Gaddy, V.L., 1939. The solubility in water of carbon dioxide at 50, 75 and 100°, at pressures to 700 atmospheres. J. Am. Chem. Soc., 61: 315—318
- Wiebe, R. and Gaddy, V.L., 1940. The solubility of carbon dioxide in water at various temperatures from 12 to 40° and at pressures to 500 atmospheres. Critical phenomena. J. Am. Chem. Soc., 62: 815—817

Exhibit F

- S7. Sonie, H. M., *J. Inst. Maths. Applic.* 13, 143-152 (1970).
 S8. Stringham, G. F., Simons, D. B., and Carr, H. P., *U.S. Naval Mater. Proj. Pap. 562-C* (1969).
 T1. Taneda, S., *J. Phys. Soc. Jpn.* 11, 92-96 (1956).
 T2. Toeoben, J. B., and Gauvin, W. H., *Crit. Rev. Fluid Mech.* 38, 142-183 (1980).
 U1. Underwood, R. L., *J. Fluid Mech.* 95, 114-119 (1979).
 V1. Van der Heijge Zijnen, R. G., *Phil. Soc. Roy. Soc. Spec. J.* 6, 129-140 (1980).
 W1. Wadell, H., *J. Geol.* 41, 310-331 (1933).
 W2. Wadell, H., *J. Franklin Inst.* 217, 459-490 (1934).
 W3. Wehrmann, O. H., *Phys. Fluids* 9, 228-235 (1966).
 W4. Weissberger, C., *Phys. Z.* 23, 219-224 (1922).
 W5. Willmarth, W. W., Hawk, N. E., and Harvey, R. L., *Phys. Fluids* 7, 197-208 (1964).
 W6. Woo, S. W., Ph.D. Thesis, McMaster Univ., Hamilton, Ontario, 1971.

Ellipsoidal Fluid Particles

Chapter 7

I. INTRODUCTION

The conditions under which fluid particles adopt an ellipsoidal shape are outlined in Chapter 2 (see Fig. 2.5). In most systems, bubbles and drops in the intermediate size range (d_e typically between 1 and 15 mm) lie in this regime. However, bubbles and drops in systems of high Morton number are never ellipsoidal. Ellipsoidal fluid particles can often be approximated as oblate spheroids with vertical axes of symmetry, but this approximation is not always reliable. Bubbles and drops in this regime often lack fore-and-aft symmetry, and show shape oscillations.

II. FLUID DYNAMICS

A. AIR-WATER SYSTEMS

Because of their practical importance, water drops in air and air bubbles in water have received more attention than other systems. The properties of water drops and air bubbles illustrate many of the important features of the ellipsoidal regime.

1. Water Drops in Air

Numerous determinations of the terminal velocities of water drops have been reported. The most careful measurements are those by Gunn and Klinzer (G13) and Beard and Pruppacher (B4). Figure 7.1, derived from these results,⁴ shows

⁴ Results for $Re < 300$ were included in the data used to derive the "standard drag curve" in Chapter 5. Numerical results for spherical raindrops valid for $Re < 200$ are also discussed in Chapter 5.

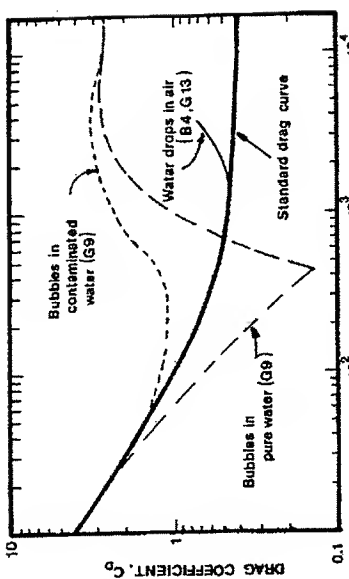


FIG. 7.2 Drag coefficient as function of Reynolds number for water drops in air and air bubbles in water, compared with standard drag curve for rigid spheres.

Water drops become unstable and tend to break up before they reach 1 cm diameter (see Chapter 12). Drops approaching this size show periodic shaft fluctuations of relatively low amplitude (J3, M4). As for other types of fluid particle, the internal circulation of water drops depends on the accumulation of surface-active impurities at the interface (H9). Observed internal velocities are of order 1% of the terminal velocity (G P5), too small to affect drag detectably. Ryan (R6) examined the effect of surface tension reduction by surface-active agents on falling water drops.

2. Air Bubbles in Water

Experimental terminal velocities for air bubbles rising in water are presented in Fig. 7.3 for the ellipsoidal regime and adjacent parts of the spherical air-spherical-cap regimes. Some of the spread in the data results from experimental scatter, but the greatest cause is surface contamination. For water drops in a system described in the previous section, surfactants have negligible effect on drag since κ is so high that internal circulation is small even in pure systems. For air bubbles in water, κ is so small that there is little viscous resistance to internal circulation, and hence the drag and terminal velocity are sensitive to the presence of surfactants.

The two curves in Fig. 7.3 are based on those given by Gaudin (G9) for distilled water and for water with surfactant added. The curves converge for small (spherical) bubbles, since even distilled water tends to contain sufficient surfactant to prevent circulation in this range (see Chapter 3), and for large (spherical-cap) bubbles, where surface tension forces cease to be important. Surface-active contaminants affect the rise velocity most strongly in the ellipsoidal range. Drag coefficients corresponding to these two curves appear in Fig. 7.2, and show that C_D for bubbles lies below the rigid sphere curve when

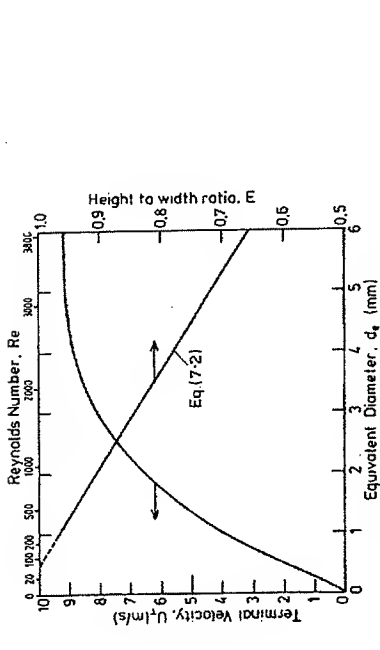


FIG. 7.1 Terminal velocity and aspect ratio of water drops falling freely in air at 20°C and 1 bar (B4, G13, P5).

terminal velocity and corresponding Reynolds number as a function of volume-equivalent diameter for water drops in air. Berry and Pranger (B7) and Beard (B3) give empirical polynomials describing the terminal velocity of drops in air, with Beard's equations covering a wider range of atmospheric conditions than the others. For water drops in air under normal atmospheric conditions at sea level, the simplest fit (B7), accurate within about 3%, gives

$$Re = \exp[-3.126 + 1.013 \ln N_D - 0.01912(\ln N_D)^2] \quad (7.1)$$

where N_D is defined by Eq. (5.15). For $d_e \leq 1$ mm ($Re \leq 300$), deviations from a spherical shape and internal circulation are so small that the correlations for rigid spheres in Chapter 5 may be used to predict terminal velocities. For $d_e \geq 20 \mu\text{m}$ (B3), correction for noncontinuum effects must be made (see Chapter 10). Pitter and Pruppacher (P4) studied the motion of 200 to 350 μm water drops undergoing freezing.

Drops larger than about 1 mm in diameter are significantly nonspherical; the mean height to width ratio is approximated (P5) by:

$$E = 1.030 - 0.062d_e \quad (1 < d_e < 9 \text{ mm}). \quad (7.2)$$

with d_e in mm. This ratio is plotted in Fig. 7.1. Figure 7.2 shows that deformation increases the drag coefficient above the value for a rigid sphere if C_D and Re are based on the volume-equivalent diameter d_e . The flattening of water drops at the front (lower) surface results from the increased hydrodynamic pressure there, while the rear has a more uniform hydrodynamic pressure and is therefore more rounded (M6). Blanchard (B9) discusses the popular misconception that raindrops fall with a teardrop shape. Figure 2.4(a) shows a photograph of a water drop in air. Shapes are discussed in detail in Section D.

7. Ellipsoidal Fluid Particles

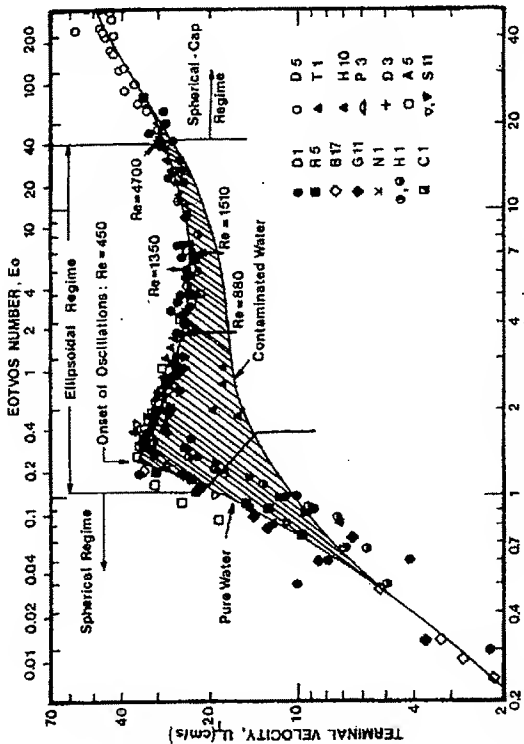


FIG. 7.3 Terminal velocity of air bubbles in water at 20°C.

internal circulation is present, but above if there is no internal circulation and the drag is dominated by deformation. For $d_e > 1.3$ mm, the uppermost (pure system) curve in Fig. 7.3 is approximated closely by

$$U_T = [(2.14 \sigma / \mu d_e) + 0.505 g d_e]^{1/2} \quad (7.3)$$

which is of the form suggested by a wave analogy (C2, M7).

Aybers and Tapucu (A4, A5) measured trajectories of air bubbles in water. When surface-active agents continue to accumulate during rise, the terminal velocity may never reach steady state (A4, B1) and may pass through a maximum (W4). Five types of motion were observed, listed in Table 7.1 with Re based on the maximum instantaneous velocity. Secondary motion of fluid par-

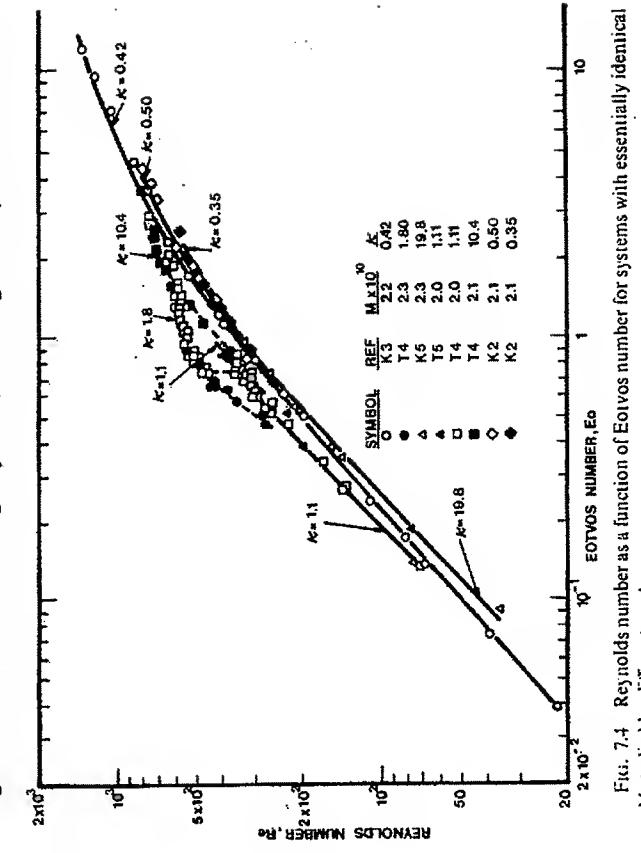


FIG. 7.4 Eotvos number as a function of Eotvos number for systems with essentially identical

TABLE 7.1

Motion of Intermediate Size Air Bubbles Through Water at 28.5°C ^a			
d_e (mm)	Re	E	Path
< 1.3	< 565	> 0.8	Rectilinear
1.3 to 2.0	565 to 880	0.8 to 0.5	Helical
2.0 to 3.6	880 to 1350	0.5 to 0.36	Plane [zig-zag] then helical
3.6 to 4.2	1350 to 1510	0.36 to 0.28	Plane [zig-zag]
4.2 to 17	1510 to 4700	0.28 to 0.23	Rectilinear but with rocking

^a Aybers and Tapucu (A4, A5).

Number $(2.0 \text{ to } 2.3 \times 10^{-10})$, but widely different values of κ (0.35 to 20). While the data exhibit some scatter, the observed dimensionless terminal velocities do not vary systematically with κ , but appear to reflect differences in system purity. Thorsen and coworkers (T4, T5) took greater care to purify their systems than the other authors and this is reflected in higher velocities. The internal fluid viscosity can be considered to be of secondary importance for systems in which no particular care has been taken to eliminate surfactants.

2. Effect of Surface-Active Contaminants

We may illustrate the effect of surfactants by comparing terminal velocities measured by different workers using the same system. Results for air bubbles in water have already been shown in Figs. 7.2 and 7.3. Results from six different studies on carbon tetrachloride drops falling through water are plotted in Fig. 7.5. The measured terminal velocities differ widely among different investigators, and one can only attribute these differences to differences in system purity. A number of workers have noted a strong influence of system purity on the drag or terminal velocity of ellipsoidal fluid particles [e.g. (E3, R1, S9, T1, T4, Z1)]. In a very careful study, Edge and Grant (E3) examined the effects of low concentrations of a surfactant, sodium lauryl sulphate, on the motion of dichloroethane drops descending through water. At very low surfactant concentrations (10^{-5} gm/liter or less) there was no observable effect. As the concentration was increased, a marked decrease in terminal velocity was observed for drops of equivalent diameter between 2 and 6 mm and this was usually accompanied by earlier boundary layer separation and irregular drop

oscillations. At relatively high surfactant concentrations (10^{-2} gm/liter or greater) the systems were said to be "grossly contaminated." The drop terminal velocities again became independent of surfactant concentration while the interface remained rigid, and oscillations became more regular. Very few workers have succeeded in eliminating all surface-active contaminants from their systems. Moreover, the type and concentration of contaminant present have seldom been characterized. Based on the available evidence, one may draw the following conclusions.

2. (i) Surfactants tend to damp out internal motion by rendering the interface rigid as discussed in Chapter 3. The influence of surfactants is most significant for low values of κ , since at large κ the viscous resistance of the interface fluid limits internal motion even for pure systems.
- (ii) Surfactants have the greatest influence on terminal velocity near the point of transition from rectilinear to oscillating motion. This is presumably because internal circulation can drastically alter the wake structure of a fluid particle (see below) leading to delayed boundary layer separation, wakes, and delayed vortex shedding.
- (iii) Surfactants play a particularly important role in high σ systems (e.g. air/water) since surface tension reductions are largest for these systems (see Chapter 3).
- (iv) Most of the experimental results in the literature are for "grossly contaminated" bubbles and drops. Since it is so difficult to eliminate surface-active contaminants in systems of practical importance, this is not a serious limitation.

3. Correlation for Contaminated Drops and Bubbles

There is a substantial body of data in the literature on the terminal velocities of bubbles and drops. In view of the influence of system purity discussed above a separation of this data has been made. Cases where there is evidence that considerable care was taken to eliminate surfactants and where a sharp peak in the U_T vs. d_e curve at low M and κ is apparent (as for the pure systems Figs. 7.3 and 7.5) are discussed in Section 4.

Grace *et al.* (G12) applied three types of correlation to a large body of experimental data: the form proposed by Klee and Treybal (K3); that of Hu and Kintner (H12) and its extension by Johnson and Braida (J2); and a wave analogy suggested for bubbles by Mendelson (M7) and extended by Marrucci *et al.* (M5). The second of these forms gave smaller residuals especially as M is increased. Even so, it was necessary to eliminate high M systems from the resulting correlation. Cases where wall effects were too significant were also eliminated from the data treated. The criteria which the data had to meet were then Eqs. (9-33) or (9-34) and

$$M < 10^{-3}, \quad Eo < 40, \quad Re > 0.1. \quad (7)$$

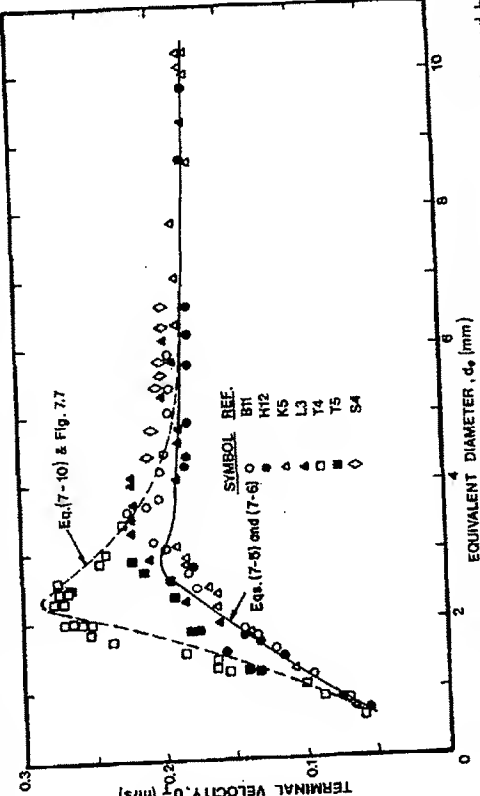


FIG. 7.5 Terminal velocity of carbon tetrachloride drops falling through water, measured by

The indices in the original Johnson and Braida correlation and the point of intersection between the two linear regions were adjusted to improve the agreement with all the data meeting the above criteria. The resulting correlation (G12) is:

$$J = 0.94H^{0.757} \quad (7-5)$$

and

$$J = 3.42H^{0.441} \quad (7-6)$$

where

$$H = \frac{2}{3} E_0 M^{-0.149} (\mu/\mu_w)^{-0.14}, \quad (7-7)$$

$$J = Re M^{0.149} + 0.857, \quad (7-8)$$

and μ_w is the viscosity of water in Braida's experiments, which may be taken as 0.0009 kg/ms (0.9 cp).

A plot of every fourth data point and the lines given by Eqs. (7-5) and (7-6) appears in Fig. 7.6. The gradient discontinuity corresponds approximately to the transition between nonoscillating and oscillating bubbles and drops. In the above correlation, the terminal velocity appears only in the dimensionless group J , and may be expressed explicitly as:

$$U_T = \frac{\mu}{\rho d_e} M^{-0.149}(J - 0.857). \quad (7-9)$$

The r.m.s. deviation between measured and predicted terminal velocities is about 15% for the 774 points with $H \leq 59.3$ and 11% for the 709 points with $H > 59.3$. This correlation is recommended for calculations of bubble and drop terminal velocities when the criteria outlined above are satisfied and where some surface-active contamination is inevitable. The predictions from this correlation for carbon tetrachloride drops in water are shown on Fig. 7.5. Many other correlations for calculating the terminal velocity of bubbles and drops are available [e.g. (H12, J2, K3, T1, V1, W2)]. None covers such a broad range of data as Eqs. (7-5) and (7-6). Moreover, a number of the earlier correlations require that values be read from graphs or that iterative procedures be used to determine U_T .

4. Correlation for Pure Systems

In view of the limited data available for pure systems, Grace *et al.* (G12) modified the correlation given in the previous section rather than proposing an entirely different correlation. A correction of somewhat similar form to that suggested in Chapter 3 for low Re is employed; i.e.,

$$(U_T)_{\text{pure}} = U_T[1 + \Gamma/(1 + \kappa)]. \quad (7-10)$$

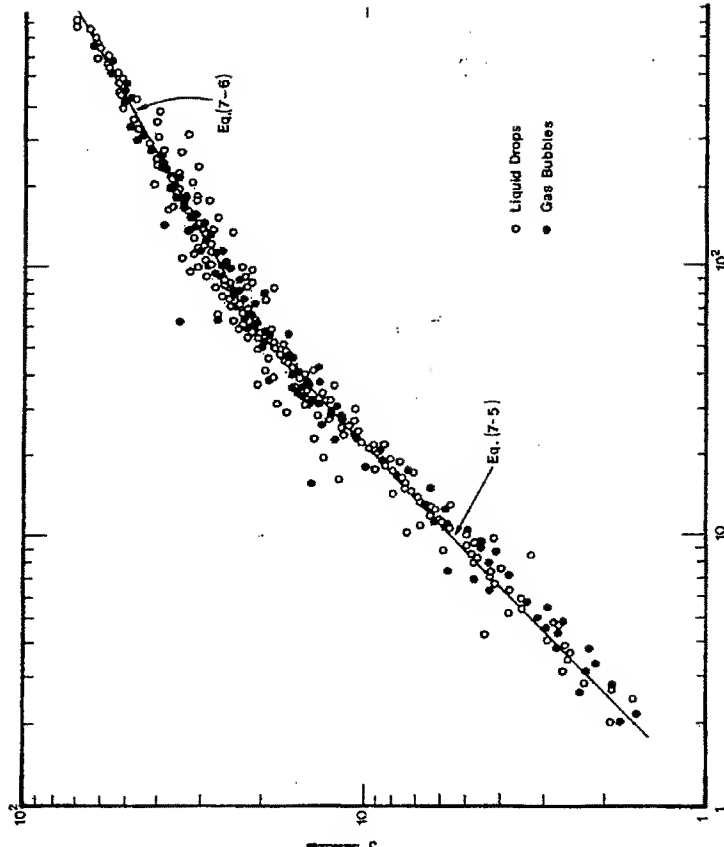


FIG. 7.6 Data (showing one point in four) used to obtain general correlation for terminal velocity of drops and bubbles in contaminated liquids, compared with Eqs. (7-5) and (7-6) (B11, B17, D2, E3, E4, G9, G10, G14, H1, H12, J4, K2, K3, L3, L11, P3, T1, W3, Y4).

where Γ is to be obtained experimentally and U_T is predicted using Eqs. (7-5) to (7-9). Since the continuous fluid was water for all the pure systems for which data are available, μ and M cover very restricted ranges. Experimental values of Γ are plotted in Fig. 7.7 as a function of $E(1 + 0.1\kappa)/(1 + \kappa)$, where the function of κ was chosen to reduce the spread in the resulting points.

Careful purification of a system has little effect for small and large drops and bubbles. Hence Γ reaches a maximum for a particular value of the abscissa and decreases to zero at large and small values of the abscissa. An envelope has been drawn to provide an estimate of the maximum increase in terminal velocity for bubbles and drops in pure systems over that for contaminated systems. This envelope, together with Eq. (7-10) and the correlation of the previous section, have been used to obtain the upper curve in Fig. 7.5 for carbon tetrachloride drops in water. The curve gives a good representation of the higher velocities observed for carefully purified systems.

drops, data of Finlay (F1) and Van der Leeden *et al.* (V2) can be correlate with the best data for water drops in air (B4, G13) by the equations

$$Re = 1.62 E_0^{0.755} M^{-0.25} \quad (0.5 \leq E_0 \leq 1.84). \quad (7-1)$$

$$Re = 1.83 Eo^{0.555} M^{-0.25} \quad (1.84 \leq Eo \leq 5.0). \quad (7-1)$$

$$\text{Re} \equiv L U E_0^{-1/2} M^{-1/2}, \quad (E_0 \geq 3.0). \quad (/-)$$

Equation (7-13) predicts that the terminal velocity approaches an upper limit

$$U_1 = 2.0(\Delta\rho g\sigma/\rho^2)^{1.4}, \quad (7-1)$$

independent of the drop size and the viscosity of the gas

An alternative correction given by Garner and Lihou (GS) based on data independent of the droplet size and the viscosity of the gas.

This form of correlation was used by Beard (B3) to suggest a correlation for water drops in air under different atmospheric conditions. It should be used with caution for gases with properties widely different from air under atmospheric conditions.

$$Re = 0.77 E_0^{0.66} M^{-0.28} \quad (E_0 \leq 164M^{1.6}), \quad (7-1)$$

correlation was used by Beard (B3) to suggest a correlation β

This form of correlation was used by Beard (B3) to suggest a correlation for water drops in air under different atmospheric conditions. It should be used with caution for gases with properties widely different from air under atm

It is an open question whether small quantities of surfactants, too spherical conditions, but the range of liquid properties covered is broad. Influence the cross-numbered affect the terminal velocity of liquid drops.

influence the gross properties, affect the terminal velocity or liquid drops in air. This appears unlikely in view of the large values of κ , but Buzzard and Nedderman (B18) have claimed such an influence. Acceleration may have contributed to this observation. Quantities of surfactant large enough to low appreciably can lead to significantly increased deformation and hence to a increase in drag and a reduction in terminal velocity (B18).

D. SUDARSESNA: EVIDENCE FROM BANGLADESH

In aqueous systems it should be used with caution for

C. TERMINAL VELOCITIES OF LIQUID DROPS IN AIR

As indicated in Chapter 2, liquid drops falling through gases have such extreme values of γ and κ that they must be treated separately from bubbles and drops in liquids. Few systems have been investigated aside from water drops in air, discussed above, and what data are available for other systems (F_1, G_5, L_5, V_2) show wide scatter. Rarely have gases other than air been used.

As noted in Chapters 2 and 3, deformation of fluid particles is due to inert effects. For low Re and small deformations, Taylor and Acrivos (T3) used matched asymptotic expansion to obtain, to terms of order We^2/Re , cycles.

$$\frac{r(\theta)}{\theta} = 1 - i \cdot \operatorname{We} P_2(\cos \theta) - \frac{3\zeta(11\kappa + 10)}{70(1 + \kappa)} \frac{\operatorname{We}^2}{\operatorname{Re}} P_3(\cos \theta). \quad (7-1)$$

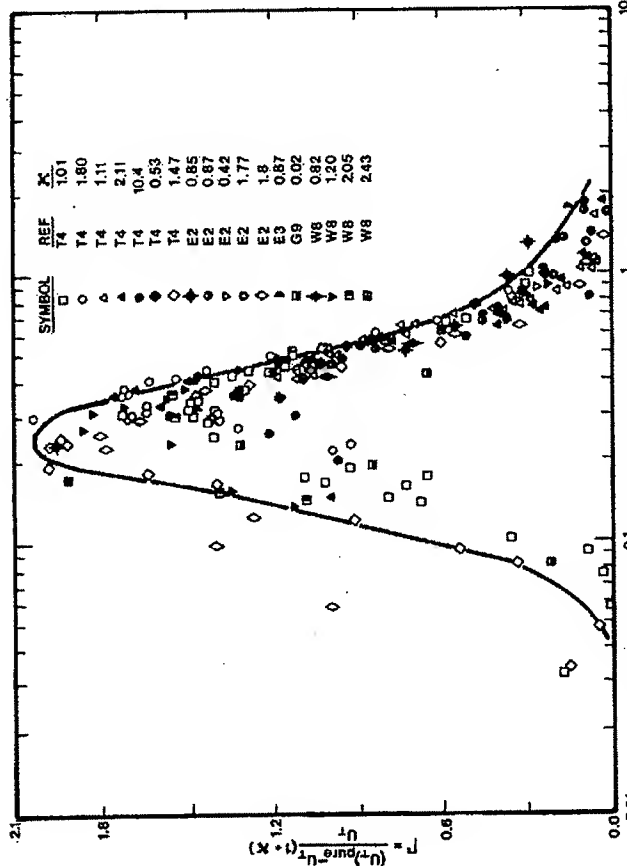


Fig. 7.7 Corection factor Γ , relating terminal velocity in pure systems to value in corresponding contaminated systems (E2, E3, G9, T4).

The envelope in Fig. 7.5 is for the maximum increase in terminal velocity obtainable by eliminating surface-active contaminants. For systems of intermediate purity, Γ may be assigned a value between zero and that given by the envelope. Since the envelope has been derived solely from experiments for aqueous systems, it should be used with caution for nonaqueous systems.

As indicated in Chapter 2, liquid drops falling through gases have such extreme values of γ and κ that they must be treated separately from bubbles and drops in liquids. Few systems have been investigated aside from water drops in air, discussed above, and what data are available for other systems (F_1, G_5, L_5, V_2) show wide scatter. Rarely have gases other than air been used.

As noted in Chapters 2 and 3, deformation of fluid particles is due to inert effects. For low Re and small deformations, Taylor and Acrivos (T3) used matched asymptotic expansion to obtain, to terms of order We^2/Re ,

that they cannot be used with confidence.

where

$$\lambda = \frac{1}{32(1+\kappa)^3} \left\{ (3 + 10.3\kappa + 11.4\kappa^2 + 4.05\kappa^3) - \frac{(1 + \kappa)(\kappa - 1)}{3} \right\}. \quad (7.18)$$

P_2 and P_3 are the second- and third-order Legendre polynomials. For small We , the deformed bubble or drop is predicted to be exactly spheroidal. In principle, the spheroid may be either prolate or oblate, but for cases of physical significance oblate shapes are predicted. If $Re_p \gg 1$, droplet shapes are predicted to differ only slightly from the case where both Re and Re_p are small (P1). Brignell (B14) extended the series expansion to terms of order $We Re^2$. Since deformation at low Re is only observable for high M systems, this approach is of little practical value.

At larger Re and for more marked deformation, theoretical approaches have had limited success. There have been no numerical solutions to the full Navier-Stokes equation for steady flow problems in which the shape, as well as the flow, has been an unknown. Savic (S3) suggested a procedure whereby the shape of a drop is determined by a balance of normal stresses at the interface. This approach has been extended by Pruppacher and Pitter (P6) for water drops falling through air and by Waregi (W1) for drops and bubbles in liquids. The drop or bubble adopts a shape where surface tension pressure increments, hydrostatic pressures, and hydrodynamic pressures are in balance at every point. Thus

$$\Delta\rho g y + \sigma[(1/R_1) + (1/R_2) - (2/R_0)] + p_{HD} - (p_{HD})_p = 0, \quad (7.19)$$

where y is measured vertically upwards from the lowest point, 0, of the drop; R_1 and R_2 are the principal radii of curvature at a general point on the surface ($R_1 = R_2 = R_0$ at 0); and p_{HD} and $(p_{HD})_p$ are the pressures due to the external and internal fluid motions, respectively, less the stagnation pressures. It is usual practice to assume that $(p_{HD})_p \ll p_{HD}$, although this has been criticized by Foote (F2). With this assumption, drop shapes can be determined if the distribution of p_{HD} is known. Savic assumed that the pressure distribution was the same as that about a rigid sphere at the same value of Re : Pruppacher and Pitter used the same approach, with more recent and reliable pressure data. Deformations were assumed small and the shape represented by a cosine series (P6, S3) or by Legendre polynomials (W1). The general procedure is the reverse of that employed by McDonald (M6) to calculate surface dynamic pressure distributions from observed drop shapes. The predictions become less realistic with increasing particle size and deformation because of increasing error in the assumed pressure distribution.

A reasonable approximation to the observed profile of many drops and bubbles is a combination of two half oblate spheroids with a common major axis and different minor axes (B8, F1). This observation has been used (W1) to propose a model from which bubble and drop shapes can be estimated at

high Re . The pressure distribution over the front surface is assumed to be the potential flow pressure distribution over a complete spheroid of the same eccentricity, while the dynamic pressure over the rear is assumed uniform;¹ that the rear deforms like a sessile drop or bubble of the same size in the same system.² The theory correctly predicts that drops in air deform most at the front, while some systems (e.g., bubbles in water) begin by flattening more at the front, then deforming more at the rear with increasing d_e .

2. Experimental Results for Bubbles and Drops in Liquids

It is possible to prepare a generalized plot of mean aspect ratio \bar{E} , where E is maximum vertical dimension, maximum horizontal dimension. In the literature both We and Eo are commonly used as independent variables for correlating shape parameters for fluid particles. The Eotvos number gives a better overall representation (G12). As in Section B, it is necessary to separate data for drops falling through air (see Section 4) and for very pure systems (see Section 5). The generalized graphical correlation for bubbles and drops in contaminated liquid media is given in Fig. 7.8. Wall effects have been eliminated using the same criteria as for terminal velocities, i.e., Eqs. (9-33) and (9-34).

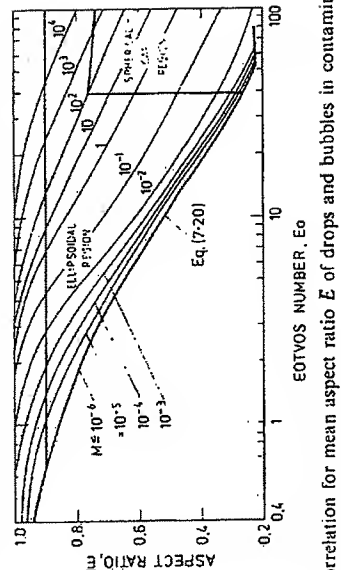


Fig. 7.8 Correlation for mean aspect ratio E of drops and bubbles in contaminated systems (B10, H7, K2, K3, K4, T6, W1, W6, Y4).

From Fig. 7.8 it is clear that deformation depends not only on Eo but also on M ; higher M giving rise to less deformation at the same Eo . For low M it is reasonable to correlate the data by a single line:

$$\bar{E} = 1/(1 + 0.163 Eo^{0.757}) \quad (Eo < 40, M \leq 10^{-6}). \quad (7.2)$$

Given by Wellek et al. (W6), for higher M , Fig. 7.8 can be used to estimate the height-to-width ratio of bubbles and drops in liquids. An alternative correlation

¹ Previous workers have also made use of potential flow pressure distributions about spheroids but no allowance was made for lack of fore-and-aft symmetry, while the constant pressure condition was satisfied only near the front stagnation point (S1) or at the equator and poles (H6, M1).

obtained by Tadaki and Maeda (T1) for air bubbles with $M < 10^{-3}$ expresses $d_e/2a = E^{1/3}$ (where $2a$ is the maximum horizontal dimension) as a function of a dimensionless group $Ta = Re M^{0.23}$. Vakrushev and Efremov (V1) extended this approach to give:

$$E = 1 \quad (Ta \leq 1), \quad (7-21)$$

$$E = [0.81 + 0.206 \tanh(2(0.8 - \log_{10} Ta))]^3, \quad (1 \leq Ta \leq 39.8), \quad (7-22)$$

$$E = 0.24 \quad (Ta \geq 39.8) \quad (7-23)$$

Equation (7-23) implies a spherical-cap shape with an included angle of about 50° (see Chapter 8).

3. Experimental Results for Pure Systems

Drops and bubbles in highly purified systems are significantly more deformed than corresponding fluid particles in contaminated systems. Increased flattening of fluid particles in pure systems results from increased inertia forces related to the increased terminal velocities discussed above. Some experimental results for drops and bubbles in water (low M systems) are shown in Fig. 7.9. The

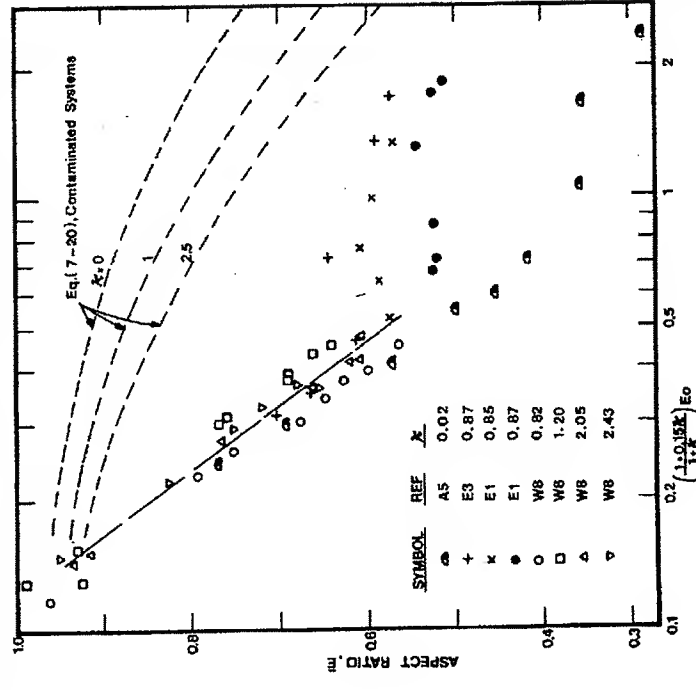


Fig. 7.10. The data can be represented by the relationships given in Fig. 7.10. The shape factor, $b_1/(b_1 + b_2)$, is also plotted in Fig. 7.10 based on data given by Finlay (F1). The relationships

$$\frac{b_1 + b_2}{2a} \approx 1.0 \quad (Eo \leq 0.4), \quad (7-24)$$

$$\frac{b_1 + b_2}{2a} = \frac{1.0 + 0.18(Eo - 0.4)^{0.8}}{1.0 + 0.12(Eo - 0.5)^{0.8}} \quad (0.4 < Eo < 8), \quad (7-25)$$

The shape factor, $b_1/(b_1 + b_2)$, is also plotted in Fig. 7.10 based on data given by Finlay (F1). The relationships

$$\frac{b_1}{b_1 + b_2} = 0.5 \quad (Eo \leq 0.5), \quad (7-26)$$

$$\frac{b_1}{b_1 + b_2} = \frac{0.5}{1.0 + 0.12(Eo - 0.5)^{0.8}} \quad (0.5 < Eo < 8) \quad (7-27)$$

give an adequate fit to the data. Equations (7-25) and (7-27) are plotted

Fig. 7.10.

A good approximation to the shape of deformed drops in air may therefore be obtained from knowledge of the system properties and drop size. The ratios $(b_1 + b_2)/2a$ and $b_1/(b_1 + b_2)$ are calculated from Eo using Eqs. (7-24) and (7-27). From geometric considerations

$$d_e/a = 2 \left[\frac{b_1 + b_2}{2a} \right]^{1/3}, \quad (7-28)$$

so that the semiminor axes can then be calculated. The surface area may be estimated by again assuming that the drop is composed of two halfspheroids, i.e.

$$A = 2\pi a^2 + \frac{\pi}{2} \left\{ \frac{b_1^2}{e_1} \ln \left(\frac{1+e_1}{1-e_1} \right) + \frac{b_2^2}{e_2} \ln \left(\frac{1+e_2}{1-e_2} \right) \right\}, \quad (7-29)$$

where $e_1 = (1 - b_1^2/a^2)^{1/2}$ and $e_2 = (1 - b_2^2/a^2)^{1/2}$ are the eccentricities of the

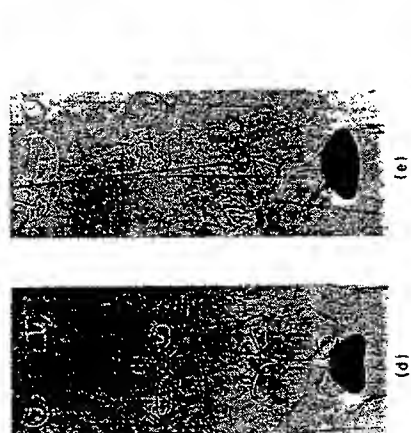
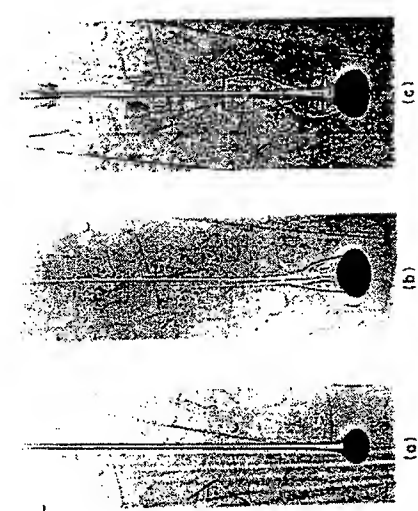


Fig. 7.11 Wake configurations for drops in water (highly purified system) reproduced from Winnikow and Chao (W8) with permission. (a) nonoscillating nitrobenzene drop; $d_c = 0.250$ cm, $Re = 515$; steady thread-like laminar wake; (b) nonoscillating *m*-nitrotoluene drop; $d_c = 0.380$ cm, $Re = 688$; steady thread accompanied by attached toroidal vortex wake; (c) oscillating nitrobenzene drop; $d_c \approx 0.380$ cm, $Re \approx 686$; central thread plus axisymmetric outer vortex sheet rolled inward to give inverted bottle shape of wake; (d) oscillating nitrobenzene drop; $d_c = 0.454$ cm, $Re = 775$; vortex sheet in (e) has broken down to form vortex rings; (e) oscillating nitrobenzene drop; $d_c = 0.490$ cm, $Re = 804$; vortex rings in (d) now shed asymmetrically, and the drop exhibits a rocking motion.

critical value should be (E2, H6, W8), and the value of Re and purity of the system appear to be better indicators of the likelihood of secondary motion. While wake shedding appears to provide the excitation for shape oscillation the frequency of the two phenomena may differ. For example, Winnikow and Chao (W8) measured oscillation frequencies between about 60 and 80 of wake shedding frequencies for nitrobenzene drops in water, while Ed et al. (E1) found the two frequencies to be identical. To obtain a simple physical understanding of shape oscillations, consider forced vibration of a single degree-of-freedom damped system [see, e.g., Anderson (A2)]. Suppose that wake shedding provides a harmonic excitation of frequency f_w , while the natural frequency of the drop is given (1.1) by

$$f_n = \sqrt{\frac{48\sigma}{\pi^2 d_c \rho(2 + 3\gamma)}} \quad (7.3)$$

If we define

$$\bar{f} = (f_w + f_n)/2 \quad (7.3)$$

and

$$\Delta f = (f_w - f_n)/2, \quad (7.3)$$

and if $\Delta f \ll \bar{f}$, then the motion is approximately

$$E = E_0 \times \frac{\bar{f}}{\Delta f} \sin(2\pi \bar{f} t) \cos(2\pi \bar{f} t). \quad (7.3)$$

As illustrated in Fig. 7.12, the drop then oscillates at frequency \bar{f} with an amplitude modulated at frequency Δf .

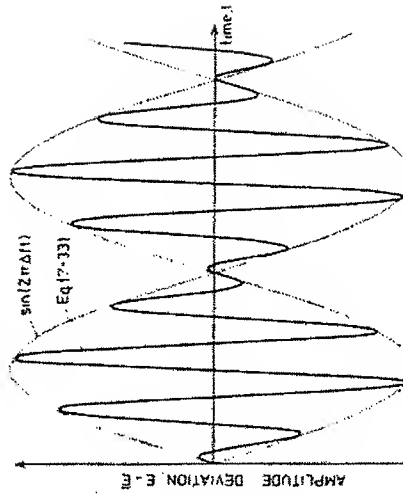


Fig. 7.12 Simple model to show nature of shape oscillations for bubbles and drops in motion.

In practice, this model is oversimplified since the exciting wake shedding is by no means harmonic and is itself coupled with the shape oscillations and since Eq. (7-30) is strictly valid only for small oscillations and stationary fluid particles. However, this simple model provides a conceptual basis to explain certain features of the oscillatory motion. For example, the period of oscillation, after an initial transient (E1), becomes quite regular while the amplitude is highly irregular (E3, S4, S5). "Beats" have also been observed in drop oscillations (D4). If f_w and f_n are of equal magnitude, one would expect resonance to occur, and this is one proposed mechanism for breakage of drops and bubbles (Chapter 12).

Equation (7-30) gives the natural frequency of the fundamental mode for stationary fluid particles undergoing small oscillations with viscous forces neglected. It has been modified to account for viscous effects (L4, M10, S10), surface impurities (M10), finite amplitudes (S5, Y1), and translation (S10). Observed oscillation frequencies are generally less than those given by Eq. (7-30), typically by 10–20% for drops in free motion in impure systems (S4) and by 20–40% for pure systems (E1, E3, W8, Y1). The amplitude tends to be larger for pure systems (E3) and this explains the reduction in frequency.

In general, oscillations may be oblate-prolate (H8, S5), oblate-spherical, or oblate-less oblate (E2, F1, H8, R3, R4, S5). Correlations of the amplitude of fluctuation have been given (R3, S5), but these are at best approximate since the amplitude varies erratically as noted above. For low M systems, secondary motion may become marked, leading to what has been described as "random wobbling" (E2, S4, W1). There appears to have been little systematic work on oscillations of liquid drops in gases. Such oscillations have been observed (F1, M4) and undoubtedly influence drag as noted earlier in this chapter. Measurements (Y3) for 3–6 mm water drops in air show that the amplitude of oscillation increases with d_e , while the frequency is initially close to the Lamb value (Eq. 7-30) but decays with distance of fall.

Oscillating bubbles and drops may travel along zig-zag or spiral (helical) paths. Some authors have observed only one of these modes while others have observed both. There is some evidence that the type of secondary motion is affected by the mode of release (M8). Saffman (S1) performed a careful series of experiments on air bubbles in water. Rectilinear motion was found to become unstable, and gave rise to zig-zag motion which in turn gave way to spiral motion for larger bubbles.[†] The paths followed by fluid particles undergoing secondary motion are no doubt associated with the type of wake. Details of the paths, orientation, and periods of spiralling and zig-zagging drops and bubbles are presented by Mercier and Rocha (M9) and Tsuge and Hibino (T6).

Secondary motion plays an important role in increasing drag (L7) and in promoting heat and mass transfer from bubbles or drops. The onset of oscillations corresponds approximately to the maximum in $U_{rl}(d_e)$ and minimum in

[†] See also Table 7.1.

C_D/Re curves for drops and bubbles (B11, E1, E2, T4). The influence of oscillations on heat and mass transfer is discussed in Section III.

G. INTERNAL CIRCULATION

Surface-active contaminants play an important role in damping out internal circulation in deformed bubbles and drops, as in spherical fluid particles (see Chapters 3 and 5). No systematic visualization of internal motion in ellipsoid bubbles and drops has been reported. However, there are indications that deformations tend to decrease internal circulation velocities significantly (M11), while shape oscillations tend to disrupt the internal circulation pattern droplets and promote rapid mixing (R3). No secondary vortex of opposite sense to the prime internal vortex has been observed, even when the external boundary layer was found to separate (S11).[‡]

H. THEORETICAL SOLUTIONS FOR DEFORMED BUBBLES AND DROPS

Attempts to obtain theoretical solutions for deformed bubbles and drops are limited, while no numerical solutions have been reported. A simplifying assumption adopted is that the bubble or drop is perfectly spheroidal. Saffman (S1) considered flow at the front of a spheroidal bubble in spiral or zig-zag motion. Results are in fair agreement with experiment. Harper (H4) tabulated energy dissipation values for potential flow past a true spheroid. Moore (M1) applied a boundary layer approach to a spheroidal bubble analogous to that for spherical bubbles described in Chapter 5. The interface is again assumed to be completely free of contaminants. The drag is given by

$$C_D = \frac{48}{Re} f_1(E) \left[1 + \frac{f_2(E)}{Re^{1/2}} \right], \quad (7-3)$$

where the first term results from the viscous energy dissipation for irrotational flow past an oblate spheroid, and the second arises from dissipation in the boundary layer and wake. Harper (H5) tabulated values of $f_1(E)$ and $f_2(E)$ and plotted drag curves for four values of M . The curves show minima and are qualitatively in agreement with observed $C_D(Re)$ curves for bubbles. No attempt has been reported to extend this treatment to deformed drops of low κ .

III. HEAT AND MASS TRANSFER

A. REGIMES OF MOTION AND TRANSFER

The flow and shape transitions for small and intermediate size bubbles and drops are summarized in Fig. 7.13. In pure systems, bubbles and drops circulate freely, with internal velocity decreasing with increasing κ . With increasing κ they deform to ellipsoids, finally oscillating in shape when Re exceeds a value of order 10^3 . In contaminated systems spherical and nonoscillating ellipsoid

where a' is the amplitude of the oscillation, $Re_e = 4d_e/f\tau/v$ is the vibrational Reynolds number, and f is the frequency. Rearranging Eq. (7-35) yields:

$$\frac{a'f}{U_T} < 0.05 \left(\frac{2a'}{d} \right)^{0.45} \quad (7-3)$$

Assuming spherical-oblate oscillations with amplitude $2a' = (1 - E)d_e$, taking $E = 0.5$ as a rough approximation and replacing d by d_e and f by f_N from Eq. (7-30), we find no effect of oscillation on the external resistance if

$$d_e f_N / U_T < 0.15. \quad (7-3)$$

For liquid drops in gases the terminal velocity is so large that the inequality is obeyed and oscillation has essentially no effect on transfer. For drops or bubbles in liquids, the effect of oscillation on transfer is significant.

B. DEFINITIONS

Fig. 7.13 Flow transitions for bubbles and drops in liquids (schematic).

bubbles and drops are effectively rigid but, for $Re > 200$, wake shedding and shape oscillations occur with associated motion of the internal fluid. In systems of intermediate purity, small bubbles and drops are rigid but, with increasing size, they become deformed and partially circulating. Circulation increases with increasing size, and shape oscillations occur at $Re > 200$. The Reynolds number marking the transition from rigid to circulating behavior depends on system purity.

These flow transitions lead to a complex dependence of transfer rate on Re and system purity. Deliberate addition of surface-active material to a system with low to moderate κ causes several different transitions. If $Re < 200$, addition of surfactant slows internal circulation and reduces transfer rates to those for rigid particles, generally a reduction by a factor of 2–4 (S6). If $Re > 200$ and the drop is not oscillating, addition of surfactant to a pure system decreases internal circulation and reduces transfer rates. Further additions reduce circulation to such an extent that shape oscillations occur and transfer rates are increased. Addition of yet more surfactant may reduce the amplitude of the oscillation and reduce the transfer rates again. Although these transitions have been observed (G7, S6, T5), additional data on the effect of surface active materials are needed.

The internal resistance is always decreased substantially when a bubble or drop oscillates, but the external resistance may be unaffected if the Reynolds number is high enough. A rough criterion can be obtained from Eq. (11-63) for vibration of a particle in an axial stream. Oscillation has negligible effect on the external resistance if

$$\frac{Re_v \left(\frac{2a}{d} \right)^{-0.45}}{Re \left(\frac{d}{d_e} \right)} < 0.2, \quad (7-35)$$

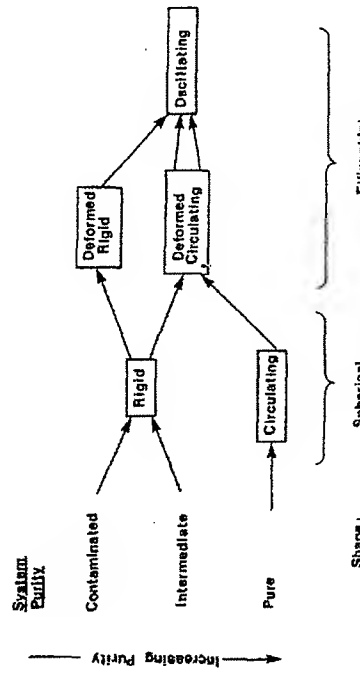


Fig. 7.13 Flow transitions for bubbles and drops in liquids (schematic).

Mass transfer rates from drops are obtained by measuring the concentration change in either or both of the phases after passage of one or more drops through a reservoir of the continuous phase. This method yields the average transfer rate over the time of drop rise or fall, but not instantaneous values. For measurements of the resistance external to the drop this is no drawback, because the resistance is nearly constant, but the resistance within the drop frequently varies with time. The fractional approach to equilibrium, F , is calculated from the compositions and is then related to the product of the overall mass transfer coefficient and the surface area:

$$(\bar{KA})_p = -(\pi d_e^3 / 6t) \ln(1 - F), \quad (7-34)$$

where t is the time of free rise or fall and $(\bar{KA})_p$ is the time-average coefficient area product based on dispersed phase concentrations. If the resistance in each phase may be added,

$$\frac{1}{(\bar{KA})_p} = \frac{H}{\bar{KA}} + \frac{1}{(\bar{KA})_e}, \quad (7-35)$$

If the resistance external to the drop is negligible,

$$(\bar{KA})_p = -(\pi d_e^3 / 6t) \ln(1 - F). \quad (7-40)$$

Many investigators base mass transfer coefficients upon the area of the volume equivalent sphere, especially for oscillating drops:

$$(\bar{KA})_p / A_e = -(d_e / 6t) \ln(1 - F). \quad (7-41)$$

The Sherwood number based on this coefficient is

$$Sh_{pe} = [(\bar{KA})_p / A_e] d_e / \mathcal{D}_p. \quad (7-42)$$

A similar definition is frequently used for the continuous phase Sherwood number

$$\text{Sh}_e = [\kappa A_e / A_s] d_e / \zeta \quad (7-43)$$

In some studies the surface area of the particle is measured and area-free Sherwood numbers are reported

$$\text{Sh}_p = k_p d_e / \zeta_p, \quad (7-44)$$

$$\text{Sh} = k d_e / \zeta. \quad (7-45)$$

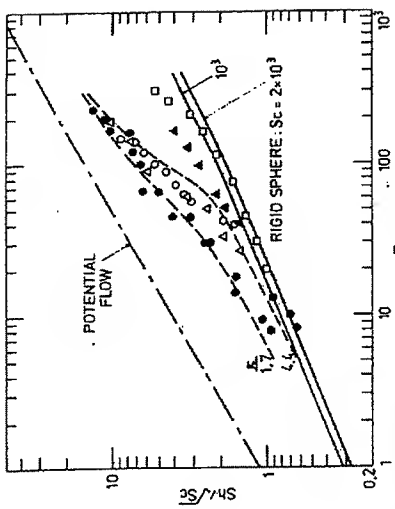
Careful reading of papers is required to determine which definition has been used. Measurements of the continuous phase resistance around bubbles frequently use photographic, volumetric, or pressure change techniques to yield instantaneous rates of mass transfer, and thus k_A . Here too, both definitions of the Sherwood number, Eqs. (7-43) and (7-45), have been used.

C. EXTERNAL RESISTANCE

Figure 7.14 gives area-free Sherwood numbers for organic drops in water. In the furfural-water system ($\kappa = 1.7$), the transition from circulation at low Re to circulation at high Re agrees well with the treatment of Chapter 5, i.e., deformation has little effect on the area-free Sherwood number. For this value of κ , however, it is not clear whether the drops were circulating for $\text{Re} < 10$. For the diol-water system, ($\kappa = 80$), circulation is so slow that Sh agrees with the result for rigid spheres up to $\text{Re} \approx 200$ where oscillation begins. At this Reynolds number, $d_e f_N / U_T \approx 0.6$ and oscillations are expected to affect the Sherwood number; see Eq. (7-37). The chlorobenzene/benzene drop system ($\kappa = 0.7$) shows the effect of addition of surfactant. Without surfactant, Sh departs from the line for solids at $\text{Re} \approx 20$ and deviation increases with Re as circulation becomes stronger. The data with added surfactant follow the line for solids up to $\text{Re} \approx 50$ and remain below the pure system values at higher Re . Even the system without surfactant was contaminated, since the data should lie above those for $\kappa = 1.7$. The presence of surface-active materials acts in the same way as an increase in the drop viscosity with respect to terminal velocity. Transition from a stagnant drop to a drop with circulation may occur at any Re below 200. The data for aniline drops ($\kappa = 4.4$) lie between the systems with $\kappa = 1.7$ and 80, and show reasonable agreement with Eq. (5-39). Oscillation in contaminated systems and circulation in less contaminated systems both cause Sh to rise more rapidly than $\text{Re}^{1/2}$.

1. Particles without Shape Oscillations

For nonspherical particles the only theoretical treatment available is for potential flow around a spheroid (L10). For an oblate spheroid the area-free



Symbol	κ	γ	Sc	Ref.
□	80	0.95	1660	(G8)
○	4.4	1.02	1100	(H11)
●	1.7	1.16	975	(G8, H11)
△	0.7	1.02	1020	(T5)
				same as △, but contaminated with 10^{-3} gm/liter sodium oleyl-p-aminidine sulfonate Eq. (5-39)
—				Rigid sphere, Eq. (5-25), Table 5.4E
—				Sphere in potential flow, Eq. (5-35)
-				

Fig. 7.14 Area-free mass transfer factors. Sh , γ , Sc for drops.
Sherwood number is
$$\text{Sh} = \frac{2}{\sqrt{\pi}} \text{Pe}^{1/2} \left[\frac{8\epsilon^2 E^{1/3}}{3(\sin^{-1} \epsilon - \epsilon E)} \right]^{1/2} \left[1 + \frac{E^2}{2\epsilon} \ln \left(\frac{1+\epsilon}{1-\epsilon} \right) \right], \quad (7-4)$$
 where Pe is based on d_e and

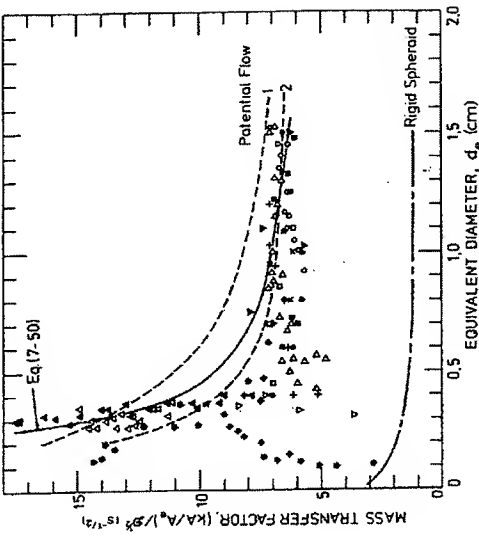
$$\epsilon = (1 - E^2)^{1/2}. \quad (7-4)$$

Since the area ratio is given by

$$\frac{A}{A_e} = \frac{1}{2E^{2/3}} \left[1 + \frac{E^2}{2\epsilon} \ln \left(\frac{1+\epsilon}{1-\epsilon} \right) \right], \quad (7-4)$$

then

$$\text{Sh}_e = \frac{2}{\sqrt{\pi}} \text{Pe}^{1/2} \left[\frac{2\epsilon^3}{3E(\sin^{-1} \epsilon - \epsilon E)} \right]^{1/2}. \quad (7-4)$$



Experimental Data					
Symbol	Gas	Ref.	Symbol	Gas	Ref.
+	CO ₂	(I1)	△	CO ₂	(Z2)
*	CO ₂	(W4)	▽	CO ₂	(R1) ^a
●	CO ₂	(C1)	○	O ₂	(Y3)
◇	CO ₂	(G15)	▲	C ₂ H ₂	(L2)
△	CO ₂	(D3)	×	C ₂ H ₄	(J1)
▼	CO ₂	(B2)	◆	C ₂ H ₄	(G3)
■	CO ₂	(L6)	□	C ₂ H ₈	(J1)

^a As Δ, but with 1.2 ppm n-nananol.

Fig. 7.15 Mass transfer factor (kA/A_e) $^{1/2}$ for gas bubbles in water.

Comparison of these equations shows that the area-free Sherwood number is only slightly affected by eccentricity; e.g. $Sh/Pe^{1/2}$ for a spheroid with $E = 0.4$ is only 8.5% larger than that for the equivalent sphere while the area ratio A/A_e is 17% larger. Therefore, we expect little effect of deformation on the area-free Sherwood number for bubbles and drops at high Re . This is borne out by the agreement of the data in Fig. 7.14 with Eq. (5-39), derived for fluid spheres.

a. *Drops in Gases* For liquid drops in gases at low pressure the equations for solid particles in Chapter 6 can be used to predict heat and mass transfer rates. Figure 7.10 shows the area ratio α and the ratio L/d_e as functions of Ec , to facilitate use of Eq. (6-34), while areas may be calculated from Eq. (7-29) or from Eq. (7-48). Surface-active materials should have little effect. For drops in high-pressure gases, oscillations may become important if $Re > 200$ and the terminal velocity is small enough that $d_e f_n U_T > 0.1$.

Near the point of drop release, transfer coefficients can be much different from those predicted, due to large amplitude oscillation and internal circulation induced by departure from the nozzle or tip (A1, G4, Y3).

b. *Drops in Liquids* For drops in pure liquid systems, the area-free Sherwood number may be taken as the larger of the values calculated from the equations for solid spheres in Chapter 5 or Eq. (5-39) for fluid spheres. This provides a transition from the lines for solids in Fig. 7.14 to the potential flow line with increasing Re . For impure systems, surface-active materials may immobilize the drop surface and reduce the coefficients to those for solid particles. The area-free Sherwood number should be equal to or above that for a solid sphere, yet below that for a fluid sphere given by Eq. (5-39). If the system is grossly contaminated, oscillations occur if $Re > 200$.

c. *Bubbles in Water* Water is the only continuous fluid for which reliable mass transfer data are available at low M . Figure 7.15 presents the mass transfer factor $(kA/A_e)^{1/2}$ for bubbles in water including only data in which wall effects are small ($d_e/D < 0.12$) and for which the water had been degassed. Dissolved gases can transfer into the bubble and reduce the driving force appreciably (B13, L6, W5). The scatter in the figure is due to different methods of bubble release (Z2), different techniques of measuring the mass transfer rate (G1, W7), and different system purities (R1). Figure 7.15 also shows the mass transfer factor for a rigid spheroid with its aspect ratio given by Eq. (7-20), its velocity by the lower curve in Fig. 7.3, and its Sherwood number calculated from Eqs. (6-16) and (6-17) with $Sc = 500$. Predictions for potential flow from Eq. (7-46) are also shown, based on the properties of water at 25°C with terminal velocity from the upper curve in Fig. 7.3. Curve 1 corresponds to pure systems, with bubble shape from Fig. 7.9, while curve 2 corresponds to the shape in a contaminated system given by Eq. (7-20).

For $d_e > 0.5$ cm, the data agree closely with the potential flow solution with the shape appropriate to a contaminated system. For $d_e < 0.5$ cm, system purity

has a pronounced effect, just as on terminal velocity (see Fig. 7.3). In careful purified systems [e.g., (Z2)], the mass transfer coefficient increases sharply with decreasing d_e , but contaminated systems do not show such a sharp increase. With 1.2 ppm n-nananol added, the coefficient decreases towards the value for a rigid spheroid. Garner and Hammerton (G3) and Weiner (W4) apparent used systems of intermediate purity. Weiner also found that the mass transfer coefficient and terminal velocity decreased with bubble age due to accumulation of surfactants. The data for pure systems with $d_e < 0.5$ cm are better predicted by the potential flow solution with shape given by Fig. 7.9, but the predicted mass transfer factors increase less rapidly with decreasing bubble size than the data. The failure of the prediction results from zig-zag and helical motion in the range 0.2 cm $< d_e < 0.4$ cm (see Table 7.1).

A reasonable upper limit on the mass transfer factor from bubbles to well-purified water at room temperature is given by:

$$\frac{\bar{kA}/A_e}{Q^{1/2}} = \frac{0.14}{d_e^3} + \frac{6.94}{d_e^{1/4}}, \quad (7.50)$$

with d_e in cm and the left side in $s^{-1/2}$. For contaminated systems, the data for $d_e > 0.5$ cm are well represented by taking $(\bar{kA}/A_e)/Q^{1/2} = 6.5 s^{-1/2}$.

2. Particles with Shape Oscillations

When the shape of a particle oscillates, the surface area changes with time. This situation has been modeled by neglecting the motion adjacent to the surface due to the terminal velocity of the particle, i.e., by considering the particle to be oscillating but stationary, with material transferred by transient molecular diffusion over a time equal to the period of oscillation. For $Sc \gg 1$, the thin concentration boundary layer assumptions are invoked (see Chapter 1).

Two alternative assumptions have been made for the manner in which the area variation occurs. The more realistic postulates that all elements of the surface remain in the surface throughout an oscillation cycle. Increasing surface area stretches the surface (A3, B5) and causes a velocity normal to the surface which increases the diffusion rate. For a surface of area A_0 suddenly exposed at $t = 0$, the mass transfer product averaged over time is given by

$$\frac{\bar{kA}}{A_0} = 2 \sqrt{\frac{\mathcal{Q}}{\pi t}} \left[\int_0^t \left(\frac{A}{A_0} \right)^2 dt' \right]^{1/2}, \quad (7.51)$$

where the bracketed term represents the effect of the area variation. The value of \bar{kA} is proportional to the r.m.s. interfacial area, so that the transfer rate is larger when the area oscillates.

The alternate assumption is that new elements are brought to the surface as the area increases, and the oldest elements are removed from the surface when the area decreases (B16). For a surface of area A_0 exposed at $t = 0$, the time-averaged mass transfer product is then

$$\frac{\bar{kA}}{A_0} = 2 \sqrt{\frac{\mathcal{Q}}{\pi t}} + \sqrt{\frac{\mathcal{Q}}{\pi t}} \left[\int_0^t \left(\int_0^r \frac{1}{\sqrt{T-t'}} \frac{d(A/A_0)}{dt'} dr' \right) dT \right]. \quad (7.52)$$

The first term on the right-hand side represents transfer to the elements of surface present over the entire time period t , while the second represents transfer to appearing or disappearing elements. The fresh surface model, Eq. (7.52), predicts larger coefficients than the surface stretch model, Eq. (7.51). Given the time variation of the area of a fluid particle, the \bar{kA} product is easily calculated. For oscillating droplets, Angelo *et al.* (A3) showed that the time variation of area is given closely by:

$$A/A_0 = 1 + \varepsilon \sin^2(\pi t'), \quad (7.53)$$

where $1 + \varepsilon$ is the ratio of maximum area to minimum area, A_0 . Assuming that the averaging time is the period of oscillation, f^{-1} , and that the oscillation is spherical-oblate, we obtain from Eqs. (7.51) and (7.53) for the surface stretch model:

$$\text{Sh}_e = \frac{2}{\sqrt{\pi}} \sqrt{\frac{d_e^2 f}{\mathcal{Q}}} \sqrt{1 + \varepsilon + \frac{3\varepsilon^2}{8}}, \quad (7.54)$$

while from Eqs. (7.52) and (7.53) the fresh surface model yields

$$\text{Sh}_e = \frac{2}{\sqrt{\pi}} \sqrt{\frac{d_e^2 f}{\mathcal{Q}}} (1 + 0.687\varepsilon). \quad (7.55)$$

These results are remarkably close to each other; e.g., for an extreme value $\varepsilon = 0.5$ the fresh surface prediction is only 6% larger than the surface stretch model. The amplitude of the area oscillation, ε , has a relatively small effect on the prediction, since $\varepsilon \neq 0.3$ in many systems (R3, Y1).

Mass transfer data for oscillating liquid drops have been obtained in several studies in liquids (G2, G8, Y2) and a single study in gases (L5). Comparison with Eqs. (7.54) and (7.55) is difficult due to uncertainty in predicting the frequency f , and the lack of data on the amplitude factor ε . As noted earlier, the frequency of oscillation is generally less than the natural frequency given in Eq. (7.30). The following empirical equation applies to the liquid-liquid data with an average deviation of 6%:

$$\text{Sh}_e = 1.2 \sqrt{d_e^2 f / \mathcal{Q}} \quad \text{or} \quad \bar{kA}/A_e = 1.2 \sqrt{\mathcal{Q} f}. \quad (7.56)$$

Data for drops in gases show an average deviation of about 30% from Eq. (7.54).

D. INTERNAL RESISTANCE

For circulating fluid particles without shape oscillations the internal resistance varies with time in a way similar to that discussed in Chapter 5 for fluid spheres. The occurrence of oscillation, with associated internal circulation, always has a strong effect on the internal resistance. If the oscillations are sufficiently strong to promote vigorous internal mixing, the resistance with the particle becomes constant.

1. Particles without Shape Oscillations

Although there are no solutions for circulating ellipsoidal fluid particles similar to the Kronig-Brink model for spheres, Fig. 3.22, which includes the external resistance, should be a good approximation with $d = d_e$ and k taken to be the area-free external mass transfer coefficient. This procedure is supported by the work on freely suspended drops in gases by Garner and Laan (G4), who found that the Kronig-Brink model applied up to $Re \approx 3000$ after decay of strong initial circulation, caused during drop formation. Some of the

data are shown in Fig. 7.16. The ethylene glycol and monoethanolamine drops did not oscillate. The data from these experiments, in which there was a small external resistance, agree well with the curve for $Bi = 50$ from Fig. 3.22. Similar agreement with the Kronig-Brink model has been found for drops in liquids (B15, K1) as noted in Chapter 5. Although their data for nonoscillating drops in liquids were in fair agreement with the Kronig-Brink model, Skelland and Wellek (S7) proposed an empirical equation which is widely used. In impure systems, where surface-active materials make the particle effectively rigid, the drop may approach equilibrium at rates given by Fig. 3.21.

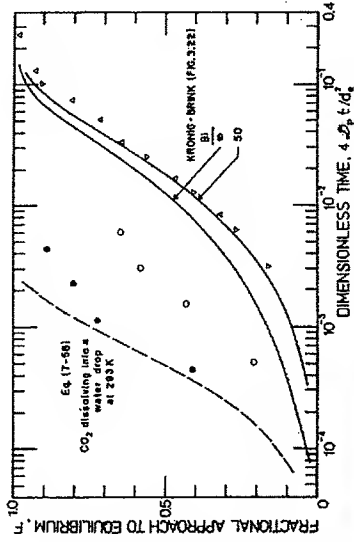


Fig. 7.16 Fractional approach to equilibrium for circulating and oscillating drops in gases.
Data of Garner and Lane (G4).

2. Particles with Shape Oscillations

If a fluid particle oscillates violently enough to mix its contents in each oscillation cycle, the average internal resistance is constant if the driving force is based upon the mixed mean concentration within the drop. The fractional approach to equilibrium is then given by Eq. (7-40) or (7-41).

A model of transfer within an oscillating droplet was proposed by Handlos and Baron (H3). They assumed that transfer within the drop was entirely by turbulent motion, random radial movement, superimposed upon toroidal circulation streamlines. No allowance was made for the variation of shape or

surface area. The results of the model are expressed in terms of a series solution for the fractional approach to equilibrium. For long times, only the first term is required, yielding a constant internal resistance:

$$k_p = 0.00375 U_f / (1 + \kappa). \quad (7-5)$$

Calculations valid for short times and including external resistance are available (P2). Equation (7-57) gives a rough estimate of $(kA)_p/A_e$ for organic-watt systems.

The assumption of transfer by a purely turbulent mechanism in the Handlos-Baron model leads to the prediction that the internal resistance is independent of molecular diffusivity. However, such independence has not been found experimentally, even for transfer in well-stirred cells or submerged turbulent jets (D4). In view of this fact and the neglect of shape and area oscillations, mode based upon the surface stretch or fresh surface mechanism appear more realistic. For rapid oscillations in systems with $Sc \gg 1$, mass transfer rates are described by identical equations on either side of the drop surface, so that the mass transfer results embodied in Eqs. (7-54) and (7-55) are valid for the internal resistance if \mathcal{Q} is replaced by \mathcal{Q}_p . Measurements of the internal resistance of oscillating drops show that the surface stretch model predicts the internal resistance with an average error of about 20% (B16, Y1). Agreement of the data for drops in liquids with Eq. (7-56) considerably improves if the constant is increased to 1.4, i.e.,

$$(kA)_p/A_e = 1.4\sqrt{f_N \mathcal{Q}_p}. \quad (7-5)$$

Figure 7.16 shows the fractional approach to equilibrium of an oscillating 5.8 mm water drop in a CO_2 -air mixture, predicted from Eqs. (7-41) and (7-55).

The large decrease in internal resistance with shape oscillation is readily apparent by comparison with the Kronig-Brink lines. The prediction is a good approximation of the rapid approach to equilibrium found by Garner and Lane (G4) for oscillating water droplets with negligible external resistance. Their data for dekalin are intermediate between the oscillating droplet prediction and the Kronig-Brink model, possibly because oscillation was not vigorous enough to mix the contents of the drop fully. Brunson and Wellek (B1) review other models for oscillating drops.

REFERENCES

- A1. Ahmadzadeh, J. and Harker, J. H., *Trans. Inst. Chem. Eng.* 52, 108-111 (1974).
- A2. Anderson, R. A., "Fundamentals of Vibrations," Macmillan, New York, 1967.
- A3. Angelo, J. B., Lightfoot, E. N. and Howard, D. W., *J. Ch. E. J.* 12, 751-760 (1966).
- A4. Aybers, N. M. and Tapscott, A., *Wärme-Stoffübertrag.* 2, 118-128 (1969).
- A5. Aybers, N. M. and Tapscott, A., *Wärme-Stoffübertrag.* 2, 171-177 (1969).
- B1. Bachhuber, C., and Sanford, C., *J. Appl. Phys.* 45, 2567-2569 (1974).
- B2. Baird, M. H. I., and Davidson, J. F., *Chem. Eng. Sci.* 17, 87-93 (1962).

- B3. Beard, K. V., *J. Atmos. Sci.* **33**, 851-864 (1976).
- B4. Beard, K. V., and Pruppacher, H. R., *J. Atmos. Sci.* **26**, 1066-1072 (1969).
- B5. Beek, W. J., and Kramers, H., *Chem. Eng. Sci.* **17**, 909-921 (1962).
- B6. Berghmans, J., *J. Chem. Eng. Sci.* **28**, 2005-2011 (1973).
- B7. Berry, E. X., and Pranger, M. R., *J. Appl. Meteorol.* **13**, 108-113 (1974).
- B8. Best, A. C., *Meteorol. Rev. Pap. No. 277* (1946); *No. 330* (1947).
- B9. Blanchard, D. C., "From Raindrops to Volcanoes," Doubleday, Garden City, New York, 1967.
- B10. Bonato, L. M., *Ternatec. Ric.* **20**, 11-18 (1971).
- B11. Braida, L., M.A.Sc. Thesis, Univ. of Toronto, 1956.
- B12. Brian, P. L. T., and Hales, H. B., *AIChE J.* **15**, 419-425 (1969).
- B13. Bridgewater, J., and McNab, G. S., *Chem. Eng. Sci.* **27**, 837-840 (1972).
- B14. Brignell, A. S., *Q. J. Mech. Appl. Math.* **26**, 99-107 (1973).
- B15. Brounshtein, B. I., Zheleznyak, A. S., and Fishbein, G. A., *Int. J. Heat Mass Transfer* **13**, 963-973 (1970).
- B16. Brunson, R. J., and Wellek, R. M., *Can. J. Chem. Eng.* **48**, 267-274 (1970).
- B17. Bryn, T., *David Taylor Model Basin Transl.* No 132 (1949).
- B18. Buzzard, J. F., and Nedderman, R. M., *Chem. Eng. Sci.* **22**, 1577-1586 (1967).
- C1. Calderbank, P. H., Johnson, D. S. L., and Loudon, J., *Chem. Eng. Sci.* **25**, 235-256 (1970).
- C2. Connole, R., *C. R. Acad. Sci. Ser. A* **272**, 1213-1216 (1971).
- D1. Datta, R. L., Napier, D. H., and Newitt, D. M., *Trans. Inst. Chem. Eng.* **28**, 14-26 (1950).
- D2. Davenport, W. G., Ph.D. Thesis, Imperial College, London, 1964.
- D3. Davenport, W. G., Richardson, F. D., and Bradshaw, A. V., *Chem. Eng. Sci.* **22**, 1221-1235 (1967).
- D4. Davies, J. T., "Turbulence Phenomena," Academic Press, New York, 1972.
- D5. Davies, R. M., and Taylor, Sir G. J., *Proc. Roy. Soc. Ser. A* **200**, 375-390 (1950).
- E1. Edge, R. M., Flatman, A. T., Grant, C. D., and Kalafatoglu, I. E., *Symp. Multiphase Flow Syst.. Inst. Chem. Eng. London Pap.* C3 (1974).
- E2. Edge, R. M., and Grant, C. D., *Chem. Eng. Sci.* **26**, 1001-1012 (1971).
- E3. Edge, R. M., and Grant, C. D., *Chem. Eng. Sci.* **27**, 1709-1721 (1972).
- E4. Elzinga, E. R., and Banchero, J. T., *AIChE J.* **7**, 394-399 (1961).
- F1. Fluijy, B. A., Ph.D. Thesis, Univ. of Birmingham, 1957.
- F2. Foote, G. B., *J. Atmos. Sci.* **26**, 179-184 (1969).
- G1. Garbarini, G. R., and Tien, C., *Can. J. Chem. Eng.* **47**, 35-41 (1969).
- G2. Garner, F. H., Foord, A., and Tayeban, M., *J. Appl. Chem.* **9**, 315-323 (1959).
- G3. Garner, F. H., and Hammerton, D., *Trans. Inst. Chem. Eng.* **32**, 518-524 (1954).
- G4. Garner, F. H., and Lane, J. J., *Trans. Inst. Chem. Eng.* **37**, 162-172 (1959).
- G5. Garner, F. H., and Lihou, D. A., *DECHEMA Monogr.* **55**, 155-178 (1965).
- G6. Garner, F. H., and Sheland, A. H. P., *Chem. Eng. Sci.* **4**, 149-158 (1955).
- G7. Garner, F. H., and Skelland, A. H. P., *Ind. Eng. Chem.* **48**, 51-58 (1956).
- G8. Garner, F. H., and Tayeban, M., *An. fis. Quim.* **LVI-B**, 479-498 (1960).
- G9. Gaudin, A. M., "Floation," 2nd ed. McGraw-Hill, New York, 1957.
- G10. Gibbons, J. H., Houghton, G., and Coull, J., *AIChE J.* **8**, 274-276 (1962).
- G11. Gorodetskaya, A., *Zh. fiz. Khim.* **23**, 71-77 (1949).
- G12. Grace, J. R., Wairegi, T., and Nguyen, T. H., *Trans. Inst. Chem. Eng.* **54**, 167-173 (1976).
- G13. Gunn, R., and Kinzer, G. D., *J. Meteorol.* **6**, 243-248 (1949).
- G14. Guthrie, R. I. L., Ph.D. Thesis, Imperial College, London, 1967.
- G15. Guthrie, R. I. L., and Bradshaw, A. V., *Chem. Eng. Sci.* **28**, 191-203 (1973).
- H1. Haberman, W. L., and Morton, R. K., *David Taylor Model Basin Rep. No. 802* (1953).
- H2. Hamielec, A. E., Ph.D. Thesis, Univ. of Toronto, 1961.
- H3. Handlos, A. E., and Baroni, T., *AIChE J.* **3**, 127-136 (1957).
- H4. Harper, J. F., *Chem. Eng. Sci.* **25**, 342-343 (1970).
- H5. Harper, J. F., *Adv. Appl. Mech.* **12**, 59-129 (1972).
- H6. Hartunian, R. A., and Sears, W. R., *J. Fluid Mech.* **3**, 27-47 (1957).
- H7. Hayashi, S., and Matunobu, Y., *J. Phys. Soc. Jpn.* **22**, 905-910 (1967).
- H8. Hendrik, C. D., Dave, S. B., and Johnson, H. F., *AIChE J.* **13**, 1072-1077 (1967).
- H9. Horton, T. J., Fritsch, T. R., and Kinzer, R. C., *Can. J. Chem. Eng.* **43**, 143-146 (1965).
- H10. Houghton, G., Ritchie, P. D., and Thomson, J. A., *Chem. Eng. Sci.* **7**, 111-112 (1955).
- H11. Hozawa, M., Tadaki, T., and Maeda, S., *Kagaku Kogyaku* **34**, 315-320 (1970).
- H12. Hu, S., and Kinzer, R. C., *AIChE J.* **1**, 42-50 (1955).
- J1. Johnson, A. I., Besik, F., and Hamielec, A. E., *Can. J. Chem. Eng.* **47**, 559-564 (1969).
- J2. Johnson, A. I., and Braida, L., *Can. J. Chem. Eng.* **35**, 165-172 (1957).
- J3. Jones, D. M., *J. Meteorol.* **16**, 504-510 (1959).
- J4. Jones, D. R. M., Ph.D. Thesis, Cambridge Univ., 1965.
- K1. Kadenskaya, N. I., Zheleznyak, A. S., and Brounshtein, B. I., *Zh. Prikl. Khim. (Leningrad)* **38**, 1156-1159 (1965).
- K2. Keift, F. W., and Hisson, A. N., *Ind. Eng. Chem.* **47**, 256-267 (1955).
- K3. Klee, A. J., and Trebilcot, R. E., *AIChE J.* **2**, 444-447 (1956).
- K4. Kojima, E., Akehata, T., and Shiraishi, T., *J. Chem. Eng. Jpn.* **1**, 45-50 (1968).
- K5. Krishna, P. M., Venkateswarlu, D., and Narasimhamurty, G. S. R., *J. Chem. Eng. Dyn.* **4**, 336-343 (1959).
- L1. Lamb, H., "Hydrodynamics," 6th ed. Cambridge Univ. Press, London, 1932.
- L2. Lessard, R. R., and Ziemiński, S. A., *Ind. Eng. Chem., Fundam.* **10**, 260-269 (1971).
- L3. Light, W., and Narasimhamurty, G. S. R., *AIChE J.* **1**, 366-373 (1955).
- L4. Lihou, D. A., *Trans. Inst. Chem. Eng.* **50**, 392-393 (1972).
- L5. Lihou, D. A., Lowe, W. D., and Hattangady, K. S., *Trans. Inst. Chem. Eng.* **50**, 217-222 (1972).
- L6. Lindt, J. T., Dissertation, Technische Hogeschool, Delft. (Brondor—Offset N. V., Rotterdam, 1971.)
- L7. Lindt, J. T., *Chem. Eng. Sci.* **27**, 1775-1781 (1972).
- L8. Lindt, J. T., and De Groot, R. G., *Chem. Eng. Sci.* **29**, 957-962 (1974).
- L9. List, R., and Hand, M. J., *Phys. Fluids* **14**, 1648-1655 (1971).
- L10. Lochiel, A. C., and Calderbank, P. H., *Chem. Eng. Sci.* **19**, 471-484 (1964).
- L11. Loutay, R., and Vigues, A., *Chem. Eng. Sci.* **25**, 201-217 (1970).
- M1. Magarvey, R. H., and Bishop, R. L., *Phys. Fluids* **4**, 800-805 (1961).
- M2. Magarvey, R. H., and Bishop, R. L., *Can. J. Phys.* **39**, 1418-1422 (1961).
- M3. Magarvey, R. H., and Blackford, B. L., *Can. J. Phys.* **40**, 1036-1040 (1962).
- M4. Magono, C., *J. Meteorol.* **11**, 77-79 (1954).
- M5. Marrucci, G., Apuzzo, G., and Astaria, G., *AIChE J.* **16**, 538-541 (1970).
- M6. McDonald, J. E., *J. Meteorol.* **11**, 478-494 (1954).
- M7. Mendelson, H. D., *AIChE J.* **13**, 250-252 (1967).
- M8. Mercier, J., and Antia, W., *Houille Blanche* No. 5, 421-425 (1972).
- M9. Mercier, J., and Rocha, A., *Chem. Eng. Sci.* **24**, 1179-1183 (1969).
- M10. Miller, C. A., and Scriven, L. E., *J. Fluid Mech.* **32**, 417-435 (1968).
- M11. Moore, D. W., *J. Fluid Mech.* **23**, 749-766 (1965).
- M12. Moore, F. K., *NASA Contract. Rep. NASA CR-1368* (1972).
- N1. Napier, D. H., Newitt, D. M., and Datta, R. L., *Trans. Inst. Chem. Eng.* **28**, 14-31 (1950).
- N2. Natarajan, R., *Combust. Flame* **20**, 199-209 (1973).
- P1. Pan, F. Y., and Arivoss, A., *Ind. Eng. Chem., Fundam.* **7**, 227-232 (1968).
- P2. Patel, J. M., and Walek, R. M., *AIChE J.* **13**, 384-386 (1967).
- P3. Peebles, F. N., and Garber, H. J., *Chem. Eng. Prog.* **49**(2), 88-97 (1953).
- P4. Pittet, R. L., and Pruppacher, H. R., *Q. J. R. Meteorol. Soc.* **99**, 540-550 (1973).
- P5. Pruppacher, H. R., and Beard, K. V., *Q. J. R. Meteorol. Soc.* **96**, 247-256 (1970).

- R1. Raymond, D. R., and Zieminski, S. A., *AIChE J.* **17**, 57-65 (1971).
 R2. Reinhart, A., *Chem.-Ing.-Tech.* **36**, 740-746 (1964).
 R3. Rose, P. M., Ph.D. Thesis, Illinois Inst. of Technol., Chicago, 1965.
 R4. Rose, P. M., and Kintner, R. C., *AIChE J.* **12**, 530-534 (1966).
 R5. Rosenberg, B., *David Taylor Model Basin Rep.* No. 727 (1950).
 R6. Ryan, R. T., *J. Appl. Meteorol.* **15**, 157-165 (1976).
 S1. Saftman, P. G., *J. Fluid Mech.* **1**, 249-275 (1956).
 S2. Satapathy, R., and Smith, W. J., *Fluid Mech.* **10**, 561-570 (1961).
 S3. Savic, P., *Natl. Res. Coun. Can. Rep.* No. MT-22 (1953).
 S4. Schroeder, R. R., Ph.D. Thesis, Illinois Inst. of Technol., Chicago, 1964.
 S5. Schroeder, R. R., and Kintner, R. C., *AIChE J.* **11**, 5-8 (1965).
 S6. Skelland, A. H. P., and Caenepel, C. L., *AIChE J.* **18**, 1154-1163 (1972).
 S7. Skelland, A. H. P., and Wellek, R. M., *AIChE J.* **10**, 491-496 (1964).
 S8. Srikrishna, M., and Narasimhamurty, G. S. R., *Indian Chem. Eng.* **13**, 4-11 (1971).
 S9. Stuke, B., *Naturwissenschaften* **39**, 325-336 (1952).
 S10. Subramanyam, S. V., *J. Fluid Mech.* **37**, 715-725 (1969).
 S11. Sunner, B. S., and Moore, F. K., *NASA Contract. Rep.* NASA CR-1669 (1970).
 T1. Tadaki, T., and Maeda, S., *Kagaku Kagaku* **25**, 254-264 (1961).
 T2. Tapucu, A., Document IGN-87, Ecole Polytechnique, Montreal, 1974.
 T3. Taylor, J. D., and Acivos, A. J., *J. Fluid Mech.* **18**, 466-476 (1964).
 T4. Thorsen, G., Stordalen, R. M., and Terjesen, S. G., *Chem. Eng. Sci.* **23**, 413-426 (1968).
 T5. Thorsen, G., and Terjesen, S. G., *Chem. Eng. Sci.* **17**, 137-148 (1962).
 T6. Tsuge, H., and Hibino, S., *Kagaku Kagaku* **35**, 65-71 (1971).
 V1. Vakhrushev, I. A., and Efremov, G. I., *Chem. Technol. Fuels Oils (USSR)* **5**, 376-379 (1970).
 V2. Van der Leeden, P., Nio, L. D., and Suratman, P. C., *Appl. Sci. Res., Sect. A* **5**, 338-348 (1956).
 V3. Vogtländer, J. G., and Meijboom, F. W., *Chem. Eng. Sci.* **29**, 799-803 (1974).
 W1. Waiteg, T., Ph.D. Thesis, McGill Univ., Montreal, 1974.
 W2. Wallis, G. B., *Int. J. Multiphase Flow* **1**, 491-511 (1974).
 W3. Warschay, M., Bogusz, E., Johnson, M., and Kinner, R. C., *Can. J. Chem. Eng.* **37**, 29-36 (1959).
 W4. Weiner, A., Ph.D. Thesis, Univ. of Pennsylvania, Philadelphia, 1974.
 W5. Wellek, R. M., Andoe, W. V., and Brunson, R. J., *Can. J. Chem. Eng.* **48**, 645-655 (1970).
 W6. Wellek, R. M., Agrawal, A. K., and Skelland, A. H. P., *AIChE J.* **12**, 854-862 (1966).
 W7. Weller, K. R., *Can. J. Chem. Eng.* **50**, 49-58 (1972).
 W8. Winnikow, S., and Chao, B. T., *Phys. Fluids* **9**, 50-61 (1966).
 Y1. Yamaguchi, M., Fujimoto, T., and Katayama, T., *J. Chem. Eng. Jpn.* **8**, 361-366 (1975).
 Y2. Yamaguchi, M., Watanabe, S., and Katayama, T., *J. Chem. Eng. Jpn.* **8**, 415-417 (1975).
 Y3. Yao, S.-C., and Schrock, V. E., *J. Heat Transfer* **98**, 120-125 (1976).
 Y4. Yeheskel, J., and Kehat, E., *Chem. Eng. Sci.* **26**, 1223-1233 (1971).
 Z1. Zabel, T., Hanson, C., and Ingham, J., *Trans. Inst. Chem. Eng.* **51**, 162-164 (1973).
 Z2. Zieminski, S. A., and Raymond, D. R., *Chem. Eng. Sci.* **23**, 17-28 (1968).

Chapter 8

Deformed Fluid Particles of Large Size

I. INTRODUCTION

This chapter is devoted to bubbles and drops with $Eo > 40$ and $Re > 1$. (see Chapter 2). These inequalities are generally satisfied by bubbles and drop with volumes greater than about 3 cm^3 (i.e., $d_e > 1.8 \text{ cm}$). Considerable work has been carried out for large gas bubbles, primarily in connection with underwater explosions, fluidized beds, and processing of liquid metals, and review have been prepared by Wegener and Parlane (W5) and Harper (H2). Relative little attention has been devoted to large drops. Drops falling in gases almost always break up before an Eotvos number of 40 is reached (see Chapter 1), so that the present chapter is restricted to cases where the continuous phase is a liquid.

In the present chapter, we neglect wall effects and unsteady motion including splitting. These factors are considered in Chapters 9, 11, and 12, respectively. The fluid mechanics of large bubbles and drops are discussed before their mass transfer.

II. FLUID MECHANICS

A. SHAPE

Over most of the range covered by this chapter, the shape of bubbles and drops can be closely approximated as a segment of a sphere (see Fig. 2.) Hence, most of the fluid particles under discussion are said to be "spherical caps." For $Re \geq 150$, the rear or base is quite flat, though sometimes irregular, and the wake angle very nearly 50° . At lower Re , the wake angle is larger (G^{*} as shown in Fig. 8.1. For $Re < 40$, the leading edge tends to be oblate ellipsoid

IN THE UNITED STATES PATENT AND TRADEMARK OFFICE

In re application of: Ronald D. BLUM, ET
AL.

Application No.: 09/994,860

Filed: November 28, 2001

For: METHOD AND APPARATUS FOR
REDUCING THE INTENSITY OF
HURRICANES AT SEA BY DEEP-
WATER UPWELLING

Customer No.: 20350

Confirmation No. 9812

Examiner: Boeckmann, Jason

Technology Center/Art Unit: 3752

Mail Stop AF
Commissioner for Patents
P.O. Box 1450
Alexandria, VA 22313-1450

DECLARATION UNDER 37 C.F.R. § 1.132

I, Isaac Ginis Ph.D., declare the following:

1. I am a tenured Professor of Oceanography at the University of Rhode Island. I hold a doctorate in Geophysics, specializing in Oceanography and Meteorology. A copy of my resume is attached as Exhibit A.

2. I am a leading expert in numerical modeling and forecasting of air-sea interaction during hurricanes. I have published over 70 papers in scientific journals and books on this topic and authored a chapter on hurricane-ocean interaction for the book "Global Perspectives on Tropical Cyclones" published by the World Meteorological Organization, Geneva, Switzerland in 1995. I have delivered over 100 lectures worldwide at national and international meetings as well as at oceanographic and atmospheric institutions and have advised 12 doctoral students and

postdoctoral scientists. The National Science Foundation, the National Oceanic and Atmospheric Administration, the U.S. Office of Naval Research supported my research.

3. I have been leading the effort toward improvements of the GFDL/URI coupled hurricane model related to the ocean and wave coupling. This work involves close collaboration between my research group at URI and scientists at the NOAA's National Centers for Environmental Prediction (NCEP) and Geophysical Fluid Dynamics Laboratory (GFDL). My research group has made a successful conversion of a research coupled hurricane-ocean research model to a fully automated real-time prediction system. This significant technological and computer programming effort has resulted in implementation of the GFDL/URI coupled hurricane model to operational forecasting at National Weather Service in 2001. This model is used by the National Hurricane Center for issuing official hurricane warnings. I continue to be responsible for maintaining and improving the coupled hurricane operational forecast system at NCEP.

4. I have been retained by the assignee of the above-identified application to assist in responding to the Office Action. I have no financial interest in the assignee or the outcome of this patent application, including whether it issues as a patent or not. I am being compensated for the time spent on this matter at the rate of \$200/hr, plus reasonable expenses.

5. I have read and am familiar with the above-referenced application. I have also read and am familiar with the Office Action mailed May 4, 2007 ("Office Action") pertaining to this application.

6. It is my understanding that the claims currently under examination, which relate to, *inter alia*, methodologies for reducing the intensity of a hurricane, were rejected as allegedly being wholly inoperative, lacking credible utility, and not enabled. Specifically, the Examiner asserts:

...applicant admits in his arguments, "submersibles of the kind required for this application do not presently exist." It seems that applicant wishes that someone will come along and develop the technology required to make the required submersibles, thereby enabling the present invention. Therefore, it is impossible for one

of ordinary skill in the art at his time to make and or use this invention. Office Action at page 6.

7. The disclosure contains sufficient evidence and reasoning that a person of skill in the art would appreciate that since a hurricane draws energy from the heat content of the upper ocean, it is generally accepted that a large area of cooled ocean surface can suppress hurricane intensity. For example, the specification states:

[0005] Because tropical storms draw their energy from the heat content of the upper ocean, it is generally accepted that a large area of cooled ocean surface can suppress hurricane intensity. Numerical modeling studies at the Massachusetts Institute of Technology suggests that reduction of sea surface temperature by 2.5°C in the storm's central core would eliminate the thermodynamic conditions that sustain hurricanes. Other numerical model studies by independent researchers corroborate these results. In addition, analyses of measurements from past hurricanes show a strong correlation between lack of hurricane intensification and conditions that favor cold-water upwelling by the storm's own winds, such as a shallow thermocline or slow forward speed. Finally, there is clear evidence that hurricanes weaken (or do not intensify under otherwise favorable conditions) when a hurricane crosses the cold "wake" of a previous storm.

I agree with this assertion in the specification, which is consistent with the knowledge of one skilled in the art at the time of filing the application. Indeed, as detailed below, I conducted numeric modeling that illustrates that reduction of the temperature in the storm's central core would reduce the wind speed of the hurricane, and hence the intensity of the hurricane.

8. Variability in hurricane intensity originates from two sources: internal variability and environmental interactions. An important aspect of environmental interaction is the coupling between the storm and the underlying ocean. It is well known that tropical cyclones are driven by turbulent heat fluxes from the ocean (Ooyama, 1969) and it is natural to suppose that variability in surface conditions and in the response of the upper ocean to the passing storm plays a role in controlling storm intensity.

9. The effect of air-sea interaction as a negative feedback on tropical cyclone development and intensity has been well established. It is known that strong surface winds in a tropical cyclone induce turbulent mixing in the upper ocean and entrainment of the underlying cold water into the ocean mixed layer, which cools and deepens (e.g., Price 1981, Bender et al. 1993, Ginis 2002). Both observational and real case numerical studies (e.g., Black, 1983; Bender and Ginis 2000) showed that the SST anomalies induced by tropical cyclones can reach up to 5-6°C. Studies also showed that tropical cyclone intensity is more sensitive to the local SST changes under the hurricane core than to those beyond the core area (e.g., Emanuel, 1999; Shen et al., 2000). Therefore, it can be expected that cooling of the ocean area underneath the hurricane core may reduce its intensity.

10. Numerical modeling studies suggest that a reduction of sea surface temperatures by 2.5° C in the storm's central core would eliminate the conditions that sustain hurricanes (Emanuel, 1986, 1988). Numerical simulations with coupled models (Khain and Ginis, 1991, Bender et al., 1993) and the operational GFDL/URI coupled hurricane-ocean model forecasts (Bender et al., 2007) indicate that *most* tropical cyclones experience a noticeable reduction of intensity owing to their coupling with the ocean, though the degree of reduction depends on many aspects of the upper ocean thermal structure and the speed of translation, size and initial intensity of the tropical cyclone. This coupling also depends on the surface heat and momentum exchange, which affects mean currents and turbulence in the ocean mixed layer and thereby influences the degree of mixing through the seasonal thermocline.

11. For this declaration, I have conducted a set of numerical experiments to assess the impact on hurricane intensity of a region with the reduced upper ocean heat content (hereafter "cooled" region) placed in front of a moving hurricane. I used the NOAA operational GFDL/URI coupled hurricane-ocean model (Bender et al. 2007) with idealized, but realistic, oceanic and atmospheric conditions. The GFDL hurricane prediction system became operational in 1995 as the U.S. National Weather Service's official hurricane model. Since that time, it has provided forecast guidance to forecasters at the NWS's Tropical Prediction Center (TPC) and has been the most

reliable forecast model for track error during the past decade (Table 1, courtesy of James Franklin, TPC). Table 1 is attached as Exhibit B.

12. Important upgrades to the physics and spatial and vertical resolutions have been introduced to the GFDL/URI model over the years. These upgrades led to significant increase in GFDL/URI model intensity forecast skill (Bender et al, 2007). The operational GFDL/URI model presently has about 9 km spatial resolution in the innermost movable mesh. For this study, I increased the finest resolution to about 4.5 km to improve further its intensity forecast skill.

13. For these idealized experiments, I integrated the coupled model for 120 hours starting with a normal size initial hurricane vortex embedded in specified initial, horizontally uniform environmental conditions. A GATE (Global Atlantic Tropical Experiment) III condition in the tropics is used for the atmospheric environmental thermal profile, which has air temperature of 27°C and relative humidity of 84% at the lowest model level (about 35 m). A steady easterly environmental wind of 5 m/s was used (the hurricane is moving north-west). In the control experiment, the ocean was initially horizontally uniform and motionless with the sea surface temperature of 28.5°C. The initial vertical temperature profile with a mixed layer depth of 30 m is typical for the northern Gulf of Mexico in September.

14. Simulation of the SST response in the control experiment is shown in Figure 1, attached as Exhibit C. A typical SST cooling pattern is generated due to hurricane-ocean interaction. The largest cooling is on the right sight of the hurricane track, consistent with observations and other modeling studies (Ginis, 2002).

15. In the first two sensitivity experiments, I introduced the cooled regions in front of the moving hurricane as shown in Figure 2, attached as Exhibit D. The size of each region is about 400 km in the along-track direction and covered the entire computational domain in the cross-track direction. The temperature anomalies in the regions are 1°C and 2°C, correspondingly, which are evenly distributed over the depth of the mixed layer.

16. The main results are summarized in Figures 3 and 4 (Figure 3 is attached as Exhibit E and Figure 4 is attached as Exhibit F). The temperature anomalies (SSTA) underneath the hurricane core, defined as a circular area around the storm center with $R=100$ km, are shown in Figure 3. The SSTA are greatly reduced when the hurricane crosses the cooled regions. Evolution of hurricane central pressure and maximum winds in the numerical experiments are shown in Figure 4. In both sensitivity experiments the hurricane intensity was reduced after the storm encounters the cooled regions. The maximum winds were reduced from about 145 kts to about 135 kts (6% reduction) in the 1°C swath experiment and to about 130 kts (10% reduction) in the 2°C swath experiment.

17. I conducted an additional experiment in which the size of the 2°C cooled region was doubled along the track direction. As result, the hurricane intensity was further reduced from about 145 kts to about 120 kts (22% reduction). These sensitivity experiments clearly indicate that both the size and magnitude of the cooled area encountered by a moving hurricane make important impact on the hurricane intensity reduction.

18. A list of references cited herein are attached as Exhibit G.

19. All statements made herein of my own knowledge are true and that all statements made on information and belief are believed to be true; and further, that the statements were made with the knowledge that willful false statements and the like so made are punishable by fine or imprisonment, or both, under section 1001 of Title 18 of the United States Code, and such willful false statements may jeopardize the validity of the application or any patents issuing thereon.



Isaac Ginis, Ph.D.

Date 11.05.07

Exhibit A

Curriculum Vita

ISAAC GINIS

Professor of Oceanography
Graduate School of Oceanography
University of Rhode Island
Narragansett, RI 02882
Tel: (401) 874-6484; Fax: (401) 874-6728
e-mail: iginis@gso.uri.edu
WWW: www.po.gso.uri.edu/Numerical/ig

Professional Preparation:

Kabardino-Balkarian State University, Nalchik, Russia	Mathematics	M.S.	1977
Institute of Experimental Meteorology, Obninsk, Russia	Geophysics	Ph.D.	1986

Appointments:

2003-present	Professor of Oceanography, University of Rhode Island
2006 - Fall	Visiting Research Scholar, Princeton University, Princeton, NJ
1998-2003	Associate Professor of Oceanography, University of Rhode Island
1993-1998	Associate Marine Research Scientist, Adjunct Professor of Oceanography University of Rhode Island
1990-1993	Visiting Research Scientist, Geophysical Fluid Dynamics Laboratory/NOAA Princeton University, Princeton, NJ
1977-1989	Research Scientist, Institute of Mechanics and Applied Mathematics, Kabardino-Balkarian State University, Nalchik, Russia

Awards

- National Oceanic and Atmospheric Administration 2001 Outstanding Scientific Paper Award
- National Science Foundation Atmospheric Sciences Division 2001 Highlighted Research Project
- National Oceanic and Atmospheric Administration 2002 Environmental Hero Award
- National Oceanographic Partnership Program 2002 Excellence in Partnering Award

Journal Publications (last 3 years)

- Bender, M.A., I. Ginis, R. Tuleya, B. Thomas, T. Marchok, 2007: The operational GFDL coupled hurricane-ocean prediction system and a summary of its performance. *Mon. Wea. Rev.* In press.
- Moon, I., I. Ginis, and T. Hara, B. Thomas, 2007: Physics-based parameterization of air-sea momentum flux at high wind speeds and its impact on hurricane intensity predictions. *Mon. Wea. Rev.* **135**, 2869-2878.
- Moon, I., I. Ginis, and T. Hara, 2007: Impact of reduced drag coefficient on ocean wave modeling under hurricane conditions, *Mon. Wea. Rev.* In press.
- Yablonsky, R. M., I. Ginis, 2007: Improving the initialization of coupled hurricane-ocean models by assimilating mesoscale oceanic features. *Mon. Wea. Rev.* In press.
- Fan Y., I. Ginis, T. Hara, Il Ju Moon, 2007: Energy and momentum budget across air-sea interface. Part I: Steady Uniform Wind, *J. of Atmos. Sci.* Submitted.
- Fan Y., I. Ginis, T. Hara, Il Ju Moon, 2007: Energy and momentum budget across air-sea interface. Part II: Hurricane Wind, *J. of Atmos. Sci.* Submitted.

- Falkovich, A., and **I. Ginis**, 2005: Ocean data assimilation and initialization procedure for the Coupled GFDL/URI Hurricane Prediction System. *J. Atmos. Oceanic Technol.*, **22**, 1918–1932.
- Ginis, I.**, A.P. Khain, E. Morozovsky, 2004: Effects of large eddies on the structure of the marine boundary layer under strong wind conditions, *J. Atmos. Sci.*, **61**, 3049–3064.
- Moon, I.-J., **I. Ginis**, and T. Hara, 2004: Effect of surface waves on air-sea momentum exchange. Part II: Behavior of drag coefficient under tropical cyclones, *J. Atmos. Sci.*, **61**, 2334–2348.
- Moon I.J., **I. Ginis**, T. Hara, E. J. Walsh, and H. L. Tolman, 2003: Numerical modeling of sea surface directional wave spectra under hurricane wind forcing, *J. Phys. Oceanogr.*, **33**, 1680–1706.
- Frolov, S.A., Sutyrin, G.G., and **I. Ginis**, 2004: Asymmetry of the stabilized Gulf Stream system. *J. Phys Oceanogr.*, **34**, 1087–1102.
- Knutson, T.R., R.E. Tuleya, **I. Ginis**, 2004: Impact of climate change on hurricane intensity as simulated using regional high-resolution models. Book Chapter. Columbia University Press.

Synergistic Activities

I've been leading the effort toward improvements of the GFDL/URI coupled hurricane model related to the ocean and wave coupling. This work involves close collaboration between my research group at URI and scientists at the NOAA's National Centers for Environmental Prediction (NCEP) and Geophysical Fluid Dynamics Laboratory (GFDL). My research group has made a successful conversion of a research coupled hurricane-ocean research model to a fully automated real-time prediction system. This significant technological and computer programming effort has resulted in implementation of the GFDL/URI coupled hurricane model to operational forecasting at National Weather Service in 2001. This model is used by the National Hurricane Center for issuing official hurricane warnings. We continue to be responsible for maintaining and improving the coupled hurricane operational forecast system at NCEP. A number of major improvements have been made to the operation model for the 2002-06 hurricane seasons which led to significant improvements of the GFDL model forecast skill. Through ongoing collaboration with GFDL, Navy's Fleet Numerical Meteorology Center (FNMOC) and Joint Typhoon Warning Center (JTWC) we are transitioning the new version of the GFDL/URI hurricane model to operations at FNMOC for global tropical cyclone forecasting. Since 2006 my research group has been actively involved in developing the new generation Hurricane Weather, Research and Forecast (HWRF) model in collaboration with EMC/NCEP scientists. We focus our effort on developing and improving the ocean and wave components of the coupled HWRF system. We also collaborate with scientists at the Korean Oceanography and Development Institute in developing a coupled tropical cyclone-ocean model for the western Pacific.

I have developed new courses at URI that cover various numerical methods applied for solving the fundamental equations governing atmospheric and oceanic motions, marine geophysics, and biophysics.

Research Collaborators within Last 48 Months

M. Bender, R. Tuleya, T. Marchok (GFDL/NOAA), A. Khain (HIUJ), G. Sutyrin, L. Rothstein, T. Hara (URI), Il-Ju Moon (JU, Korea), H. Tolman, N. Surgi, C. Lozano (NCEP/NOAA), E. Walsh (NOAA/ETL and NASA/GSFC), K. Emanuel (MIT), Sok Kuh Kang (KORDI).

Graduate Students and Postdoctoral Fellows Advised/Sponsored

Sergey Frolov (PhD), Evan Robertson (MS), Minoru Kadota (MS), Yalin Fan (PhD), Dr. Clark Rowley, Dr. Weixing Shen, Dr. Ray Richardson, Dr. Il-Ju Moon, Richard Yablonsky(PhD - present), Zhitao Yu (PhD- present), Erica Clay (PhD- present), Seunghoun Lee (PhD – present), Lou Licate (MS – present), Dr. Biju Thomas (present), Dr. Yalin Fan (present).

Exhibit B

VERIFYING TIME	NUMBER OF CASES	GFDI	GFSI	UKMI	NGPI
00	2252	8.8	8.	8.	8.
12	2128	38.8	42.8	44.9	43.3
24	1952	67.1	73.7	77.7	74.2
36	1741	98.9	104.4	108.8	105.4
48	1511	122.8	135.2	136.7	137.4
72	1159	192.4	208.0	195.0	206.1

TABLE 1 Average track errors in nautical miles [nm] for all forecasts run in the Atlantic between 1996 and 2005 for the GFDL, NCEP's GFS, UKMET and Navy's NOGAPS models. Results are for the time interpolated models. Since numerical weather prediction models are generally not available to the forecasters in time to make their forecasts, a simple technique exists to take the model forecasted position and intensity, and adjust the forecast to apply to the current synoptic time and initial conditions. This adjustment is usually 6 or 12 hours, depending on the availability of the last model guidance. These adjusted versions are known for historical reasons as interpolated models which are generally indicated by the letter "I" at the end of the name (e.g., GFDI for the GFDL interpolated model).

Exhibit C

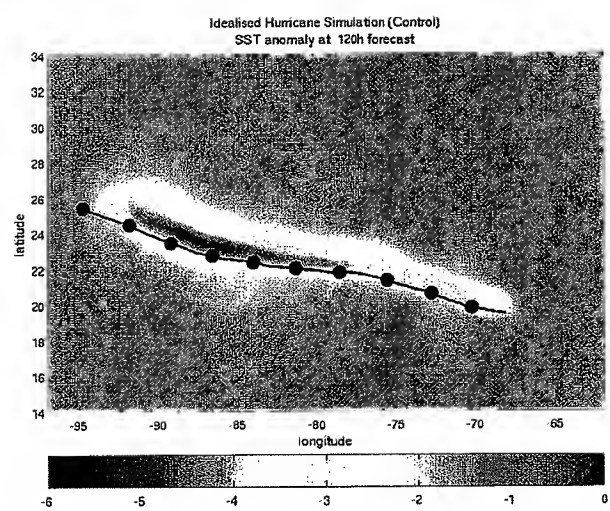


Figure 1. SST anomalies at 120 h in the control experiment.

Exhibit D

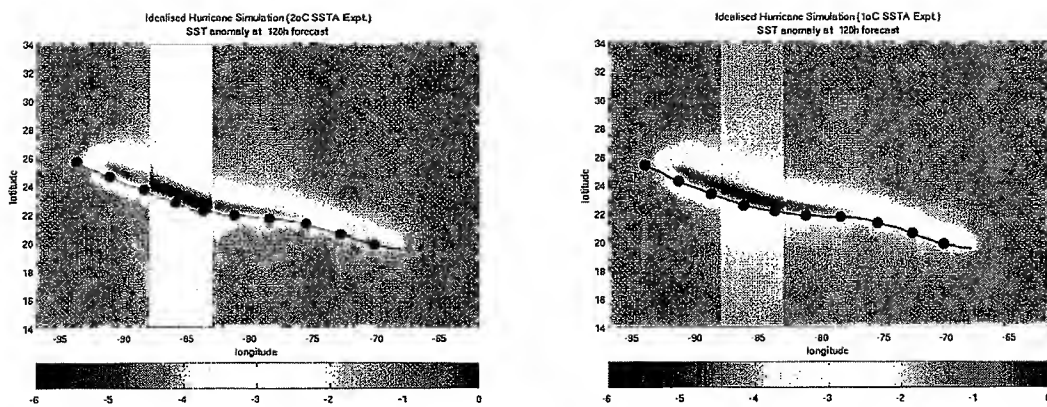


Figure 2. SST anomalies at 120 h in two sensitivity experiments, where cooled regions of 1°C (left panel) and 2°C (right panel) temperature anomalies are placed in front of the hurricane.

Exhibit E

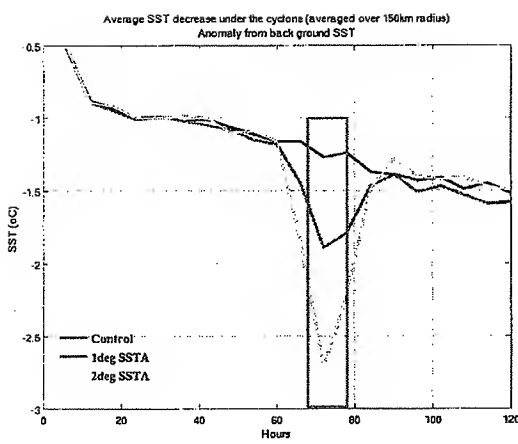


Figure 3. SST anomalies (SSTA) underneath the hurricane core region, defined as a circular area around the storm center with $R=100$ km, as function of time. The rectangular box indicates the time when the hurricane center crossed the region with the reduced upper ocean heat content.

Exhibit F

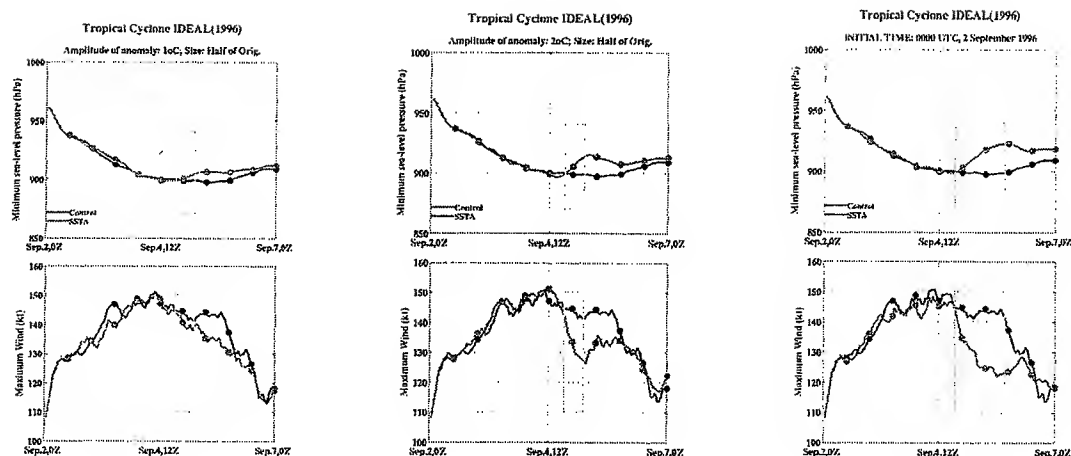


Figure 4. Evolution of central pressure and maximum winds in four numerical experiments: 1) control (blue line), 2) 1°C anomaly (left panel, red), 3) 2°C anomaly (middle panel, red,) and 4) the same as 1) and 2) except the size of the cooled swath in the along track direction is twice larger. The green rectangular boxes indicate the time when the hurricane center crossed the regions with the reduced upper ocean heat content.

Exhibit G

REFERENCES

- Bender, M. A., and I. Ginis, 2000: Real-case simulations of hurricane–ocean interaction using a high-resolution coupled model: Effects on hurricane intensity. *Mon. Wea. Rev.*, 128, 917–946.
- Bender M.A., Ginis, I. & Kurihara, Y. Numerical simulations of the tropical cyclone-ocean interaction with a high-resolution coupled model. *J. Geophys. Res.*, 98, pp. 23,245-23,263, 1993.
- Bender, M.A., I. Ginis, R. Tuleya, B. Thomas, T. Marchok, 2007: The operational GFDL coupled hurricane-ocean prediction system and a summary of its performance. *Mon. Wea. Rev.* In press.
- Emanuel, K. A., 1986: An air–sea interaction theory for tropical cyclones. Part I: Steady-state maintenance. *J. Atmos. Sci.*, 3, 585–605.
- Emanuel, K. A., 1988: The maximum intensity of hurricanes. *J. Atmos. Sci.*, 45, 1143–1155.
- Emanuel, K. A., 1999: Thermodynamic control of hurricane intensity. *Nature*, 401, 665–669.
- Ginis, I., 2002: Hurricane-ocean interactions, 2002: Tropical cyclone-ocean interactions. Chapter 3. In *Atmosphere-Ocean Interactions*, Edited by W. Perrie, WIT Press, Advances in Fluid Mechanics Series, Vol. 33, 83 – 114.
- Khain, A., and I. Ginis, 1991: The mutual response of a moving tropical cyclone and the ocean. *Beitr. Phys. Atmos.*, 64, 125–141.
- Ooyama, K. Numerical simulation of the life-cycle of tropical cyclones, 1969. *J. Atmos. Sci.*, 26, 3-40.
- Price, J. F., 1981: Upper ocean response to a hurricane. *J. Phys. Oceanogr.*, 11, 153–175.
- Schade, L. R., and K. A. Emanuel, 1999: The ocean’s effect on the intensity of tropical cyclones: Results from a simple coupled atmosphere–ocean model. *J. Atmos. Sci.*, 56, 642–651.
- Shen, W., R. E. Tuleya, and I. Ginis, 2000: A Sensitivity study of the thermodynamic environment on GFDL hurricane intensity: Implications for global warming, *J. of Climate*, 13, 109-121.